POLITECNICO
MILANO 1863

SCUOLA DI INGEGNERIA INDUSTRIALE
E DELL'INFORMAZIONE

# A Loosely-Coupled Scheme for Cardiac Electro Fluid Structure Interaction

Tesi di Laurea Magistrale in
Mathematical Engineering - Ingegneria Matematica

Author: **Martin Geraint Gabriel**

Student ID: 946716
Advisor: Prof. Christian Vergara
Co-advisors: Eng. Michele Bucelli
Academic Year: 2020-21

# Abstract

The purpose of this work is to propose a new Loosely-Coupled Scheme for Cardiac Electro Fluid Structure Interaction Problems. Hence, we review some of the most critical issues in modeling the cardiac functions, presenting the mathematical models to describe all the physics involved. Explicit schemes, due to their instability issue in in hemodynamics, are difficult to implement in this context. However, if stable, they allow to use different already existing solvers to solve each problem separately, leading to a great improvement in terms of computational costs. The design of our proposed new scheme relies on an explicit partitioned Robin-Neumann treatment of the Fluid Structure Interaction Problem, which requires the choice of a Robin interface parameter. Among the different options, we make use of a theoretical analysis on a simplified problem to obtain guess values for such parameter. We explore different choices of parameters, running 3D simulations of a geometrically simplified human ventricle, trying to reproduce a physiological behavior, according to specific requirements. Hence, we define a range of values for the Robin interface parameter to obtain stable, accurate and computationally efficient simulations with the new proposed explicit scheme. Finally, we compare the performances of our new scheme with other algorithms based on an implicit treatment of the Fluid Structure Interaction Problem, obtaining encouraging results in terms of accuracy, stability and mostly in terms of computational cost.

**Keywords:** Explicit Scheme, Hemodynamics, Fluid Structure Interaction, Cardiac Mathematical Model, Computational Fluid Dynamics

# Abstract in lingua italiana

Lo scopo di questo lavoro è quello di proporre un nuovo schema esplicito per il problema di interazione elettro-fluido-strutturale in ambito cardiaco. Per fare ciò passiamo in rassegna alcuni dei punti critici nella modellizzazione delle funzioni cardiache, presentando i modelli matematici usati per descrivere le diverse fisiche coinvolte. Gli schemi espliciti, data la loro instabilità in ambito emodinamico, sono difficili da implementare in questo contesto. Tali schemi però, quando stabili, ci permettono di usare solver già esistenti per simulare separatamente i diversi problemi matematici, permettendoci di ottenere grandi vantaggi nei costi computazionali. Il nuovo schema esplicito che proponiamo si basa sulla risoluzione partizionata del problema di interazione fluido-strutturale con lo splitting di Robin-Neumann, il quale richiede la scelta di un parametero di interfaccia. Tra i diversi modi per ottenere alcuni guess iniziali per tale parametro, noi ci basiamo su una analisi teorica di un problema semplificato. Nel corso del lavoro proposto, effettuiamo diverse simulazioni 3D usando il nuovo schema esplicito con diversi valori del parametro di interfaccia, utilizzando un modello geometricamente semplificato del ventricolo sinistro, con lo scopo di riprodurre un comportamento fisiologico delineato da precisi requisiti. Da questa analisi definiamo un intervallo di valori per il parametro di interfaccia, che dia simulazioni stabili, accurate e computazionalmente efficienti. Infine, compariamo i risultati ottenuti con il nuovo schema con quelli ottenuti con altri schemi basati su un trattamento implicito della interazione fluido-strutturale, ottenendo risultati incoraggianti dal punto di vista di accuratezza, stabilità e soprattutto costo computazionale.

**Parole chiave:** Schema Esplicito, Interazione Fluido Struttura, Emodinamica, Modello Matematico Cardiaco, Fluidodinamica Computazionale

# Contents

# 1 | Introduction

## 1.1. On the importance of Fluid Structure Interaction problems

Fluid Structure Interaction (FSI) problems are widely present in many fields, one of the most common is surely aeroelasticity [35, 39, 64, 75, 76, 79], but there are other important fields ranging from industrial [20, 91, 104] to living systems applications [8, 18, 33, 83]. We can have examples of fluid structure interaction every day, looking at a bridge or a building advected by the wind (see figure 1.1b) or considering the blood flowing through our veins. There are many reasons to model and computationally simulate these kinds of situations, for instance to find the best shape for an airfoil to oppose minimal resistance to air (see figure 1.1a), or to give a priori hints to a surgeon on the best way to operate a plaque in an artery [33] (see figure 1.2). The design of efficient and accurate algorithms for the numerical simulation of FSI problems plays a fundamental role in the pursuit of optimal solutions in all the fields cited above: faster and less consuming airplanes, more stable bridges, more efficient assembly line or safer surgical operations. These kinds of problems are really difficult to solve numerically since we have to deal with two different physics and we have to provide suitable conditions to allow them to interact. Indeed we need to provide a kinematic condition to ensure that the fluid and the structure move at the same velocity at the interface; we also need a dynamic condition to ensure the validity of the Third Newton's law at the interface. Moreover the fact that the two domains (i.e. both structure and fluid domain) are moving also requires to satisfy a geometric coupling and creates the additional issue to select the correct formulation to be used to state the fluid and the structure equations. Often the structure is treated in a reference configuration, whilst the fluid is treated making use of the Arbitrary Lagrangian Eulerian (ALE) Formulation [15, 94].

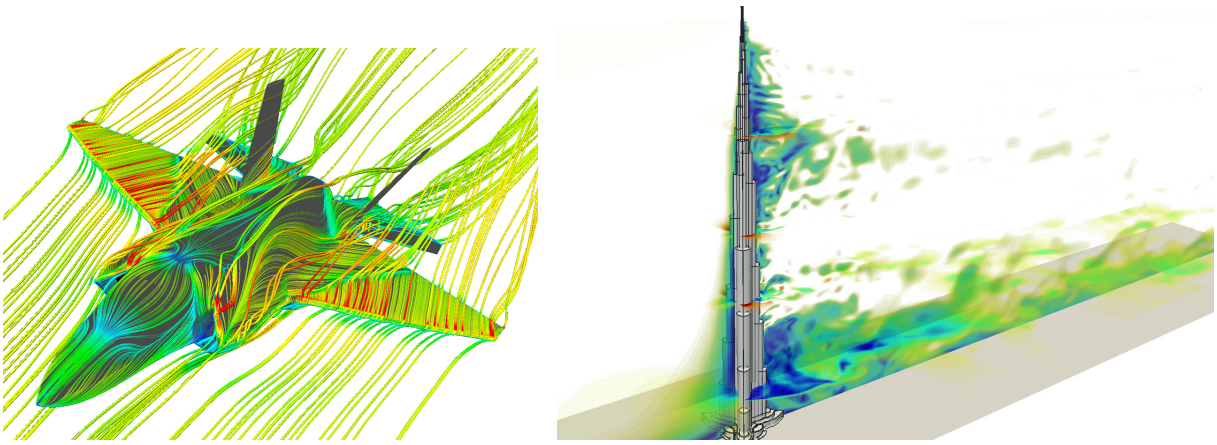

(a) Wind streamlines advecting an airplane. (b) Wind advecting a vertical building.

Figure 1.1: Examples of Fluid Structure Interaction simulations (ansys.com).

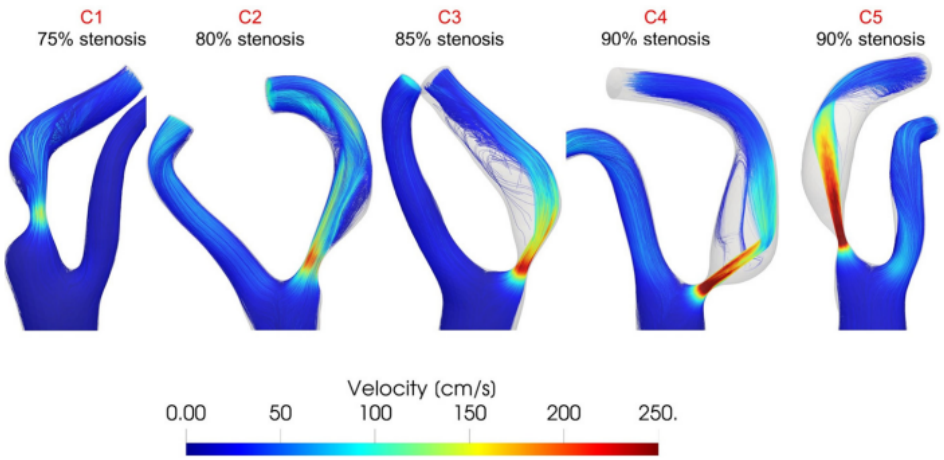


Figure 1.2: Streamlines of the velocity fields at systolic peak with different levels of stenosis in presence of calcific plaques [18].

Besides the large number of degrees of freedom characterizing an FSI problem, another big issue is the treatment of the conditions that ensure the correct fluid structure interaction and the correct movement of the two meshes. Indeed, from a numerical point of view it is not easy to ensure the dynamic and kinematic conditions due to the numerical errors coming from approximation schemes and the fact that the fluid and structure subproblems are often solved separately. Therefore, one can understand that the numerical simulation of an FSI problem is tough and leads to huge computational costs; the reduction of such costs becomes crucial in the design of cutting edge algorithms. The type of schemes that one can use have their range of validity depending on the densities at stake: indeed, some

of them can be suitable for a specific FSI problem but not for others. In general, there are different ways to address the FSI numerical problem [21]. The most common are:

- Monolithic [13, 31, 43, 57];
- implicit (or fully-coupled) partitioned scheme [58, 79];
- explicit (or loosely-coupled) partitioned scheme [22–24, 35, 37, 50, 51, 54].

In the Monolithic ones, the entire FSI problem is solved all together relying on a large linear system, so all the conditions that ensure the correct fluid structure interaction are present in the system with their contributions. Usually, when Monolithic schemes are used, a preconditioner is needed due to the elevated condition number of the linear system arising from the discretization. On the other hand, with partitioned schemes, the FSI problem is separated into the smaller fluid and structure subproblems; the kinematic and dynamic conditions are usually split, one for the structure problem and one for the fluid problem, becoming boundary conditions on the fluid-structure interaction interface and giving the name to the scheme (e.g. Dirichlet-Neumann). In general, Monolithic schemes are faster than implicit partitioned ones, even if they are not modular, i.e. they can not in general be designed as the subsequent solution of pre-existing codes, as can be done for partitioned schemes. When one considers explicit partitioned schemes (i.e. only one iteration on fluid and one on structure at each time step) stability issues may arise but improvements in efficiency could be obtained in the stable cases.

## 1.2. Fluid Structure Interaction in hemodynamics

One of the fields where numerical methods for FSI are thriving surely is hemodynamics, since there are many situations where a fluid and a structure have to interact: for instance blood in arteries [33, 65, 80], cardiac perfusion [14, 32], blood-myocardium [21, 30], blood-eye [6]. The main difference between hemodynamics and many other fields is the fact that the computational domain is not chosen or designed to achieve particular results, but is given and patient-specific. This creates an additional problem, i.e. the need to acquire data and recreate the computational mesh for every different patient [3, 28, 82, 105]. Therefore, there is an increasing cooperation between doctors and mathematicians in sharing information and large amounts of data to be able to simulate many different patients. Of course having many different simulations gives the opportunity to obtain some kind of average situation [1], useful to test new algorithms and scenarios.

One of the great advantages of having a computational model for many physiological human functions is to have the possibility to predict how the human body will respond

to possible changes and interventions. Indeed, one can modify the domain or change something in the model to simulate what could happen if that change was applied on the patient, all this without his or her direct involvement. For this reason, in recent years many studies have been carried out in the most various fields to have a picture as large as possible [83, 85], but also to solve delicate medical problems [18, 33]. One can easily understand that in a context where human life is at stake, computational performances become crucial to distinguish between bad and excellent algorithms to simulate such problems. Therefore many strategies have been implemented, from monolithic schemes [13, 31, 43, 57] to implicit partitioned ones [10, 11, 27, 69–71]. Recently explicit partitioned schemes have been investigated as well, due to their low computational cost and the possibility to couple together already existing solvers. However, loosely-coupled schemes are often unstable and need a small time discretization step $\Delta t$. Moreover in this context there is another big issue called added mass effect, that occurs when the considered densities are comparable: this is the case of blood and arteries to mention one. Indeed one of the first schemes that we can think of, the Dirichlet-Neumann scheme, is unconditionally unstable in this context [27, 40, 69, 83]. Some works have been carried out on the stabilization of unstable explicit schemes for hemodynamics, see for example [22–24, 38].

## 1.3. Loosely-coupled schemes in hemodynamics

Due to the instability of the explicit Dirichlet-Neumann scheme other kinds of explicit schemes have been taken into account. For instance in [38] it has been proven that it is sufficient an implicit coupling between the fluid pressure and the vessel wall displacement to achieve stability without stabilization terms for the Dirichlet-Neumann scheme. Therefore, a semi-implicit scheme can be designed, where the advection-diffusion problem (i.e. a fluid problem without pressure) is solved with a Dirichlet condition on the interface; then a pressure problem strongly coupled with the structure problem, both equipped with a Neumann condition on the interface, are solved in a loop at fixed time [83]. On the other hand, concerning explicit schemes, many studies have been carried out on Robin-Robin schemes [7, 10–12, 44, 49, 50, 52, 68, 83]. These schemes are designed considering a Robin condition, i.e. a linear combination of a Dirichlet and a Neumann condition, to ensure the kinematic and the dynamic conditions. More in detail, with these schemes the FSI problem is split in a fluid problem and a structure problem both equipped with a Robin condition on the interface, so that these two problems are solved one after another, only once per time step. Since we have a linear combination we have to choose two Robin parameters, one for the fluid and one for the structure. There are many ways to deal with the task of designing an explicit Robin-Robin scheme, for instance in [23] a Discontinuous

Galerkin(DG)-like mortaring of the interface coupling conditions is proposed. This idea can be reinterpreted as an explicit Dirichlet-Robin scheme because one of the two interface Robin parameters turns out to be $\infty$; for what regards the other, it is linked to the penalty parameter of the DG method. Unfortunately this setting is not able to control the pressure fluctuations on the fluid-structure interface, therefore a penalizing stabilization term has to be added to the fluid problem, leading to an absolutely stable scheme under some CFL-like condition. Another stable explicit Robin-Robin scheme has been introduced in [12], where the interface Robin parameters were chosen after analyzing the incoming and outcoming characteristic variables of the vessel wall problem. In that work, the authors also present formulas to compute the coupling parameters in the context of linear elasticity, leading to a tight coupling between the fluid and the structure problems. However for what regards this thesis we will rely on some studies based on the theoretical analysis of simplified problems to choose the optimal parameters in different geometries [49–52]. In these works, firstly the implicit partitioned scheme on a simplified theoretical problem is taken into account to select the optimal parameters, then those parameters are used for the explicit partitioned counterpart, hoping to achieve a good level of stability and accuracy, even though there is no guarantee of the optimality for the loosely coupled scheme.

Among Robin-Robin schemes there is a particular one that requires the use of only one Robin parameter instead of two: the Robin-Neumann scheme [37, 50, 51, 54]. This scheme is obtained setting to 0 one of the two parameters of the linear combination, leading to a Robin condition for the fluid problem and a Neumann condition for the structure problem. Summing up, the Robin interface based explicit methods are among the most used in hemodynamics, they allow us to solve only one fluid problem and one structure problem at each time step, preserving a considerable stability with respect to Dirichlet-Neumann scheme. Moreover in [37, 50, 51] encouraging results have been achieved using such loosely-coupled partitioned schemes also in realistic applications, e.g. human Aortic Abdominal Aneurysm (AAA) [50]. Indeed, both accuracy and stability were reached, together with a substantial reduction of the computational cost. These results of accuracy and stability were not trivial, given the large added mass effect present in these settings.

## 1.4. The Electro Fluid Structure Interaction Problem

A further step consists in investigating a more complex problem: the fluid-structure interaction problem arising in the cardiac ventricles [84]. In this context, a new phenomenon

comes into play, i.e. electrophysiology [26, 60], so that the resulting mathematical model yields an Electro Fluid Structure Interaction (EFSI) problem. In this case the structure problem is not only passive and subjected to the fluid action, as in arteries, but it is driven by the active contraction of the myocardial tissue, determined in turn by the excitation of muscular cells, triggered by the stimulus of the the sinoatrial node. This complication leads to an additional problem to model and solve, and adds an active component to the stress tensor [62] of the structure problem. Moreover the modeling of the human ventricle is way more challenging with respect of other FSI problems also for many other reasons:

- the computational domain: indeed, this organ is very complex and presents crucial difficulties in the representation of many features, from the Purkinje fibers [61, 63, 78] to the mitral and aortic valves [36, 42]. Often these kinds of issues are solved by means of algorithms to generate the fibers [16, 92], or introducing some simplifications of the domain or of the models used [30];
- numerically the electrophysiological problem increases the computatonial cost; indeed, to solve such problem, really fine time and space discretizations are needed to well capture the phenomena [55, 56, 66]. Often we need to use two different meshes for the electrical and the structural problem or even two different time steps [90];
- we have to deal with an additional coupling with electrophysiology;
- the modeling of the myocardial mechanics itself is not an easy task; indeed, it is a non linear anisotropic material that needs the design of specific models to be accurate [53];
- the modeling of the blood flow has its issues; indeed, a pre-turbulent regime is present with some inclinations to backflow, therefore suitable stabilization models have to be considered [17, 19, 41, 67, 102];
- boundary conditions represent another important issue; indeed, accurate models have to be chosen to model crucial aspects, from the blood circulation [45, 97] to the pericardial sac embedding the myocardium [46, 73, 77, 96];
- the huge computational cost deriving from all the remarked issues typically results in extremely long computational times and often forces to use simplified geometries and models [90] to obtain results in acceptable times;
- the human heartbeat is characterized by 4 different phases:

    1. isovolumic contraction: both valves are closed and the myocardium starts actively contracting due to the excitation of muscular cells. Since the valves

are closed, an increase of pressure takes place in the ventricle and when the ventricular pressure overcomes the aortic one, the aortic valve opens;

2. ejection phase: after the opening of the aortic valve the blood is ejected into the circulation. The bloodflow continues streaming through the aortic valve until backflow takes place, at that point the aortic valve is closed leading again to an isovolumic phase;

3. isovolumic relaxation: the ventricle gradually relaxes in an isovolumic manner, resulting in a decrease of pressure until the allowed minimum pressure. This is when the mitral valve opens;

4. ventricular filling: the opening of the mitral valve allows the blood to enter again in the ventricle, filling it until the blood flows towards the mitral valve. At that point the valve is closed and a new heartbeat starts.

Therefore, it is easy to understand the difficulty of catching and reproducing all these phases during a numerical simulation.

There are many ways to design an algorithm to solve such complex problem and one of the crucial issues is how to couple together all the physics. Here are some examples of different strategies carried on in previous works:

- fully implicit scheme, where everything is coupled together and condensed in a big linear system and solved simultaneously [45, 93];
- use an analytical law for the electrical problem (or solve electrophysiology stand alone), focusing on the treatment of the 3-D FSI problem either with Monolithic and partitioned schemes (i.e. both implicit Dirichlet-Neumann and implicit Robin-Neumann were considered)[21]. The conclusion of such work was that the Monolithic scheme was faster and more accurate than implicit partitioned ones;
- simplified models for the fluid problem, focusing on the modeling of the coupled electromechanic problem [5, 46, 59, 100].

## 1.5. Thesis purpose

The aim of this thesis is to present and implement a new loosely-coupled scheme for Electro Fluid Structure Interaction, based on the solution of one electrophysiology, one fluid and one structure problem at each time step. From now on we will call it *Loosely Coupled EFSI Scheme*. The second significant novelty is the first application to a cardiac setting of the theory developed in [49–52] for the estimation of suitable Robin interface

parameters. Indeed the idea is to treat the FSI part with an explicit Robin-Neumann scheme using as the Robin parameter the optimal one coming from the implicit Robin-Neumann scheme and selecting it through the theoretical analyses carried on in the above mentioned papers. In the end, to evaluate and analyse the proposed scheme, a comparison with another scheme will be carried on, i.e. a scheme where electrophysiology is still solved stand alone (with a mechanical feedback coming from previous time steps) but FSI is solved in a Monolithic fashion (see figure 1.3), we will call this scheme *Staggered E-Monolithic FSI Scheme*.

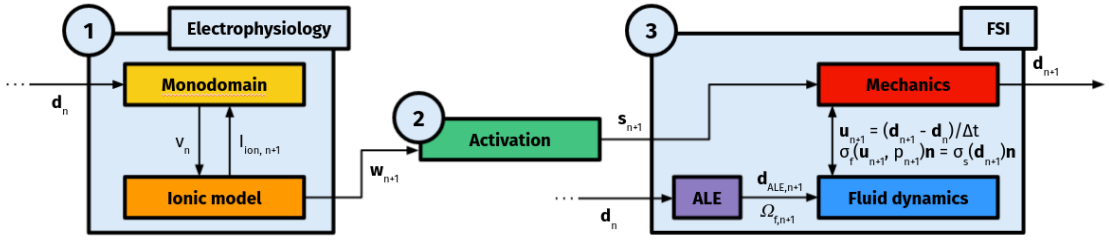


Figure 1.3: Scheme where FSI is solved in a Monolithic fashion but decoupled from electrophysiology (Eng. Michele Bucelli).

To model the human ventricle a geometrical simplified model is used, but both fluid and structure are modelled in 3 dimensions.

The aim of our work is to obtain both accuracy and stability using the new loosely-coupled proposed scheme. Moreover we aim also to obtain a reduction of the computational costs, comparing its performances with the *Staggered E-Monolithic FSI Scheme*'s ones. The work will be organized as follows:

- In Chapter 2 all the mathematical models are presented and described in their continuous forms;
- In Chapter 3 all the numerical schemes are described and presented;
- In Chapter 4 the modus operandi of the parameters choice will be discussed;
- In Chapter 5 all the results are presented and discussed;
- In Chapter 6 conclusions are drawn and hints for possible developments are proposed.

# 2 | Electro Fluid Structure Interaction Mathematical Model

## 2.1. Computational domain

We model the human ventricle as schematized in figure 2.1, it is composed by a fluid domain covered by the structure domain, except for the base (divided in $\Gamma_{s,b}$ for the structure base and $\Gamma_{f,b}$ for the fluid base), where two idealized overlapping valve orifices are present: the aortic one ($\Gamma_{AV}$) and the mitral one ($\Gamma_{MV}$). Let $\hat{\Omega}_s \subset \mathbb{R}^3$ be an open bounded domain representing the structure domain, i.e. the myocardium (the muscular tissue of the ventricle), in an undeformed and stress-free reference configuration. Differently from other FSI problems, the myocardium is not only passive, like arteries, but has an active component due to the contraction of its cells (driven by electrophysiology). Then let $\hat{\Omega}_f \subset \mathbb{R}^3$ be the fluid domain, corresponding to the space occupied by blood, again in the reference configuration. We denote the common interface by $\hat{\Sigma} = \partial\hat{\Omega}_s \cap \partial\hat{\Omega}_f$ representing the endocardial surface of the ventricle. We then define the two unit vectors normal to the boundaries: $\hat{\boldsymbol{n}}_s$ and $\hat{\boldsymbol{n}}_f$ such that $\hat{\boldsymbol{n}} = \hat{\boldsymbol{n}}_f = -\hat{\boldsymbol{n}}_s$ on $\hat{\Sigma}$. Finally, we define the epicardial surface $\Gamma_{s,epi}$, corresponding to the external portion of the structure domain.

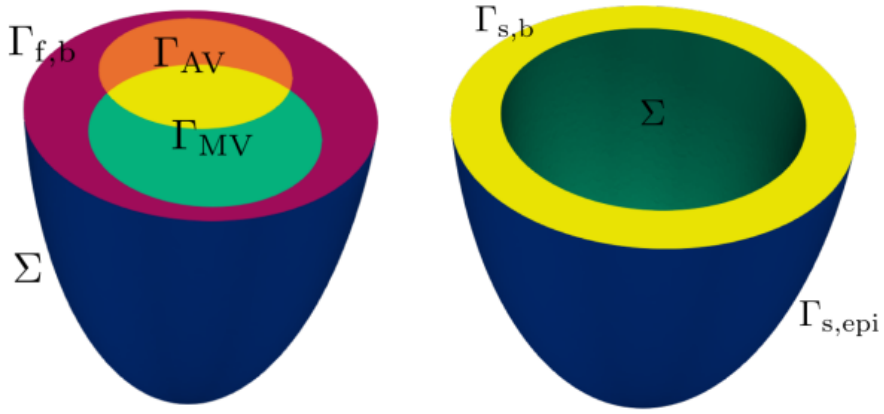


Figure 2.1: The computational domain [21].

## 2.2. Fibers generation

The muscular tissue is characterized by the presence of fibers [61]. The fibers' disposition indicates the preferential direction of conduction for the electrical activation [78]; moreover it has a role also in the active and passive mechanics [9, 47, 53, 89, 90]. Due to these reasons we need to model this anisotropy. Even if there are ex-vivo measurement techniques to acquire data on the organization of fibers, e.g. Diffuson Tensor Imaging (DTI) [78], they are not available in the standard clinical practice and require specific acquisitions. Therefore, fibers are tipically modeled and generated through algorithms, known as rule-based methods [16, 34, 78, 92], combined with experimental evidences. Among the different choices, we will choose the Rossi-Lasilla model [92]: we can see an example of fibers' direction computed with such algorithm in figure 2.2.

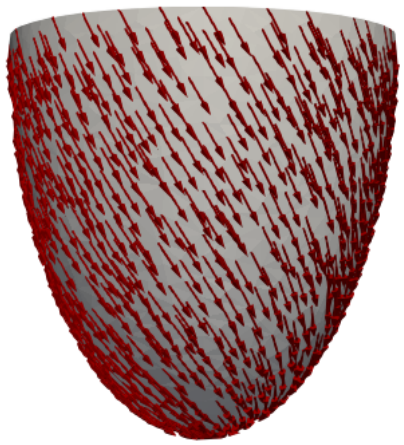

Figure 2.2: Direction of the fibers computed through the Rossi-Lassila Algorithm.

## 2.3. Electrophysiology

We model electrophysiology with the monodomain model [26, 29, 55, 60, 89, 90]. Let us denote by $v$ the transmembrane potential, that is the difference of potential between the intracellular space of cardiomyocytes and the extracellular matrix. Then the monodomain equation in a moving domain reads:

$$\begin{cases} J\chi C_m \dfrac{\partial v}{\partial t} - \nabla \cdot (JF^{-1}\Sigma_m F^{-T}\nabla v) + J\chi I_{ion}(v, \boldsymbol{w}) = J\chi I_{app} & \text{in} \quad \hat{\Omega}_s \times (0,T), \\ F^{-1}\Sigma_m F^{-T}\nabla v \cdot \hat{\boldsymbol{n}}_{\boldsymbol{s}} = 0 & \text{on} \quad \partial\hat{\Omega}_s \times (0,T), \\ v = v_0 & \text{in} \quad \partial\hat{\Omega}_s \times \{0\}, \end{cases} \tag{2.1}$$

where $F = I + \nabla \boldsymbol{d}$ , $J = \det F$ and $\boldsymbol{d}$ is the displacement field that represents the deformation of the structure (i.e. myocardium), see Section 2.4. Then $\Sigma_m$ is defined as $\Sigma_m = \Sigma_m^l \boldsymbol{f} \otimes \boldsymbol{f} + \Sigma_m^t \boldsymbol{s} \otimes \boldsymbol{s} + \Sigma_m^n \boldsymbol{n}_{fib} \otimes \boldsymbol{n}_{fib}$, where $\Sigma_m^l$, $\Sigma_m^t$, $\Sigma_m^n$ are the conductivities in the longitudinal, transversal and normal direction respectively, and $\boldsymbol{f}$,$\boldsymbol{s}$ and $\boldsymbol{n}_{fib}$ represent the fiber direction, the direction of the sheets of fibers and the normal direction respectively; these three directions are generated with rule-based algorithm as mentioned in Section 2.2. We have used a Neumann homogeneous boundary condition on $\partial\hat{\Omega}_s$ to ensure that the ventricle is electrically isolated. $\chi$ is the surface to volume ratio and $C_m$ is the membrane capacitance. $I_{app}$ is the current that models the stimulus of activation in terms of a right-hand-side forcing term, while $I_{ion}$ is the ionic current, that depends both on $v$ and on ionic variables $\boldsymbol{w} : \hat{\Omega}_s \times (0,T) \to \mathbb{R}^n$. Some of the ionic variables $\boldsymbol{w}$ represent the concentrations of ions and the others represent the gating variables, i.e. fractions of open ionic channels through the cellular membrane [29]. The most relevant ionic concentration in the context of an electro-structure coupling is the calcium one, for more details see [90]. These variables are represented through an ionic model of the form:

$$\begin{cases} \dfrac{\partial \boldsymbol{w}}{\partial t} = \boldsymbol{F}_{ion}(v, \boldsymbol{w}) & \text{in} \quad \hat{\Omega}_s \times (0,T), \\ \boldsymbol{w} = \boldsymbol{w_0} & \text{on} \quad \partial\hat{\Omega}_s \times \{0\}. \end{cases} \tag{2.2}$$

There are many ionic models, that differ in terms of complexity and number of modeled ionic concentrations and channels. We will make use of the Ten Tusscher and Panfilov (TTP06) model for ventricular cells [98, 99]. It features $n = 18$ ($\boldsymbol{w} : \hat{\Omega}_s \times (0,T) \to \mathbb{R}^{18}$) variables, of which 6 are ionic concentrations and 12 are gating variables. The last

electrical issue to discuss is the stimulation, that is modelled in a simple way: an external current is applied in three different points on the epicardium, as we can see in figure 2.3. This is a well accepted simplification that surrogates the action of the Purkinje network [60] that propagates the stimulus coming from the sinoatrial node [90]. A technique for patient specific generation of the network can be found in [101]

We can summarize the monodomain (2.1) and the ionic model equations (2.2) by means of an abstract notation to identify the underlying PDEs and ODEs highlighting the different dependencies; this will be useful in chapter 3:

$$\begin{cases} v = \mathcal{M}(v, \boldsymbol{w}, \boldsymbol{d}) & \text{in} \quad \hat{\Omega}_s \times (0, T), \\ \boldsymbol{w} = \mathcal{I}(v, \boldsymbol{w}) & \text{in} \quad \hat{\Omega}_s \times (0, T), \end{cases} \tag{2.3}$$

wherein the dependency of the solutions on the other variables is in general non -linear.

(a) View from above. (b) Lateral view.

Figure 2.3: Initial propagation of the electrical signal after the stimulus is applied. Activation starts at three stimulation points and propagates in all directions following fibers.

## 2.4. Structure mechanics

The structure is modelled in the Lagrangian framework denoting by $\boldsymbol{d}(\hat{\boldsymbol{x}}, t)$ the displacement at point $\hat{\boldsymbol{x}}$ and time $t$ in the reference configuration. We define the Lagrangian map from the reference to the current configuration as:

$$\mathcal{L}_s : \hat{\Omega}_s \to \Omega_s,$$

$$\boldsymbol{x} = \mathcal{L}_s(\hat{\boldsymbol{x}}) = \hat{\boldsymbol{x}} + \boldsymbol{d}(\hat{\boldsymbol{x}}, t), \;\; s.t. \;\; \boldsymbol{x} \in \Omega_s, \hat{\boldsymbol{x}} \in \hat{\Omega}_s.$$

The myocardium is modelled as a hyperelestic material in the Lagrangian framework [74, 89]. Defining $\rho_s$ as the structure density, we can write the partial differential equation in the reference configuration (for the sake of simplicity we remove the hat from the variables, but it remains visible on the domains):

$$\begin{cases} \rho_s \dfrac{\partial^2 \boldsymbol{d}}{\partial t^2} - \nabla \cdot P_s(\boldsymbol{d}) = 0 & \text{in } \hat{\Omega}_s \times (0,T), \quad (2.4a) \\ \boldsymbol{d} = \boldsymbol{0} & \text{on } \hat{\Gamma}_{s,b} \times (0,T), \quad (2.4b) \\ \dfrac{\partial \boldsymbol{d}}{\partial t} = \boldsymbol{u} & \text{on } \hat{\Sigma} \times (0,T), \quad (2.4c) \\ \sigma_s(\boldsymbol{d})\boldsymbol{n} = \sigma_f(\boldsymbol{u}, p)\boldsymbol{n} & \text{on } \Sigma \times (0,T), \quad (2.4d) \\ \boldsymbol{d} = \boldsymbol{d_0} & \text{in } \hat{\Omega}_s \times \{0\}, \quad (2.4e) \\ \dfrac{\partial \boldsymbol{d}}{\partial t} = 0 & \text{in } \hat{\Omega}_s \times \{0\}, \quad (2.4f) \\ + \textit{ Pericardium boundary condition} & \text{on } \hat{\Gamma}_{s,epi} \times (0,T). \quad (2.4g) \end{cases}$$

For what concerns the pericardium boundary condition we use a visco-elastic condition on $\hat{\Gamma}_{s,epi}$ to surrogate the action of the pericardium [46, 73, 77, 90, 96]:

$$P_s(\boldsymbol{d})\hat{\boldsymbol{n}}_s = -(\hat{\boldsymbol{n}}_s \otimes \hat{\boldsymbol{n}}_s)\left(K_\perp \boldsymbol{d} + C_\perp \frac{\partial \boldsymbol{d}}{\partial t}\right) - (I - \hat{\boldsymbol{n}}_s \otimes \hat{\boldsymbol{n}}_s)\left(K_\parallel \boldsymbol{d} + C_\parallel \frac{\partial \boldsymbol{d}}{\partial t}\right), \quad (2.5)$$

where $K_\perp$ and $K_\parallel$ are stiffness coefficients, while $C_\perp$ and $C_\parallel$ are viscosity coefficients.

*Remark* 1. Notice that the visco-elastic condition on $\hat{\Gamma}_{s,epi}$ is only on the external part of the structure, while on the internal part of the structure $\Sigma$ (i.e. the Fluid-Structure interface) we need to provide coupling conditions (2.4c) (2.4d), where $\boldsymbol{u}$ and $p$ are the fluid velocity and the fluid pressure respectively. The first coupling condition (2.4c) is written in reference configuration and ensures the continuity of velocity at the interface and it is called *kinematic condition*. On the other hand the second one (2.4d) is called *dynamic condition* and it ensures the continuity of forces at the interface, corresponding to the Newton's Third Law. For the sake of simplicity the second one is written in current configuration, where $\sigma_f$ (see Section 2.5) and $\sigma_s = J^{-1} \cdot P_s(\boldsymbol{d})F^T$ represent the Cauchy Stress tensors for fluid and structure respectively. These interface conditions will hold true for the Fluid problem as well.

$P_s(\boldsymbol{d})$ is the first Piola-Kirchhoff stress tensor, function of the displacement $\boldsymbol{d}$ through the constitutive equation of the material [53]. It is exactly here that electrophysiology comes

into play. Indeed we have not only a passive part $P_{pas}$ of the stress tensor but also an active one $P_{act}$, leading to the following decomposition: $P_s = P_{pas} + P_{act}$ [4, 72, 88, 93]. Like other structure problems in the hyperelastic framework, the passive part is defined as the derivative of a suitable strain energy function $\Theta(F)$, that depends on the deformation gradient $F$ and models the passive properties of the material:

$$P_{pas} = \frac{\partial \Theta}{\partial F}. \tag{2.6}$$

We will choose the Guccione model [53] for the passive part, leading to a non linear and anisotropic behavior of the passive mechanics, exploiting the presence of fibers. On the other hand for the active part we have:

$$P_{act} = T_{act}(\boldsymbol{d}, [\mathrm{Ca}^{2+}]) \frac{F\boldsymbol{f} \otimes \boldsymbol{f}}{\sqrt{I_{4f}}}, \tag{2.7}$$

where $I_{4f} = F\boldsymbol{f} \cdot F\boldsymbol{f}$ is a measure of the tissue stretch in the fiber direction and $F = I + \nabla \boldsymbol{d}$. $T_{act}$ is an active tension in the fibers direction $\boldsymbol{f}$ [4, 88, 93], computed as a function of displacement and calcium concentration [86], that is one of the component of $\boldsymbol{w}$ from the ionic model equations. To compute $T_{act}$ the activation model $RDQ18$ is used. Due to its high computationally cost, it is surrogated by means of an Artificial Neural Network (ANN) [87, 88]. To highlight the dependencies on one or another problem, in what follows we will refer to equation (2.7) as:

$$P_{act} = \mathcal{T}_{act}(\boldsymbol{d}, \boldsymbol{w}), \tag{2.8}$$

where the dependence on $\boldsymbol{w}$ is intended as that on the calcium concentration.

Regarding boundary conditions we use a homogeneous Dirichlet one for the whole base (both $\Gamma_{s,b}$ and $\Gamma_{f,b}$) [72, 103] except for the valves that are discussed afterwards in Section 2.5.3. This is not physiological but it helps avoiding problems related to moving fluid inflow and outflow. Finally, as mentioned before, we prescribe a visco-elastic Robin condition on the external surface, mimicking the presence of the pericardial sac [46, 73, 77, 90, 96].

We summarize the structure problem (2.4a) (2.4b) (2.4e) (2.4f) (2.4g) by means of the

abstract notation to highlight dependencies:

$$\boldsymbol{d} = \mathcal{S}(\boldsymbol{d}, \boldsymbol{w}) \quad in \quad \hat{\Omega}_s \times (0, T). \tag{2.9}$$

We remark that the solution $\boldsymbol{d}$ of the structure problem depends nonlinearly on the displacement $\boldsymbol{d}$ due to the Guccione constitutive law, and depends also on the calcium concentration.

For what concerns the initial conditions for the structure displacement: the heart is never in a stress-free condition, due to the pressure exerted by blood. Therefore, obtaining a reference configuration to formulate the structure problem (2.4) from medical imaging data is not trivial. To this end, we do a pre-processing step to find the reference configuration before starting the real simulation; this is done using inverse problem algorithms presented in [90], that take as an input the available mesh (e.g. generated from patient specific MRI) and a value of the pressure $p_{ref}$ at which the mesh is loaded and output the reference configuration $\hat{\Omega}_s$. For the same reasons, initial conditions are not stress-free, but rather see the structure loaded with some initial pressure $p_0$. We find such initial configuration by solving a quasi-static equation to find $\boldsymbol{d}_0$. All these things are done only on the structure, while the fluid domain is surrogated with a spatially homogeneous pressure value.

## 2.5. Fluid dynamics

Another difficulty in modeling the human ventricle is that the fluid domain is moving during the heartbeat. To take this into account, we rely on a particular formulation for fluid dynamics: the Arbitrary Lagrangian Eulerian (ALE) formulation [94]. This kind of formulation is based on the idea of looking at the problem neither from the point of view of the fluid movement nor from an external observer, but from the point of view of the moving fluid domain. To this end, we have to define a fluid domain displacement $\boldsymbol{d}_{ALE}$ and its velocity: $\boldsymbol{u}_{ALE} = \dfrac{\partial \boldsymbol{d}_{ALE}}{\partial t}$. The ALE formulation modifies the Navier-Stokes equations and introduces a new problem to solve, i.e. the geometric problem.

### 2.5.1. Geometric problem

The idea is to extend the structure displacement $\boldsymbol{d}$, computed on the interface $\hat{\Sigma}$, to the fluid domain, to obtain a value of $\boldsymbol{d}_{ALE}$ in every point of $\hat{\Omega}_f$. The condition that we are going to impose is:

$$\boldsymbol{d}_{ALE} = \boldsymbol{d} \quad \text{on} \quad ,\hat{\Sigma} \tag{2.10}$$

and it is called *geometric condition*. The extension can be done in different ways [94]. Here we consider a harmonic extension (also here for the sake of simplicity we remove the hat from the variables, but it remains visible on the domains):

$$\begin{cases} -\Delta \boldsymbol{d}_{ALE} = \boldsymbol{0} & \text{in} \quad \hat{\Omega}_f, \\ \boldsymbol{d}_{ALE} = \boldsymbol{d} & \text{on} \quad \hat{\Sigma}, \\ \boldsymbol{d}_{ALE} = \boldsymbol{0} & \text{on} \quad \hat{\Gamma}^D_{ALE} \subset \partial\hat{\Omega}_f, \\ \nabla(\boldsymbol{d}_{ALE})\boldsymbol{n}_f = \boldsymbol{0} & \text{on} \quad \hat{\Gamma}^N_{ALE} \subset \partial\hat{\Omega}_f. \end{cases} \tag{2.11}$$

Also in this context a map from the reference configuration to the current one is defined:

$$\mathcal{L}_f : \hat{\Omega}_f \to \Omega_f,$$
$$\boldsymbol{x} = \mathcal{L}_f(\hat{\boldsymbol{x}}) = \hat{\boldsymbol{x}} + \boldsymbol{d}_{ALE}(\hat{\boldsymbol{x}}, t), \;\; s.t. \;\; \boldsymbol{x} \in \Omega_f, \hat{\boldsymbol{x}} \in \hat{\Omega}_f.$$

### 2.5.2. Navier-Stokes equations

The blood is modelled as a Newtonian incompressible fluid through the Navier Stokes equations [81] in ALE formulation, as discussed before. The unknowns of this problem are the velocity of the fluid $\boldsymbol{u}$ and its pressure $p$. Denoting by $\rho_f$ the fluid density we can write:

$$\begin{cases} \rho_f \left[ \dfrac{\partial \boldsymbol{u}}{\partial t} + ((\boldsymbol{u} - \boldsymbol{u}_{ALE}) \cdot \nabla)\boldsymbol{u} \right] - \nabla \cdot \sigma_f(\boldsymbol{u}, p) = \boldsymbol{0} & \text{in} \quad \Omega_f \times (0,T), & \text{(2.12a)} \\ \nabla \cdot \boldsymbol{u} = 0 & \text{in} \quad \Omega_f \times (0,T), & \text{(2.12b)} \\ \boldsymbol{u} = \boldsymbol{0} & \text{on} \quad \Gamma_{s,b} \times (0,T), & \text{(2.12c)} \\ \boldsymbol{u} = \dfrac{\partial \boldsymbol{d}}{\partial t} & \text{on} \quad \Sigma \times (0,T), & \text{(2.12d)} \\ \sigma_f(\boldsymbol{u}, p)\boldsymbol{n} = \sigma_s(\boldsymbol{d})\boldsymbol{n} & \text{on} \quad \Sigma \times (0,T), & \text{(2.12e)} \\ \boldsymbol{u} = \boldsymbol{0} & \text{in} \quad \Omega_f \times \{0\}, & \text{(2.12f)} \\ + \textit{ Valves boundary conditions} & \text{on} \quad \Gamma_{AV} \times (0,T). & \text{(2.12g)} \end{cases}$$

The first equation (2.12a) expresses the balance of momentum, while the second one (2.12b) describes the incompressibility of the fluid. The stress tensor $\sigma_f$ is defined as

$\sigma_f(\boldsymbol{u}, p) = 2\mu D(\boldsymbol{u}) - pI$, where $\mu$ is the viscosity of the blood and $D$ is the symmetric gradient of velocity. On the other hand $\sigma_s$ is related to the first Piola-Kirchhoff tensor through $\sigma_s = J^{-1} P_s(\boldsymbol{d}) F^T$, where $F = I + \nabla \boldsymbol{d}$ and $J = \det F$. Notice how the ALE velocity $\boldsymbol{u}_{ALE}$ enters in equation (2.12a). Then here we have again the two interface conditions on $\Sigma$ (2.12d) (2.12e) that allow the fluid-structure coupling, both written in the current configuration. Finally a no-slip boundary condition (2.12c) is imposed on the fluid base $\Gamma_{s,b}$ as discussed in Section 2.4. Boundary conditions applied on valve orifices are described in detail in Section 2.5.3.

Finally the same abstract notation is used also for the fluid problem (2.12a) (2.12b) (2.12c) (2.12f) (2.12g):

$$(\boldsymbol{u}, p) = \mathcal{F}(\boldsymbol{u}, \boldsymbol{d}_{ALE}, \boldsymbol{d}; \Omega_f) \quad \text{in} \quad \Omega_f \times (0, T). \tag{2.13}$$

We can observe that the fluid problem is non linear due to the convective term, and depends also on $\boldsymbol{d}_{ALE}$ through $\boldsymbol{u}_{ALE}$ and on the displacement $\boldsymbol{d}$ through $\Omega_f$ due to the geometric problem.

### 2.5.3. Valves Boundary conditions

The two valves are simplified and represented by two overlapping orifices, denoted by $\Gamma_{AV}$ for the aortic one and $\Gamma_{MV}$ for the mitral one. We do not model them in a three dimensional way but with instantaneously switching boundary conditions, meaning that the opening and closing is an on-off mechanism:

- aortic valve:

  the switching boundary conditions are of the type Dirichlet-Resistance, meaning that when the valve is closed we have a Dirichlet no-slip condition (i.e. $\boldsymbol{u} = \boldsymbol{0}$), whilst when it is open we have a resistance boundary condition [45, 97] of the type:

$$\sigma_f(\boldsymbol{u}, p)\boldsymbol{n}_f = -\left(p_{AV} + R \int_{\Gamma_{AV}} \boldsymbol{u} \cdot \boldsymbol{n}_f \, d\Gamma\right) \boldsymbol{n}_f \quad \text{on} \quad \Gamma_{AV} \times (0, T), \tag{2.14}$$

  where $R$ is the resistance parameter for the 0-D model that models the upstream in the aortic direction. $p_{AV}$ is the minimum aortic pressure.

  The switch from closed to open is done when the ventricular pressure overcomes the minimum aortic pressure $p_{AV}$. On the other hand the switch from the open to

closed state is done when the net outgoing flow through $\Gamma_{AV}$ becomes negative.

- mitral valve:

  the switching boundary conditions are of the type Dirichlet-Neumann, meaning that when the valve is closed we have a Dirichlet no-slip condition like before, whilst when is open we have a Neumann condition $\sigma_f(\boldsymbol{u}, p)\boldsymbol{n} = -p_{MV}\boldsymbol{n}$, that allows the blood to enter inside the ventricle.

  The switch from closed to open is done when the ventricular pressure becomes smaller than a fixed value $p_{MV}$. On the other hand the closing procedure from open to closed is done when the net outgoing flow through $\Gamma_{MV}$ becomes positive.

Obviously this setting is a big simplification and other more sophisticated models exist [36, 42], but it is sufficient for the purpose of this thesis.

## 2.6. The Electro Fluid Structure Interaction Problem

Finally we can state the complete Electro Fluid Structure Interaction (EFSI) Problem, where for the sake of simplicity we omitted all the initial and boundary conditions, highlighting only the coupling conditions on the Fluid-Structure interface $\Sigma$. Notice that we have written both the kinematic and dynamic conditions in the current configuration. Given $v_0, \boldsymbol{w}_0, \boldsymbol{d}_0, \boldsymbol{u}_0, p_0, I_{app}$ find for $t \in (0, T]$ $v, \boldsymbol{w}, \boldsymbol{d}, \boldsymbol{u}, p$ such that:

$$
\begin{cases}
J\chi C_m \dfrac{\partial v}{\partial t} - \nabla \cdot (JF^{-1}\Sigma_m F^{-T}\nabla v) + \\
\quad + J\chi I_{ion}(v, \boldsymbol{w}) = J\chi I_{app} & \text{in} \quad \hat{\Omega}_s, \\
\dfrac{\partial \boldsymbol{w}}{\partial t} = \boldsymbol{F}_{ion}(v, \boldsymbol{w}) & \text{in} \quad \hat{\Omega}_s, \\
\\
-\Delta \boldsymbol{d}_{ALE} = \boldsymbol{0} & \text{in} \quad \hat{\Omega}_f, \\
\boldsymbol{d}_{ALE} = \boldsymbol{d} & \text{on} \quad \hat{\Sigma}, \\
\Omega_f = \left\{ \boldsymbol{x} \in \mathbb{R}^3 : \boldsymbol{x} = \hat{\boldsymbol{x}} + \boldsymbol{d}_{ALE}, \hat{\boldsymbol{x}} \in \hat{\Omega}_f \right\}, \\
\\
\rho_s \dfrac{\partial^2 \boldsymbol{d}}{\partial t^2} - \nabla \cdot [P_{pas}(\boldsymbol{d}) + P_{act}(\boldsymbol{d}, \boldsymbol{w})] = 0 & \text{in} \quad \hat{\Omega}_s, \\
\\
\boldsymbol{u} = \dfrac{\partial \boldsymbol{d}}{\partial t} & \text{on} \quad \Sigma, \\
\sigma_f(\boldsymbol{u}, p)\boldsymbol{n} = \sigma_s(\boldsymbol{d})\boldsymbol{n} & \text{on} \quad \Sigma, \\
\\
\boldsymbol{u}_{ALE} = \dfrac{\partial \boldsymbol{d}_{ALE}}{\partial t}, \\
\rho_f \left[ \dfrac{\partial \boldsymbol{u}}{\partial t} + ((\boldsymbol{u} - \boldsymbol{u}_{ALE}) \cdot \nabla)\boldsymbol{u} \right] - \nabla \cdot \sigma_f(\boldsymbol{u}, p) = \boldsymbol{0} & \text{in} \quad \Omega_f, \\
\nabla \cdot \boldsymbol{u} = 0 & \text{in} \quad \Omega_f.
\end{cases}
\tag{2.15}
$$

We can also rewrite the EFSI Problem (2.15) making use of the abstract notation introduced in the previous sections. Given $v_0, \boldsymbol{w}_0, \boldsymbol{d}_0, \boldsymbol{u}_0, p_0$ find for $t \in (0, T]$ $v, \boldsymbol{w}, \boldsymbol{d}, \boldsymbol{u}, p$ such that:

$$
\begin{cases}
v = \mathcal{M}(v, \boldsymbol{w}, \boldsymbol{d}) & \text{in} \quad \hat{\Omega}_s, \\
\boldsymbol{w} = \mathcal{I}(v, \boldsymbol{w}) & \text{in} \quad \hat{\Omega}_s, \\
-\Delta \boldsymbol{d}_{ALE} = \boldsymbol{0} & \text{in} \quad \hat{\Omega}_f, \\
\boldsymbol{d} = \mathcal{S}(\boldsymbol{d}, \boldsymbol{w}) & \text{in} \quad \hat{\Omega}_s, \\
(\boldsymbol{u}, p) = \mathcal{F}(\boldsymbol{u}, \boldsymbol{d}_{ALE}, \boldsymbol{d}; \Omega_f) & \text{in} \quad \Omega_f, \\
\\
\boldsymbol{d}_{ALE} = \boldsymbol{d} & \text{on} \quad \hat{\Sigma}, \\
\boldsymbol{u} = \dfrac{\partial \boldsymbol{d}}{\partial t} & \text{on} \quad \Sigma, \\
\sigma_f(\boldsymbol{u}, p)\boldsymbol{n} = \sigma_s(\boldsymbol{d})\boldsymbol{n} & \text{on} \quad \Sigma.
\end{cases}
\tag{2.16}
$$

# 3 | Numerical Model

We first introduce some notation. we denote by $t_0 = 0, t_1 = \Delta t, ...t_{N-1} = (N-1)\Delta t, t_N = T_f$ the discrete equispaced time instants from the starting time 0 to the final time $T_f$. In this work the same time discretization is used both for Electrophysiology and FSI, even though one can also choose a finer discretization for the electrophysiological problem. We denote the discrete variables at different time steps with a subscript, e.g. $\boldsymbol{d_n} \simeq \boldsymbol{d}(t_n)$. For what concerns the approximation of time derivatives we consider a first-order implicit finite difference scheme for all subproblems. Then we linearize the non linear terms in the following ways:

- the non linearity in the monodomain equation is represented by the term $I_{ion}(v, \boldsymbol{w})$, that is non linear in $v$ and $\boldsymbol{w}$, so we can rewrite it as $I_{ion}(v, \boldsymbol{w}) = v\tilde{I}_{ion}(v, \boldsymbol{w})$, where $\tilde{I}_{ion}(v, \boldsymbol{w}) = I_{ion}(v, \boldsymbol{w})/v$ is again a non linear function in $v$ and $\boldsymbol{w}$. Therefore to take into account this non linearity we use a semi-implicit treatment of such term:

  $$I_{ion}(v_{n+1}, \boldsymbol{w}_{n+1}) \to \tilde{I}_{ion}(v_n, \boldsymbol{w}_{n+1})v_{n+1}.$$

  This semi-implicit linearization leads to a bound on $\Delta t$, i.e. $\Delta t \leq C_1$, where $C_1$ is a constant independent of the space discretization $h$, since it is related to a reaction term (whereas the diffusive term has been treated implicitly);

- in the Navier Stokes equations the non linearity of the convective term is treated again in a semi implicit fashion:

  $$((\boldsymbol{u}_{n+1} - \boldsymbol{u}_{ALE,n+1}) \cdot \nabla)\boldsymbol{u}_{n+1} \to ((\boldsymbol{u}_n - \boldsymbol{u}_{ALE,n+1}) \cdot \nabla)\boldsymbol{u}_{n+1}).$$

  This treatment leads again to a bound on $\Delta t$, i.e. $\Delta t \leq C_2 h$, where $C_2$ is a constant independent of the space discretization $h$ [81];

- in the ionic model equations an explicit linearization for the non linear function $F_{ion}(v_{n+1}, \boldsymbol{w}_{n+1})$ is employed:

  $$F_{ion}(v_{n+1}, \boldsymbol{w}_{n+1}) \to F_{ion}(v_n, \boldsymbol{w}_n)),$$

  so that $F_{ion}(v_n, \boldsymbol{w}_n)$ depends only on values computed at the previous time step. Here the bound on $\Delta t$ is again of the form $\Delta t \leq C_3$, where $C_3$ is a constant

independent of the space discretization $h$.

Moreover we will treat explicitly also the following quantities:

- the mechanical feedbacks coming from the structure problem are treated explicitly, i.e. in the Monodomain equation (2.1) and in the computation of the active part $P_{act}$ (2.7) of the First Piola-Kirchhoff Stress Tensor for the Structure Problem we consider the structure displacement $\boldsymbol{d}_n$ at the previous time step, together with all the related quantities: $F_n = I + \nabla \boldsymbol{d}_n$ and $J_n = \det F$. This choice leads to another bound $\Delta t \leq C_4$ where $C_4$ is a constant;
- also for the *geometric condition* (2.10) in the Geometric Problem (2.11) we choose an explicit treatment considering $\boldsymbol{d}_n$ as the value that has to be harmonically extended into the fluid domain. The bound due to this choice is $\Delta t \leq C_5 h$, where $C_5$ is a constant independent of the space discretization $h$;
- for what concerns the resistance boundary condition for the aortic valve, it is treated explicitly in the following way:

$$\sigma_f(\boldsymbol{u}_{n+1}, p_{n+1})\boldsymbol{n}_f = -\left(p_{AV} + R\int_{\Gamma_{AV}} \boldsymbol{u}_n \cdot \boldsymbol{n}_f \, d\Gamma\right)\boldsymbol{n}_f \quad \text{on} \quad \Gamma_{AV}. \tag{3.1}$$

  Also this treatment leads to a condition on $\Delta t$, i.e. $\Delta t \leq C_6$, where $C_6$ is a constant independent of the space discretization $h$.

Finally we can resume all the conditions on $\Delta t$ in a unique condition considering all bounds: $\Delta t \leq min(C_1, C_2 h, C_3, C_4, C_5 h, C_6)$. However, for accuracy purposes, we have to choose a small $\Delta t$ to well describe the fast propagating front associated to the electrophysiology. In practice this $\Delta t$ is small enough to satisfy the bounds cited above.

For the sake of simplicity in the following sections we do not report all the initial and boundary conditions, but for the coupling ones on the Fluid-Structure interface $\Sigma$.

## 3.1. Staggered Scheme with Monolithic treatment for Fluid Structure Interaction

We first present a scheme (in what follows referred to as *Scheme 1* or *Staggered E-Monolithic FSI Scheme*) where the electrophysiology and geometric problems are staggered, whereas the geometrically linearized FSI problem is solved in a Monolithic fashion

(see figure 1.3). The scheme is the following:

*Scheme 1 / Staggered E-Monolithic FSI Scheme.* At each time instant $t^{n+1}$:

1. solve the ionic model equations:

$$\frac{\boldsymbol{w}_{n+1} - \boldsymbol{w}_n}{\Delta t} = \boldsymbol{F}_{ion}(v_n, \boldsymbol{w}_n) \quad \text{in} \quad \hat{\Omega}_s; \tag{3.2}$$

2. solve the monodomain equation using the value $\boldsymbol{w}_{n+1}$ just computed:

$$\begin{aligned} J_n \chi C_m \frac{v_{n+1} - v_n}{\Delta t} - \nabla \cdot (J_n F_n^{-1} \Sigma_m F_n^{-T} \nabla v_{n+1}) + \\ J_n \chi \tilde{I}_{ion}(v_n, \boldsymbol{w}_{n+1}) v_{n+1} = J_n \chi I_{app} \quad \text{in} \quad \hat{\Omega}_s. \end{aligned} \tag{3.3}$$

   *Remark* 2. Notice that in the Electrophysiological Problem (3.2)(3.3) the mechanical feedbacks coming from the structure are present in $F_n = I + \nabla \boldsymbol{d}_n$ and $J_n = \det F_n$ and are treated explicitly. Notice the semi-implicit treatment of $I_{ion}$, computed using $\boldsymbol{w}_{n+1}$ because the ionic equations will be solved before the monodomain one, so $\boldsymbol{w}_{n+1}$ will be at our disposal.

3. Compute the active stress contribution using the displacement at previous time step $\boldsymbol{d}_n$ and the calcium concentration computed above:

$$P_{act} = T_{act}(\boldsymbol{w}_{n+1}, \boldsymbol{d}_n) \frac{F_n \boldsymbol{f} \otimes \boldsymbol{f}}{\sqrt{I_{4f,n}}}; \tag{3.4}$$

4. solve the geometric problem to find the fluid displacement $\boldsymbol{d}_{ALE,n+1}$. This is done extending $\boldsymbol{d}_n|_\Sigma$ in $\hat{\Omega}_f$:

$$\begin{cases} -\Delta \boldsymbol{d}_{ALE,n+1} = \boldsymbol{0} & \text{in} \quad \hat{\Omega}_f, \\ \boldsymbol{d}_{ALE,n+1} = \boldsymbol{d}_n & \text{on} \quad \hat{\Sigma}; \end{cases} \tag{3.5}$$

5. update the fluid domain and $\boldsymbol{u}_{ALE,n+1}$:

$$\Omega_{f,n+1} = \left\{ \boldsymbol{x} \in \mathbb{R}^3 : \boldsymbol{x} = \hat{\boldsymbol{x}} + \boldsymbol{d}_{ALE,n+1}(\hat{\boldsymbol{x}}), \hat{\boldsymbol{x}} \in \hat{\Omega}_f \right\}, \tag{3.6}$$

$$\boldsymbol{u}_{ALE,n+1} = \frac{\boldsymbol{d}_{ALE,n+1} - \boldsymbol{d}_{ALE,n}}{\Delta t};$$

6. solve the FSI problem in a Monolithic fashion, considering the new current fluid domain $\Omega_{f,n+1}$ and the reference structure domain $\hat{\Omega}_s$:

$$\begin{cases} \rho_s \dfrac{\boldsymbol{d}_{n+1} - 2\boldsymbol{d}_n + \boldsymbol{d}_{n-1}}{\Delta t^2} + \\ \quad -\nabla \cdot [P_{pas}(\boldsymbol{d}_{n+1}) + P_{act}(\boldsymbol{d}_n, \boldsymbol{w}_{n+1})] = 0 & \text{in} \quad \hat{\Omega}_s, \\ \\ \boldsymbol{u}_{n+1} = \dfrac{\boldsymbol{d}_{n+1} - \boldsymbol{d}_n}{\Delta t} & \text{on} \quad \Sigma_{n+1}, \\ \\ \sigma_f(\boldsymbol{u}_{n+1}, p_{n+1})\boldsymbol{n} = \sigma_s(\boldsymbol{d}_{n+1})\boldsymbol{n} & \text{on} \quad \Sigma_{n+1}, \\ \\ \rho_f \left[ \dfrac{\boldsymbol{u}_{n+1} - \boldsymbol{u}_n}{\Delta t} + ((\boldsymbol{u}_n - \boldsymbol{u}_{ALE,n+1}) \cdot \nabla)\boldsymbol{u}_{n+1} \right] + \\ \quad -\nabla \cdot \sigma_f(\boldsymbol{u}_{n+1}, p_{n+1}) = \boldsymbol{0} & \text{in} \quad \Omega_{f,n+1}, \\ \\ \nabla \cdot \boldsymbol{u}_{n+1} = 0 & \text{in} \quad \Omega_{f,n+1}. \end{cases} \tag{3.7}$$

*Remark* 3. Notice the semi-implicit treatment of non linearities described at the beginning of the chapter. The FSI problem is still non-linear, due to the structure constitutive law. The coupling conditions are imposed on the interface $\Sigma_{n+1}$, whilst the geometric condition is treated explicitly and the geometric problem is solved before the FSI problem, see step 4-5.

Concerning the space discretization we make use of the Finite Element method. We use hexaedral elements for all problems and trilinear polynomial basis functions.

Overall, the discretization procedure leads to four different linear systems to be solved:

- Ionic Linear System: leads to an ODEs system for every point of the mesh, solved with a direct solver;
- Monodomain Linear System: leads to a Mass matrix and a Stiffness matrix. It is solved with the conjugate gradient (CG) preconditioned with algebraic multigrid (AMG);

- Geometric Linear System: leads to a Stiffness matrix and it is solved with the conjugate gradient (CG) preconditioned with algebraic multigrid (AMG);
- FSI Non-linear System: linearized with Newton and solved with GMRES preconditioned with a block-based lower-triangular preconditioner.

## 3.2. Staggered Scheme with Implicit Partitioned Robin-Neumann treatment for Fluid Structure Interaction

In this section we will present an alternative scheme to solve the EFSI Problem. Here, we make a first step toward a fully loosely-coupled scheme, by introducing the implicit Robin-Neumann scheme for FSI. Such scheme is based on the idea of considering a Robin interface condition, i.e. a linear combination of the coupling conditions (2.12e) (2.12f) for Fluid Structure Interaction.

Therefore, considering a coefficient $\alpha_f$, we can write the Robin condition:

$$\alpha_f \boldsymbol{u} + \sigma_f(\boldsymbol{u}, p)\boldsymbol{n} = \alpha_f \frac{\partial \boldsymbol{d}}{\partial t} + \sigma_s(\boldsymbol{d})\boldsymbol{n} \text{ on } \Sigma. \tag{3.8}$$

This condition can replace the *kinematic condition* (2.12e) ensuring the same solution of the FSI problem.

The idea is to consider a scheme where the fluid problem is equipped with the Robin condition (3.8) and the structure is equipped with a Neumann condition (2.12f) (notice that the Neumann condition can be seen as a Robin condition with the coefficient set to 0) to ensure the correct exchange of information at the interface $\Sigma$. This second way (referred to as *Scheme 2* or *Staggered E-Partitioned FSI Scheme*) to solve the EFSI problem is exactly the same as before, but for the FSI part that is now split in two problems (the fluid problem and the structure problem) that are solved iteratively in a loop until convergence at fixed time $t^{n+1}$. Due to the presence of such loop, we introduce the superscript $^{(k)}$ (e.g. $\boldsymbol{u}_{n+1}^{(k)}$) to denote the number of iterations in the loop. We consider also a maximum number of iterations $K_{max}$ and a stopping criterion, based on the norm of the increment of the structure displacement: $||\boldsymbol{d}^k - \boldsymbol{d}^{k-1}||_{L^2} > \epsilon$. The scheme is the following:

*Scheme 2/Staggered E-Partitioned FSI Scheme.* At each time instant $t^{n+1}$:

1. the same as in *Scheme 1*, see (3.2);
2. the same as in *Scheme 1*, see (3.3);
3. the same as in *Scheme 1*, see (3.4);
4. the same as in *Scheme 1*, see (3.5);
5. the same as in *Scheme 1*, see (3.6);
6. ***for*** $(0 < k < K_{max}$ and $||\boldsymbol{d}^k - \boldsymbol{d}^{k-1}||_{L^2} > \epsilon)$ solve iteratively:

   6a. solve the fluid problem equipped with a Robin condition on the interface $\Sigma_{n+1}$:

$$\begin{cases} \rho_f \left[ \dfrac{\boldsymbol{u}_{n+1}^{(k)} - \boldsymbol{u}_n}{\Delta t} + ((\boldsymbol{u}_n - \boldsymbol{u}_{ALE,n+1}) \cdot \nabla)\boldsymbol{u}_{n+1}^{(k)} \right] + \\ \quad -\nabla \cdot \sigma_f(\boldsymbol{u}_{n+1}^{(k)}, p_{n+1}^{(k)}) = \boldsymbol{0} \qquad \text{in} \quad \Omega_{f,n+1}, \\ \\ \alpha_f \boldsymbol{u}_{n+1}^{(k)} + \sigma_f(\boldsymbol{u}_{n+1}^{(k)}, p_{n+1}^{(k)})\boldsymbol{n} = \alpha_f \dfrac{\boldsymbol{d}_{n+1}^{(k-1)} - \boldsymbol{d}_n}{\Delta t} + \sigma_s(\boldsymbol{d}_{n+1}^{(k-1)})\boldsymbol{n} \quad \text{on} \quad \Sigma_{n+1}; \end{cases} \tag{3.9}$$

   6b. solve the structure problem equipped with a Neumann condition on the interface $\Sigma_{n+1}$:

$$\begin{cases} \rho_s \dfrac{\boldsymbol{d}_{n+1}^{(k)} - 2\boldsymbol{d}_n + \boldsymbol{d}_{n-1}}{\Delta t^2} + \\ \quad -\nabla \cdot \left[ P_{pas}(\boldsymbol{d}_{n+1}^{(k)}) + P_{act}(\boldsymbol{d}_n, \boldsymbol{w}_{n+1}) \right] = 0 \quad \text{in} \quad \hat{\Omega}_s, \\ \\ \sigma_s(\boldsymbol{d}_{n+1}^{(k)})\boldsymbol{n} = \sigma_f(\boldsymbol{u}_{n+1}^{(k)}, p_{n+1}^{(k)})\boldsymbol{n} \qquad \text{on} \quad \Sigma_{n+1}. \end{cases} \tag{3.10}$$

*Remark* 4. The same semi-implicit treatment of the non linear terms is performed but now the FSI problem has been split into one linear fluid problem and one non-linear structure problem. Therefore, we can solve the fluid problem with GMRES (without needing to resort to a Newton solver). Conversely, the structure problem is still non linear, due to the Guccione constitutive law, and Newton is still employed.

From the algebraic point of view, after the same space discretization described before, we have:

- Ionic Linear System: leads to an ODEs system for every point of the mesh, solved with a direct solver;
- Monodomain Linear System: leads to a Mass matrix and a Stiffness matrix. It

is solved with conjugate gradient (CG) preconditioned with algebraic multigrid (AMG);

- Geometric Linear System: leads to a Stiffness matrix and it is solved with the conjugate gradient (CG) preconditioned with algebraic multigrid (AMG);
- Fluid Linear System: solved many times with GMRES until convergence in a loop with the structure problem;
- Structure Non-linear System: linearized with Newton and solved many times with GMRES until convergence in a loop with the fluid problem.

## 3.3. Loosely-coupled Scheme for Electro Fluid Structure Interaction

Finally we present the new scheme proposed in this study, i.e. the *Loosely Coupled EFSI Scheme* (or *Scheme 3*). The situation is exactly the same as before (i.e. *Scheme 2*) except for the fact that here we perform only one iteration of the FSI Robin-Neumann loop described above (for this reason, the superscript $^{(k)}$ is dropped). This leads to the following scheme:

*Scheme 3/Loosely Coupled EFSI Scheme.* At each time instant $t^{n+1}$:

1. the same as in *Scheme 1*, see (3.2);
2. the same as in *Scheme 1*, see (3.3);
3. the same as in *Scheme 1*, see (3.4);
4. the same as in *Scheme 1*, see (3.5);
5. the same as in *Scheme 1*, see (3.6);
6. solve the fluid problem equipped with a Robin condition on the interface $\Sigma_{n+1}$:

$$\begin{cases} \rho_f \left[ \dfrac{\boldsymbol{u}_{n+1} - \boldsymbol{u}_n}{\Delta t} + ((\boldsymbol{u}_n - \boldsymbol{u}_{ALE,n+1}) \cdot \nabla)\boldsymbol{u}_{n+1} \right] + \\ \quad -\nabla \cdot \sigma_f(\boldsymbol{u}_{n+1}, p_{n+1}) = \boldsymbol{0} \qquad \text{in} \quad \Omega_{f,n+1}, \\ \\ \alpha_f \boldsymbol{u}_{n+1} + \sigma_f(\boldsymbol{u}_{n+1}, p_{n+1})\boldsymbol{n} = \alpha_f \dfrac{\boldsymbol{d}_n - \boldsymbol{d}_{n-1}}{\Delta t} + \sigma_s(\boldsymbol{d}_n)\boldsymbol{n} \quad \text{on} \quad \Sigma_{n+1}; \end{cases} \tag{3.11}$$

7. solve the structure problem equipped with a Neumann condition on the interface $\Sigma_{n+1}$:

$$\begin{cases} \rho_s \dfrac{\boldsymbol{d}_{n+1} - 2\boldsymbol{d}_n + \boldsymbol{d}_{n-1}}{\Delta t^2} + \\ \quad -\nabla \cdot [P_{pas}(\boldsymbol{d}_{n+1}) + P_{act}(\boldsymbol{d}_n, \boldsymbol{w}_{n+1})] = 0 \quad \text{in} \quad \hat{\Omega}_s, \\ \\ \sigma_s(\boldsymbol{d}_{n+1})\boldsymbol{n} = \sigma_f(\boldsymbol{u}_{n+1}, p_{n+1})\boldsymbol{n} \qquad\qquad \text{on} \quad \Sigma_{n+1}. \end{cases} \tag{3.12}$$

*Remark* 5. Again the same semi-implicit treatment of the non linear terms is performed and the FSI problem has been split into one linear fluid problem and one non-linear structure problem. Therefore also here we need to use a Newton solver for the structure problem.

From the algebraic point of view, after the same space discretization described before, we have:

- Ionic Linear System: leads to an ODEs system for every point of the mesh, solved with a direct solver;
- Monodomain Linear System: leads to a Mass matrix and a Stiffness matrix. It is solved with conjugate gradient (CG) preconditioned with algebraic multigrid (AMG);
- Geometric Linear System: leads to a Stiffness matrix and it is solved with conjugate gradient (CG) preconditioned with algebraic multigrid (AMG);
- Fluid Linear System: solved once per time step with GMRES;
- Structure Non-linear System: linearized with Newton and solved once per time step with GMRES.

## 3.4. Algorithms

We can finally resume the three algorithms making use of the compact operators defined in chapter 2.

---

Algorithm 3.1 *Scheme 1/Staggered E-Monolithic FSI Scheme*

---

1: Solve the ionic model equations:

$$\boldsymbol{w}_{n+1} = \mathcal{I}(v_n, \boldsymbol{w}_n) \quad \text{in} \quad \hat{\Omega}_s; \tag{3.13}$$

2: solve the monodomain equations:

$$v_{n+1} = \mathcal{M}(v_n, \boldsymbol{d}_n, \boldsymbol{w}_{n+1}) \quad \text{in} \quad \hat{\Omega}_s; \tag{3.14}$$

3: compute the active stress:

$$P_{act} = \mathcal{T}(\boldsymbol{d}_n, \boldsymbol{w}_{n+1}); \tag{3.15}$$

4: solve the geometric problem:

$$\begin{cases} -\Delta \boldsymbol{d}_{ALE,n+1} = \boldsymbol{0} & \text{in} \quad \hat{\Omega}_f, \\ \boldsymbol{d}_{ALE,n+1} = \boldsymbol{d}_n & \text{on} \quad \hat{\Sigma}; \end{cases} \tag{3.16}$$

5: compute the current domain and $\boldsymbol{u}_{ALE,n+1}$:

$$\Omega_{f,n+1} = \left\{ \boldsymbol{x} \in \mathbb{R}^3 : \boldsymbol{x} = \hat{\boldsymbol{x}} + \boldsymbol{d}_{ALE,n+1}(\hat{\boldsymbol{x}}), \hat{\boldsymbol{x}} \in \hat{\Omega}_f \right\},$$

$$\boldsymbol{u}_{ALE,n+1} = \frac{\boldsymbol{d}_{ALE,n+1} - \boldsymbol{d}_{ALE,n}}{\Delta t};$$

6: solve the non linear FSI problem in a Monolithc fashion:

$$\begin{cases} \boldsymbol{d}_{n+1} = \mathcal{S}(\boldsymbol{d}_{n+1}, \boldsymbol{w}_{n+1}, \boldsymbol{d}_n) & \text{in} \quad \hat{\Omega}_s, \\ \boldsymbol{u}_{n+1} = \dfrac{\boldsymbol{d}_{n+1} - \boldsymbol{d}_n}{\Delta t} & \text{on} \quad \Sigma_{n+1}, \\ \sigma_f(\boldsymbol{u}_{n+1}, p_{n+1})\boldsymbol{n} = \sigma_s(\boldsymbol{d}_{n+1})\boldsymbol{n} & \text{on} \quad \Sigma_{n+1}, \\ (\boldsymbol{u}_{n+1}, p_{n+1}) = \mathcal{F}(\boldsymbol{u}_n, \boldsymbol{d}_{ALE,n+1}, \boldsymbol{d}_n; \Omega_{f,n+1}) & \text{in} \quad \Omega_{f,n+1}. \end{cases} \tag{3.17}$$

7: $t_n \to t_{n+1}$

---

Algorithm 3.2 *Scheme 2/Staggered E-Partitioned FSI Scheme*

1: Solve the ionic model equations:

$$\boldsymbol{w}_{n+1} = \mathcal{I}(v_n, \boldsymbol{w}_n) \quad \text{in} \quad \hat{\Omega}_s; \tag{3.18}$$

2: solve the monodomain equations:

$$v_{n+1} = \mathcal{M}(v_n, \boldsymbol{d}_n, \boldsymbol{w}_{n+1}) \quad \text{in} \quad \hat{\Omega}_s; \tag{3.19}$$

3: compute the active stress:

$$P_{act} = \mathcal{T}(\boldsymbol{d}_n, \boldsymbol{w}_{n+1}); \tag{3.20}$$

4: solve the geometric problem:

$$\begin{cases} -\Delta \boldsymbol{d}_{ALE,n+1} = \boldsymbol{0} & \text{in} \quad \hat{\Omega}_f, \\ \boldsymbol{d}_{ALE,n+1} = \boldsymbol{d}_n & \text{on} \quad \hat{\Sigma}; \end{cases} \tag{3.21}$$

5: compute the current domain and $\boldsymbol{u}_{ALE,n+1}$:

$$\Omega_{f,n+1} = \left\{ \boldsymbol{x} \in \mathbb{R}^3 : \boldsymbol{x} = \hat{\boldsymbol{x}} + \boldsymbol{d}_{ALE,n+1}(\hat{\boldsymbol{x}}), \hat{\boldsymbol{x}} \in \hat{\Omega}_f \right\},$$
$$\boldsymbol{u}_{ALE,n+1} = \frac{\boldsymbol{d}_{ALE,n+1} - \boldsymbol{d}_{ALE,n}}{\Delta t};$$

6: ***for*** $( 0 < k < K_{max}$ and $||\boldsymbol{d}^k - \boldsymbol{d}^{k-1}||_{L^2} > \epsilon)$ :

6a: solve the fluid problem equipped with a Robin condition:

$$\begin{cases} (\boldsymbol{u}_{n+1}^{(k)}, p_{n+1}^{(k)}) = \mathcal{F}(\boldsymbol{u}_n, \boldsymbol{d}_{ALE,n+1}, \boldsymbol{d}_n; \Omega_{f,n+1}) & \text{in} \quad \Omega_{f,n+1}, \\ \alpha_f \boldsymbol{u}_{n+1}^{(k)} + \sigma_f(\boldsymbol{u}_{n+1}^{(k)}, p_{n+1}^{(k)})\boldsymbol{n} = \alpha_f \dfrac{\boldsymbol{d}_{n+1}^{(k-1)} - \boldsymbol{d}_n}{\Delta t} + \sigma_s(\boldsymbol{d}_{n+1}^{(k-1)})\boldsymbol{n} & \text{on} \quad \Sigma_{n+1}; \end{cases} \tag{3.22}$$

6b: solve the non linear structure problem equipped with a Neumann condition:

$$\begin{cases} \boldsymbol{d}_{n+1}^{(k)} = \mathcal{S}(\boldsymbol{d}_{n+1}^{(k)}, \boldsymbol{w}_{n+1}, \boldsymbol{d}_n) & \text{in} \quad \hat{\Omega}_s, \\ \sigma_s(\boldsymbol{d}_{n+1}^{(k)})\boldsymbol{n} = \sigma_f(\boldsymbol{u}_{n+1}^{(k)}, p_{n+1}^{(k)})\boldsymbol{n} & \text{on} \quad \Sigma_{n+1}. \end{cases} \tag{3.23}$$

7: ***end for***

8: $t_n \to t_{n+1}$

Algorithm 3.3 *Scheme 3/Loosely Coupled EFSI Scheme*

1: Solve the ionic model equations:

$$\boldsymbol{w}_{n+1} = \mathcal{I}(v_n, \boldsymbol{w}_n) \quad \text{in} \quad \hat{\Omega}_s; \tag{3.24}$$

2: solve the monodomain equations:

$$v_{n+1} = \mathcal{M}(v_n, \boldsymbol{d}_n, \boldsymbol{w}_{n+1}) \quad \text{in} \quad \hat{\Omega}_s; \tag{3.25}$$

3: compute the active stress:

$$P_{act} = \mathcal{T}(\boldsymbol{d}_n, \boldsymbol{w}_{n+1}); \tag{3.26}$$

4: solve the geometric problem:

$$\begin{cases} -\Delta \boldsymbol{d}_{ALE,n+1} = \boldsymbol{0} & \text{in} \quad \hat{\Omega}_f, \\ \boldsymbol{d}_{ALE,n+1} = \boldsymbol{d}_n & \text{on} \quad \hat{\Sigma}; \end{cases} \tag{3.27}$$

5: compute the current domain and $\boldsymbol{u}_{ALE,n+1}$:

$$\Omega_{f,n+1} = \left\{ \boldsymbol{x} \in \mathbb{R}^3 : \boldsymbol{x} = \hat{\boldsymbol{x}} + \boldsymbol{d}_{ALE,n+1}(\hat{\boldsymbol{x}}), \hat{\boldsymbol{x}} \in \hat{\Omega}_f \right\},$$
$$\boldsymbol{u}_{ALE,n+1} = \frac{\boldsymbol{d}_{ALE,n+1} - \boldsymbol{d}_{ALE,n}}{\Delta t};$$

6: solve the fluid problem equipped with a Robin condition:

$$\begin{cases} (\boldsymbol{u}_{n+1}, p_{n+1}) = \mathcal{F}(\boldsymbol{u}_n, \boldsymbol{d}_{ALE,n+1}, \boldsymbol{d}_n; \Omega_{f,n+1}) & \text{in} \quad \Omega_{f,n+1}, \\ \alpha_f \boldsymbol{u}_{n+1} + \sigma_f(\boldsymbol{u}_{n+1}, p_{n+1})\boldsymbol{n} = \alpha_f \dfrac{\boldsymbol{d}_n - \boldsymbol{d}_{n-1}}{\Delta t} + \sigma_s(\boldsymbol{d}_n)\boldsymbol{n} & \text{on} \quad \Sigma_{n+1}; \end{cases} \tag{3.28}$$

7: solve the non linear structure problem equipped with a Neumann condition:

$$\begin{cases} \boldsymbol{d}_{n+1} = \mathcal{S}(\boldsymbol{d}_{n+1}, \boldsymbol{w}_{n+1}, \boldsymbol{d}_n) & \text{in} \quad \hat{\Omega}_s, \\ \sigma_s(\boldsymbol{d}_{n+1})\boldsymbol{n} = \sigma_f(\boldsymbol{u}_{n+1}, p_{n+1})\boldsymbol{n} & \text{on} \quad \Sigma_{n+1}. \end{cases} \tag{3.29}$$

8: $t_n \to t_{n+1}$

Finally, we can define a fourth *Scheme 4*, where the steps 1-5 are again the same as *Scheme 1*: (3.2), (3.3), (3.4), (3.5), (3.6), and the FSI part is treated as *Scheme 2*: (3.9), (3.10) but fixing $K_{max} = 2$.

# 4 | On the choice of simulation parameters: methods and results

## 4.1. Mesh and common parameters

### 4.1.1. On the choice of the mesh

The first important thing to do to run a simulation is to discretize the computational domain with a mesh. For all the simulations we have used hexahedral elements, in particular we chose a conforming mesh (i.e. the degrees of freedom on the Fluid Structure interface are the same for both fluid and structure meshes) to ease the treatment of the Fluid Structure Interaction coupling conditions. Moreover we use a nested and finer structure mesh to solve the Electrophysiological Problem, indeed this second and finer mesh is needed to capture the spreading of the the transmembrane potential due to the sharpness of the propagating wave front. The refinement was done in an octree fashion, dividing every hexahedron in eight smaller elements [2, 25]. The computational domain and the associated mesh are shown in figure 4.1.

(a) Above view of the mesh. (b) Lateral view of the domain cross section . (c) Lateral view of the domain.

Figure 4.1: Some views of the mesh of the computational domain.

### 4.1.2. On the choice of common parameters

Here we indicate some choices of parameters that have been used in all the numerical simulations:

- for what concerns the choice of $\Delta t$ we need to take into account the accuracy requirements of FSI and electrophysiology discussed at the beginning of Chapter 3, so we have chosen $\Delta t = 2 \cdot 10^{-4} s$ for all problems; in what follows also $\Delta t = 10^{-4} s$ has been used for further investigations. These choices are small enough to solve both issues associated with the choice of $\Delta t$: satisfy the bound given by linearizations and well describe the fast propagating front characterizing the Electrophysiological problem. In general the simulations have been run from time $t_0 = 0s$ to $T_f = 0.5s$, starting with the isovolumic contraction;
- the pressure at which we load the initial configuration is $1333 Pa$; we used the same value for $p_{MV}$, defined in the valves boundary conditions Section 2.5.3. On the other hand $p_{AV} = 9000 Pa$, i.e. the pressure at which the aortic valve opens;
- the degree of the finite element spaces is 1 for all the problems;
- our truncated ellipsoid has three semiaxes: two equal ones measuring $b = 2.5\ cm$ and the longest one measuring $a = 6\ cm$, the thickness of the wall measures $0.8\ cm$;
- the densities of fluid and structure are $\rho_f = 1.06 \cdot 10^3 \frac{Kg}{m^3}$ and $\rho_s = 10^3 \frac{Kg}{m^3}$ respectively, whilst the fluid viscosity is $\mu_f = 3.5 \cdot 10^{-3} Pa \cdot s$;
- since the blood flow in a healthy heart is characterized by a regime of transition to

turbulence, we have also used a SUPG-PSUPG stabilization for the Navier-Stokes equations, together with VMS-LES model for turbulence [17, 19, 30, 41, 67, 102].

- All the simulations were performed using 1 cluster node with 20 cores, with Intel Xeon E5-2640 processors, for a total of 20 processes executing in parallel. Each node had 64GB of RAM available.

## 4.2. Schemes, scenarios and notation

We recall that in Chapter 3 we have defined four schemes to solve our EFSI problem: *Scheme 1* (*S1*: 3.1), *Scheme 2* (*S2*: 3.2), *Scheme 3* (*S3*: 3.3) and *Scheme 4* (*S4*: same as *S2* but with $K_{max} = 2$).

Moreover we will consider two different scenarios, identified by their own parameters settings:

- the *Guccione setting*, where we use the non-linear anisotropic Guccione law for the structure, together with visco-elastic boundary conditions for the pericardium;
- the *Hooke setting*, where we use a linear isotropic law for the structure, together with simplified Robin boundary conditions for the pericardium.

For the sake of simplicity in what follows we will indicate the simulations of the two settings using the four different schemes as follows:

- *G-j* with $j = 1, 2, 3, 4$ to indicate the simulation of the *Guccione setting* using *Scheme j*.
- *H-j* with $j = 1, 2, 3, 4$ to indicate the simulation of the *Hooke setting* using *Scheme j*.

Finally, for the calibration of the parameters used in the different scenarios and to establish the goodness of the numerical results using the 4 different schemes, we will always keep in mind the pursuit of reproducing a behavior closer as possible to the physiological one. In particular, we aimed at reproducing physiological behaviors for the following indicators:

(i) $p_{max}$: the maximum average pressure of the ventricular chamber during the simulation;

(ii) the ejection fraction, i.e. the percentage quantity of blood ejected by the ventricle defined as:

$$E_f(\%) = \frac{V_{f,MAX} - V_{f,min}}{V_{f,MAX}} \cdot 100, \tag{4.1}$$

where $V_{f,MAX}$ is the maximum volume of the ventricular chamber and $V_{f,min}$ is the minimum volume of the ventricular chamber;

(iii) $Time_{act}$: the duration of the electrical activation;

(iv) $max||\boldsymbol{u}||$: the peak blood velocity magnitude of blood. The maximum value is computed considering both space and time;

(v) for the first isovolumic phase, i.e. the isovolumic contraction, we define a percentage indicator that represents the numerical loss/gain of the ventricular chamber volume during the isovolumic phase, the Isovolumic Loss Indicator:

$$ILI_C(\%) = \left| \frac{V_{iso,iC} - V_{iso,fC}}{max\left\{V_{iso,iC}, V_{iso,fC}\right\}} \right| \cdot 100, \tag{4.2}$$

where $V_{iso,iC}$ and $V_{iso,fC}$ are the ventricular chamber volumes at the beginning and at the end of the isovolumic contraction phase, which begins at the start of the simulation and terminates when the aortic valve opens;

(vi) for the second isovolumic phase, i.e. isovolumic relaxation we define an analogous percentage indicator:

$$ILI_R(\%) = \left| \frac{V_{iso,iR} - V_{iso,fR}}{max\left\{V_{iso,iR}, V_{iso,fR}\right\}} \right| \cdot 100, \tag{4.3}$$

where $V_{iso,iR}$ and $V_{iso,fR}$ are the ventricular chamber volumes at the beginning and at the end of the isovolumic relaxation phase, which starts when the aortic valve closes and terminates when the mitral valve opens.

(vii) We finally define also the opening/closing time of the valves:

- $T_{O,A}$: the the opening time of the aortic valve;
- $T_{C,A}$: the closing time of the aortic valve;
- $T_{O,M}$: the opening time of the mitral valve.

Therefore (i)-(vii) have to satisfy the following requirements:

I for (i): $120mmHg \leq p_{max} \leq 130mmHg$;

II for (ii): $E_f \geq 50.01\%$;

III for (iii): $Time_{act} \simeq 90ms$;

IV for (iv): $||\boldsymbol{u}|| \leq 2m/s$;

V we need to well describe the physiological variations among the 4 cardiac phases described in Section 1.4. In particular the indicators (v) and (vi) need to be smaller as possible to obtain a precise numerical description of the isovolumic phases. Finally, we need to obtain the physiological opening/closing of the valves (vii) to obtain a simulation that describes a physiological behavior. We do not impose precise time requirements for such opening/closing, but must happen.

Finally we will define the CPU time needed to carry on the simulation: $CPU_{fTime}$

## 4.3. Calibration of the *Guccione setting*

We first calibrate the parameters of the *Guccione setting*, to obtain a simulation *G-1* that reproduces a behavior closer as possible to the physiological one described by requirements I-V. The parameters to be tuned are the following:

- the conductivities in the three directions identified by the fibers: $\Sigma_m^l$, $\Sigma_m^t$, $\Sigma_m^n$. These three conductivities are embedded inside the tensor $\Sigma_m$ of the Monodomain Equation (2.1) and represent the conduction velocities in the fibers' direction and in its orthoganal directions. These parameters deeply influence the Electrophysiological behavior; indeed, some studies have been carried on the identification of physiological ranges for such parameters [95]. In the present work are tuned to obtain a full activation of the structure $Time_{act} \simeq 90ms$, as mentioned in requirement I;

- pericardium boundary conditions parameters. As seen in section 2.4, the pericardium is modelled by means of a visco-elastic condition with 4 different parameters: $K_\perp, K_\parallel, C_\perp, C_\parallel$, see (2.5). Since they influence the ejection fraction (i) and also the ventricular chamber average pressure (ii) and the blood velocity (iv), we need to calibrate them to obtain the physiological behavior described above;

- resistance boundary condition: the parameter $R$ used to model the resistance boundary condition at the outflow of the aortic valve, see (2.14). This parameter mainly influences the ejection fraction (i), being a resistance to blood flow at the outlet;

- maximum tension $\xi$: this parameter comes into play in the computation of the active part of the Piola-Kirchhoff stress tensor $P_{act}$ of the structure, see (2.8); in particular $P_{act}$ depends linearly on $\xi$ and we can express such relation between $P_{act}$

and $\xi$ as follows: $P_{act} = \xi \mathcal{T}_{act}$, with $\mathcal{T}_{act}$ coming from the activation model $RDQ18$, as discussed in Section 2.4 (for more details refer the reader to [87, 88, 90]). This parameter represents the contractility of the myocardium and, being related to the force generated by the active contraction, influences different indicators such as blood velocity (iv) and pressure (i), together with the ejection fraction (ii) of the ventricle.

The calibration of such parameters was performed manually; indeed, starting from reasonable initial guesses, we have followed a procedure of trial and error executing subsequent simulations to match all the requirements I-V up to an error of $\sim 1\%$. Due to the implicit nature of *Scheme 1*, we will use the solution *G-1* as the reference one for all the simulations obtained with the *Guccione setting* [21, 27].

In table 4.1 we haved summarized all the calibrated parameters for the *Guccione setting* described above, while in table 4.2 are presented the physiological indicators (i)-(vii) obtained with *G-1* that have to satisfy the requirements I-V. We have simulated $0.5s$ with $\Delta t = 2 \cdot 10^{-4}$.

| | **Calibrated value** |
|---|---|
| $\Sigma_m^l \ [m^2/s]$ | $1.68 \cdot 10^{-4}$ |
| $\Sigma_m^t \ [m^2/s]$ | $7.69 \cdot 10^{-5}$ |
| $\Sigma_m^n \ [m^2/s]$ | $2.48 \cdot 10^{-5}$ |
| $K_\perp [\frac{Pa}{m}]$ | $10^4$ |
| $K_\parallel [\frac{Pa}{m}]$ | $2 \cdot 10^4$ |
| $C_\perp [\frac{Pa \cdot s}{m}]$ | $2 \cdot 10^4$ |
| $C_\parallel [\frac{Pa \cdot s}{m}]$ | $2 \cdot 10^3$ |
| $\xi \ [Pa]$ | $5 \cdot 10^5$ |
| $R \ [\frac{Kg}{m^4 \cdot s}]$ | $1.3 \cdot 10^7$ |

Table 4.1: Calibrated parameters for the *Guccione setting*.

| | **G-1** |
|---|---|
| $p_{max}$ $[mmHg]$ | 121.17 |
| $E_f$ | 56.95% |
| $Time_{act}$ $[ms]$ | 91 |
| $max\|\|\boldsymbol{u}\|\|$ $[m/s]$ | 1.3 |
| $ILI_C$ | 0.01% |
| $ILI_R$ | 0.01% |
| $T_{O,A}$ $[s]$ | 0.09 |
| $T_{C,A}$ $[s]$ | 0.26 |
| $T_{O,M}$ $[s]$ | 0.366 |
| $CPU_{fTime}$ $[s]$ | 7070 |

Table 4.2: Values of the physiological indicators (i)-(vii) obtained with *G-1* to assess the fulfillment of the requirements I-V. We have simulated $0.5s$, using $\Delta t = 2 \cdot 10^{-4}$.

We can observe from table 4.2 that all the requirements I-V have been satisfied:

1. the maximum pressure, i.e. $p_{max} = 121.17mmHg$, perfectly falls in the range defined in requirement I. Some numerical results for the ventricular chamber average pressure are presented in figure 4.7;
2. the ejection fraction, i.e. $E_f = 56.95\%$, is above our acceptability threshold defined in requirement II;
3. the electrical activation $Time_{act} = 91ms$ matches the objective expressed in requirement III. The activation procedure, i.e. the numerical result of the Electrophysiological problem, can be visualized in figure 4.3;
4. the peak blood velocity magnitude, i.e. $max||\boldsymbol{u}|| = 1.3m/s$, is less than the threshold defined in requirement IV;
5. finally the physiological variations among the 4 cardiac phases are well described by *G-1*; indeed, we have indicated the opening/closing time of the valves, for a visualization od the numerical result see figure 4.5. Moreover the 2 isovolumic phases are perfectly captured as one can see from the Isovolumic Loss Indicators, both equal to 0.01%. A further confirm of this fact can be visualized in figure 4.2a, where the time evolution of the ventricular chamber volume is presented. Therefore, also requirement V has been satisfied.

The time evolution of the ventricular chamber volume and pressure obtained with *G-1* can be visualized in figure 4.2. Some other numerical results are presented in figure 4.6 and figure 4.4.

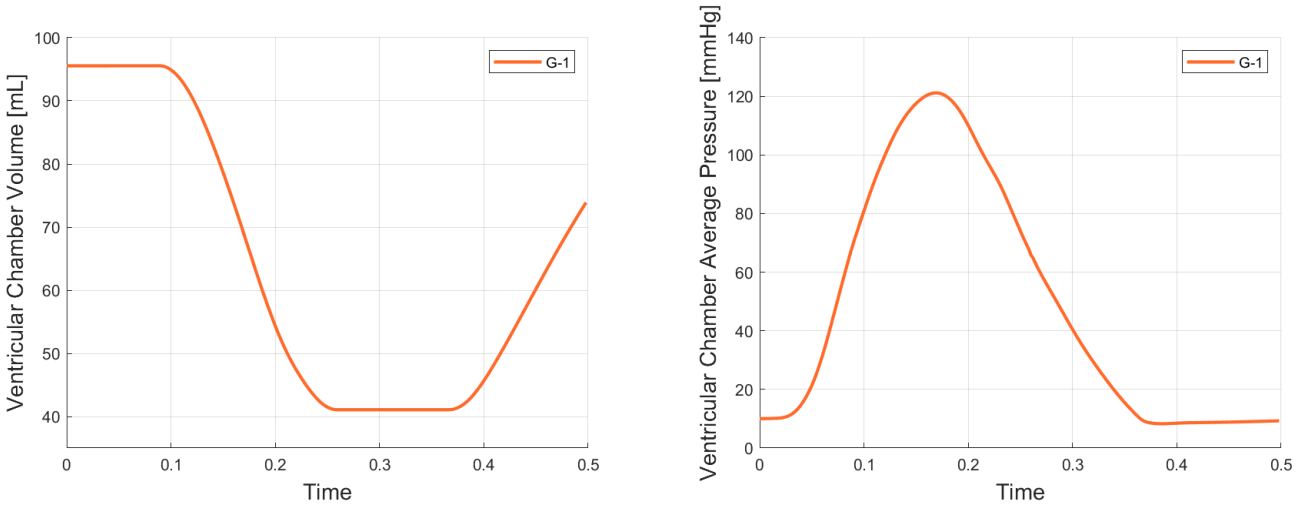


(a) Ventricular chamber volume of *G-1*.

(b) Ventricular chamber average pressure of *G-1*.

Figure 4.2: Time evolution of the ventricular chamber volume and pressure obtained with *G-1*.

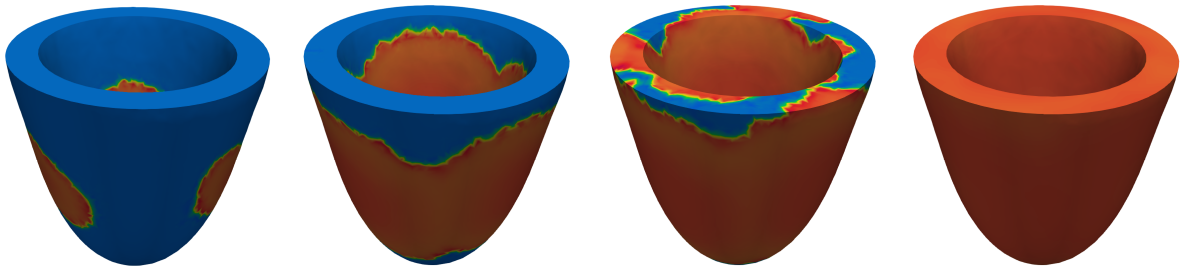

(a) $t = 22ms$: volumetric stimulus.

(b) $t = 52ms$.

(c) $t = 64ms$.

(d) $t = 90ms$: complete activation.

Figure 4.3: Numerical solution obtained with *G-1* for the Electrophysiological Problem at different time instants; we can visualize the propagation of the transmembrane potential $v$.

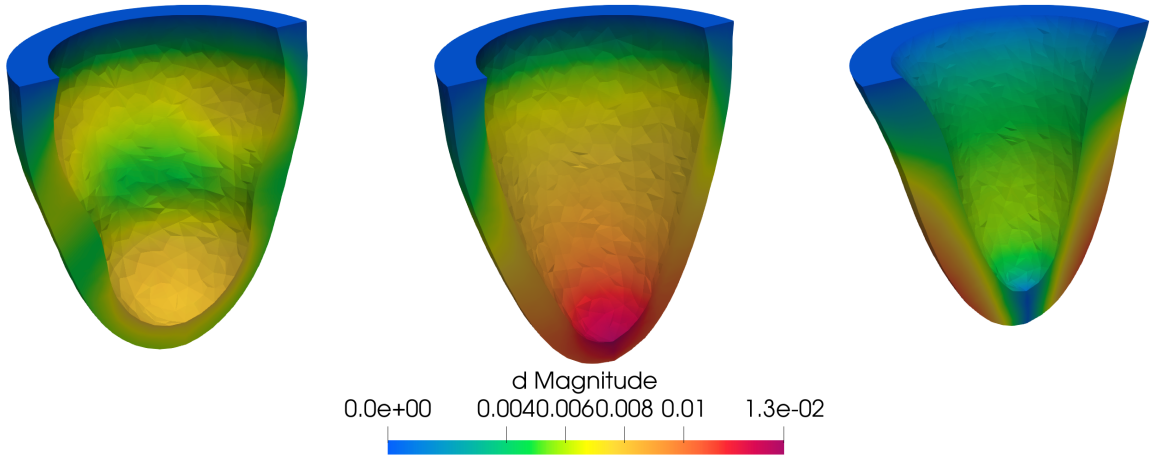


(a) $t = 0.062s$. (b) $t = 0.12s$. (c) $t = 0.286s$.

Figure 4.4: Numerical solution obtained with *G-1* for the structure displacement at different time instants.

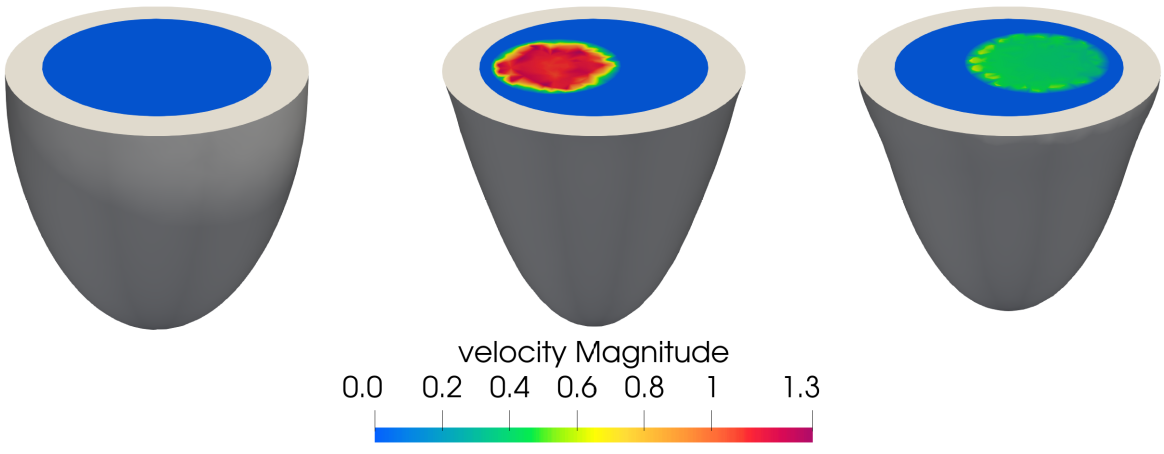


(a) $t = 0s$: both valves closed. (b) $t = 0.18s$: ejection phase. (c) $t = 0.42s$: ventricular filling phase.

Figure 4.5: Numerical solution obtained with *G-1* for the fluid velocity at different time instants.

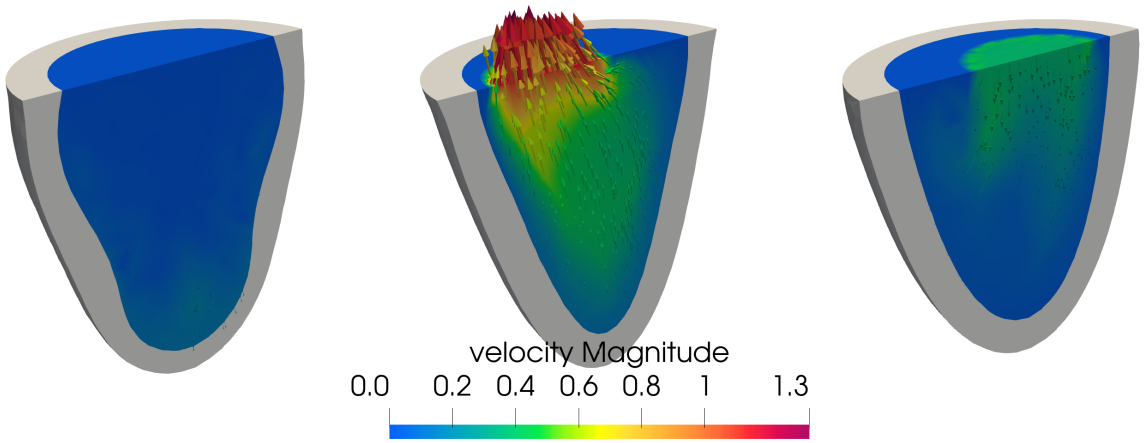


(a) $t = 0.074ss$: isovolumic contraction.

(b) $t = 0.18s$: ejection phase.

(c) $t = 0.49s$: ventricular filling phase.

Figure 4.6: Numerical solution obtained with *G-1* for the fluid velocity at different time instants.

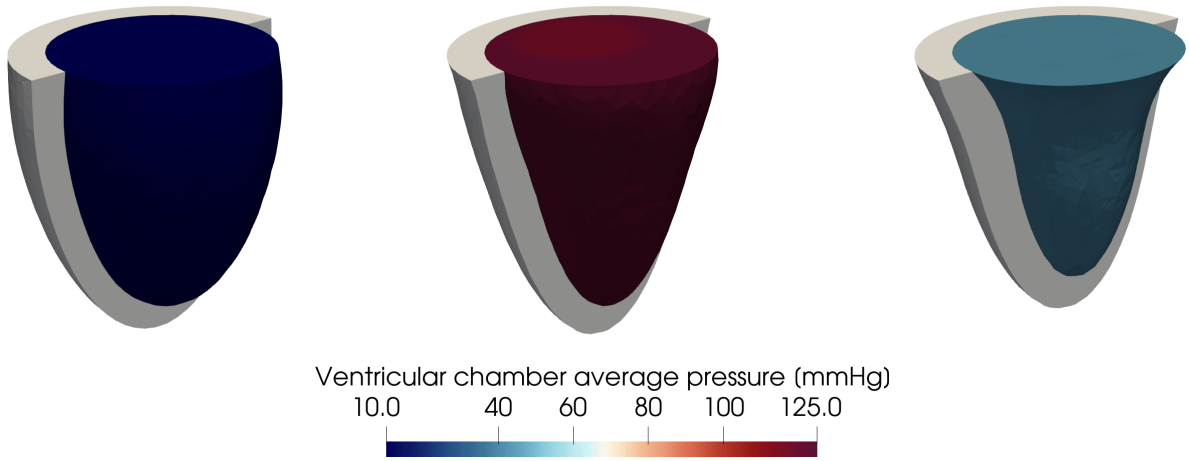


(a) $t = 0s$: the ventricular chamber is loaded at the value $p_{MV} = 1333Pa = 10mmHg$.

(b) $t = 0.17s$: $p_{max} = 121.17mmHg$.

(c) $t = 0.3s$: isovolumic relaxation.

Figure 4.7: Numerical solution of the ventricular chamber pressure obtained with *G-1* at different time instants.

## 4.4. On the choice of the Robin interface parameter $\alpha_f$ for the Robin-Neumann Schemes

Due to the fact that our new *Loosely Coupled EFSI Scheme*, together with *Scheme 2* and *Scheme 4* rely on a partitioned Robin-Neumann scheme for the FSI problem, we need to choose the Robin Interface parameter $\alpha_f$, see (3.8). Therefore, among the different choices of methods to identify such parameter, we will make use of the theory developed in [49–52]. The idea is to use the theoretical values obtained by the convergence analysis of a simplified FSI problem in spherical coordinates for our simulations, exploiting the "almost spherical" morphology of the left ventricle.

### 4.4.1. *Spherical Simplified Model* for the estimation of $\alpha_f$

We present a quick review of the *Spherical Simplified Model* proposed in [49–52] for the choice of a range for $\alpha_f$, i.e. the problem arising from the interaction between an incompressible, inviscid and linear fluid occupying the sphere $\Omega_f = \{\boldsymbol{x} \in \mathbb{R}^3 : x^2 + y^2 + z^2 < R^2\}$ and a linear elastic structure described by the wave equation and occupying the spherical shell $\Omega_s = \{\boldsymbol{x} \in \mathbb{R}^3 : R^2 < x^2 + y^2 + z^2 < (R + H)^2\}$. The two physics are separated by the common interface $\Sigma = \{\boldsymbol{x} \in \mathbb{R}^3 : x^2 + y^2 + z^2 = R^2\}$. The external surface is denoted by $\Sigma_{out}$ and $\boldsymbol{n}$ is the outward unit normal.

The choice of the *Spherical Simplified Model* has been motivated due to these facts:

(i) in this geometry it is possible to write analytic solutions of the Robin-Neumann Problem, allowing us to easily obtain a range of theoretical optimal values for $\alpha_f$;

(ii) the spherical domain is topologically similar to the truncated ellipsoid.

We will make use of this theoretical analysis only to obtain guess values for $\alpha_f$ to use them to simulate our EFSI Problem with the different Robin-Neumann based schemes presented in chapter 3.

Therefore, now we can state the *Spherical Simplified Model*. Considering $\boldsymbol{u}$ the velocity of the fluid, $p$ its pressure, $\boldsymbol{d}$ the displacement of the structure, $\rho_s$ and $\rho_f$ the densities, we can write the following equations:

**Spherical Simplified Model**

$$\begin{cases} \rho_f \dfrac{\partial \boldsymbol{u}}{\partial t} + \nabla p = \mathbf{0} & \text{in} \quad \Omega_f \times (0,T), \\ \nabla \cdot \boldsymbol{u} = 0 & \text{in} \quad \Omega_f \times (0,T), \\ \boldsymbol{u} \cdot \boldsymbol{n} = \dfrac{\partial \boldsymbol{d}}{\partial t} \cdot \boldsymbol{n} & \text{on} \quad \Sigma \times (0,T), \\ -p = \lambda \nabla \boldsymbol{d}\boldsymbol{n} \cdot \boldsymbol{n} & \text{on} \quad \Sigma \times (0,T), \\ \boldsymbol{d} \times \boldsymbol{n} = \mathbf{0} & \text{on} \quad \Sigma \times (0,T), \\ \rho_s \dfrac{\partial^2 \boldsymbol{d}}{\partial t^2} - \lambda \Delta \boldsymbol{d} = 0 & \text{in} \quad \Omega_s \times (0,T), \\ \gamma_{ST} \boldsymbol{d} + \lambda \nabla \boldsymbol{d}\boldsymbol{n} = \mathbf{0} & \text{on} \quad \Sigma_{out} \times (0,T), \\ +\mathit{Initial\ Conditions}. \end{cases} \tag{4.4}$$

*Remark* 6. Notice the presence of the continuity and the dynamic conditions on the interface $\Sigma$, together with a third condition (i.e. $\boldsymbol{d} \times \boldsymbol{n} = \mathbf{0}$) needed due to the inviscid nature of the fluid that leads to a coupling only in the normal direction. Then $\lambda$ summarizes the elastic properties of the structure and $\gamma_{ST}$ is used to reproduce a Robin condition on the external surface of the structure.

We can now state the Implicit Robin-Neumann Algorithm with a first order time discretization. The idea is to split (4.4) in two problems: a fluid problem equipped with a Robin condition and a structure problem equipped with a Neumann condition. They are then solved iteratively in a loop at fixed time $t^{n+1}$, indicating with $^{(k)}$ the k-th iteration of the loop. Therefore the scheme is the following:

given $\boldsymbol{d}_{n+1}^{(0)} = \boldsymbol{d}_n$, for $k \geq 0$ solve iteratively until convergence:

***Fluid Problem***:

$$\begin{cases} \rho_f \dfrac{\boldsymbol{u}_{n+1}^{(k)} - \boldsymbol{u}_n}{\Delta t} + \nabla p_{n+1}^{(k)} = \mathbf{0} & \text{in} \quad \Omega_f, \\ \nabla \cdot \boldsymbol{u}_{n+1}^{(k)} = 0 & \text{in} \quad \Omega_f, \\ \alpha_f \boldsymbol{u}_{n+1}^{(k)} \cdot \boldsymbol{n} - p_{n+1}^{(k)} = \alpha_f \dfrac{\boldsymbol{d}_{n+1}^{(k-1)} - \boldsymbol{d}_n}{\Delta t} \cdot \boldsymbol{n} + \lambda \nabla \boldsymbol{d}_{n+1}^{(k-1)} \boldsymbol{n} & \text{on} \quad \Sigma, \\ +\mathit{Initial\ Conditions}. \end{cases} \tag{4.5}$$

***Structure Problem***:

$$\begin{cases} \rho_s \dfrac{\boldsymbol{d}_{n+1}^{(k)} - 2\boldsymbol{d}_n + \boldsymbol{d}_{n-1}}{\Delta t^2} - \lambda \Delta \boldsymbol{d}_{n+1}^{(k)} = 0 & \text{in} \quad \Omega_s, \\ \lambda \nabla \boldsymbol{d}_{n+1}^{(k)} \boldsymbol{n} = -p_{n+1}^{(k)} & \text{on} \quad \Sigma, \\ \boldsymbol{d}_{n+1}^{(k)} \times \boldsymbol{n} = \boldsymbol{0} & \text{on} \quad \Sigma, \\ \gamma_{ST} \boldsymbol{d}_{n+1}^{(k)} + \lambda \nabla \boldsymbol{d}_{n+1}^{(k)} \boldsymbol{n} = \boldsymbol{0} & \text{on} \quad \Sigma_{out}, \\ + \textit{Initial Conditions}. \end{cases} \tag{4.6}$$

After having defined the *Spherical Simplified Model* (4.4) and the corrispondent Robin-Neumann Scheme (4.5)-(4.6), we can review the necessary steps to find a range for $\alpha_f$:

1. carry on a convergence analysis via the Fourier transforms to obtain an expression of the reduction factor $\rho$ in terms of the modified Bessel functions;
2. minimize such reduction factor $\rho$ considering $\alpha_f = constant$, to obtain a range of theoretical optimal Robin interface parameters: $[\alpha_{fTopt,min}, \alpha_{fTopt,max}]$;

For all the details of the above described theoretical analysis we refer the reader to [49–52].

Now the idea is to apply such theoretical analysis to our *Guccione setting* to find a suitable range for $\alpha_f$ to be used in our *Scheme 2* and *Scheme 4*, but most importantly in our new *Loosely-Coupled EFSI Scheme*. It is clear that our Electro Fluid Structure Interaction problem with the *Guccione setting* is really more complicated and different than the just presented *Spherical Simplified Model* (4.4). Indeed, we do not know the values of $\lambda$ and $\gamma_{ST}$ (present in (4.4)) to be used in the theoretical analysis.

Therefore, the idea to find such necessary parameters $\lambda$ and $\gamma_{ST}$ for the theoretical analysis is to simplify our model in some aspects to obtain a scenario closer to the *Spherical Simplified Model*. The chosen way to simplify our model is a linearization, obtaining the *Hooke setting*. Finally, we can resume this idea as follows:

1. empirically linearize the *Guccione setting* calibrating manually the parameters for the *Hooke setting* to obtain the parameters necessary to carry on the theoretical analysis (i.e. $\lambda$ and $\gamma_{ST}$);
2. compute the theoretical optimal range $[\alpha_{fTopt,min}, \alpha_{fTopt,max}]$ for the Robin interface parameter using the theoretical analysis of the *Spherical Simplified Model* with the just obtained $\lambda$ and $\gamma_{ST}$;
3. test different values of $\alpha_f$ in our EFSI problem with the *Hooke setting* using *S2, S3, S4*; with the main objective to obtain accuracy and stability with our new *Loosely-Coupled EFSI Scheme*;

4. finally test different values of $\alpha_f$ in our EFSI problem with the *Guccione setting* using *S2, S3, S4*; with the main objective to obtain accuracy and stability with our new *Loosely-Coupled EFSI Scheme*;.

In the next subsections all the details of steps 1-2 will be presented, whilst steps 3-4 will be discussed in the next chapter.

### 4.4.2. From the *Guccione setting* to the *Hooke setting*

To simplify the *Guccione setting* and provide suitable values of $\lambda$ and $\gamma_{ST}$ to be used in the *Spherical Simplified Model* (4.4) for the theoretical analysis, we will consider two aspects:

1. Linearization of the structure: we have a non-linear, anisotropic structure modelled via the Guccione model. The idea to have a situation more similar to the *Spherical Simplified Model* (4.4) is to consider a linear, homogeneous and isotropic model for the structure, i.e. the Hooke model: $\sigma_s(\boldsymbol{d}) = \lambda_1(\nabla \boldsymbol{d} + (\nabla \boldsymbol{d})^T) + \lambda_2(\nabla \cdot \boldsymbol{d})I$, where $\sigma_s$ is the Cauchy Stress Tensor related to the first Piola Kirchhoff through $\sigma_s = J^{-1}P_s(\boldsymbol{d})F^T$ and $\lambda_1$ and $\lambda_2$ are linked to the Young modulus $E$ and to the Poisson modulus $\nu$ through the following relations:

$$\lambda_1 = \frac{E}{2(1+\nu)}, \qquad \lambda_2 = \frac{\nu E}{(1+\nu)(1-2\nu)}. \tag{4.7}$$

   From this kind of simplification we can obtain the value $\lambda$ that summarizes in a unique parameter the elastic properties of the structure. We will use this parameter as the $\lambda$ defined in the *Spherical Simplified Model* (4.4) to carry on the theoretical anlaysis. We will compute this value through the Timoshenko correction factor [44, 52]:

$$\lambda = G\lambda_1 = \frac{\pi}{12}\lambda_1. \tag{4.8}$$

2. Simplifications of the pericardium boundary conditions: the boundary conditions used in the *Guccione setting* are visco-elastic with 4 parameters, see (2.5). In the *Spherical Simplified Model* (4.4) only one parameter $\gamma_{ST}$ to surrogate the surrounding tissue is present; therefore, the idea is to use similar boundary conditions, i.e.

eliminate the viscous component: $C_\perp = 0, C_\parallel = 0$ and use:

$$\gamma_{ST} = K_\perp = K_\parallel. \tag{4.9}$$

### 4.4.3. Calibration of the *Hooke setting*

We have chosen to perform the transition from the *Guccione setting* to the *Hooke setting* calibrating manually the necessary parameters using *Scheme 1*. The objective of such calibration is to obtain a behavior of *H-1* similar to the one obtained with *G-1* in terms of the physiological indicators (i)-(vii), but still keeping in mind the physiological behavior requirements I-V. The parameters that we need to calibrate are the following:

- monodomain conductivities: $\Sigma_m^l$, $\Sigma_m^t$, $\Sigma_m^n$;
- pericardium boundary condition $\gamma_{ST} = K_\perp = K_\parallel$;
- maximum tension $\xi$;
- resistance $R$ for the resistance boundary condition;
- Young modulus $E$ and Poisson modulus $\nu$.

This calibration was more difficult than the *Guccione setting* one; indeed, the big simplifications adopted for the structure create difficulties in tuning the parameters. Moreover not many studies were carried on modeling the cardiac tissue with a linear law (due to the inherently non-linear nature of the myocardium) and even guess values for the Young modulus were difficult to find. However, some indications were present in literature [48]. On the other hand we have chosen a priori the value of the the Poisson modulus $\nu = 0.45$, that means a body near to incompressibility (exact incompressibility is attained in the limit of $\nu \to 0.5$). For what concerns the use of only one parameter for the pericardium boundary condition, some guesses can be found in [77, 96]. We have simulated $0.5s$ with $\Delta t = 2 \cdot 10^{-4} s$.

We report the calibrated parameters for the *Hooke setting* in table 4.3 and the values of the physiological indicators (i)-(vii) obtained with such calibrated parameters using *Scheme 1* (i.e. *H-1*) in table 4.4.

| | Calibrated value |
|---|---|
| $\Sigma_m^l$ $[m^2/s]$ | $1.68 \cdot 10^{-4}$ |
| $\Sigma_m^t$ $[m^2/s]$ | $7.69 \cdot 10^{-5}$ |
| $\Sigma_m^n$ $[m^2/s]$ | $2.48 \cdot 10^{-5}$ |
| $\gamma_{ST} = K_\perp = K_\parallel [\frac{Pa}{m}]$ | $10^4$ |
| $C_\perp [\frac{Pa \cdot s}{m}]$ | 0 |
| $C_\parallel [\frac{Pa \cdot s}{m}]$ | 0 |
| $\xi$ $[Pa]$ | $1.3 \cdot 10^6$ |
| $R$ $[\frac{Kg}{m^4 \cdot s}]$ | $1 \cdot 10^7$ |
| **Young modulus E** $[Pa]$ | $5 \cdot 10^4$ |
| **Poisson modulus** $\nu$ | 0.45 |

Table 4.3: Calibrated parameters for the *Hooke setting*.

| | **H-1** |
|---|---|
| $p_{max}$ $[mmHg]$ | 126.02 |
| $E_f$ | 51.1% |
| $Time_{act}$ $[ms]$ | 97 |
| $max\|\|\boldsymbol{u}\|\|$ $[m/s]$ | 1.9 |
| $ILI_C$ | 0.01% |
| $ILI_R$ | 0.01% |
| $T_{O,A}$ $[s]$ | 0.082 |
| $T_{C,A}$ $[s]$ | 0.184 |
| $T_{O,M}$ $[s]$ | 0.244 |
| $CPU_{fTime}$ $[s]$ | 3380 |

Table 4.4: Values of the physiological indicators (i)-(vii) obtained with *H-1* to assess the fulfillment of the requirements I-V. We have simulated $0.5s$.

We can observe from table 4.4 that again all the requirements I-V have been satisfied and the physiological indicators (i)-(vii) are similar to the one obtained in table 4.2; in particular:

1. the maximum pressure, i.e. $p_{max} = 126.02 mmHg$, is slightly little bit higher than the one obtained with *G-1* but again falls in the range defined in requirement I;
2. the ejection fraction, i.e. $E_f = 51.1\%$, is a slightly lower than in *G-1* but it is again above our threshold defined in requirement II;
3. the electrical activation $Time_{act} = 97ms$; we have used the same electrical conductivities as in the *Guccione setting* because $97ms$ is however an acceptable value for the activation compared to $90ms$ of requirement III;
4. the peak blood velocity magnitude, i.e. $max||\boldsymbol{u}|| = 1.9m/s$, is less than the threshold defined in the requirement IV, but higher than the one obtained with *G-1*. This can be related to the fact that with *H-1* we have used a higher maximum tension $\xi$ with respect to *G-1* to obtain value for the ejection fraction that satisfies requirement II;
5. finally the physiological variations among the 4 cardiac phases are well described by *H-1*; indeed, we have reported the opening/closing time of the valves. Moreover the 2 isovolumic phases are perfectly captured as one can see from the Isovolumic Loss Indicators, both equal to 0.01%. A further confirmation of this fact can be visualized in figure 4.8a, where the time evolution of the ventricular chamber volume is presented. Therefore, also requirement V has been satisfied.

We can now compare the time evolution of the ventricular chamber volume and pressure obtained in *G-1* and *H-1*, such comparison can be found in figure 4.8.

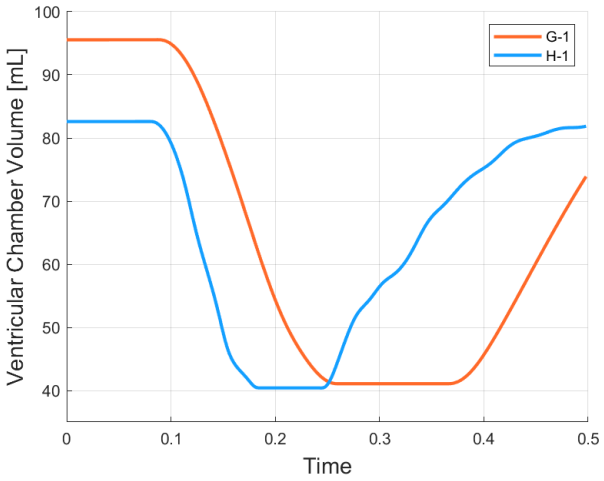


(a) Ventricular chamber volume of *G-1* and *H-1*.

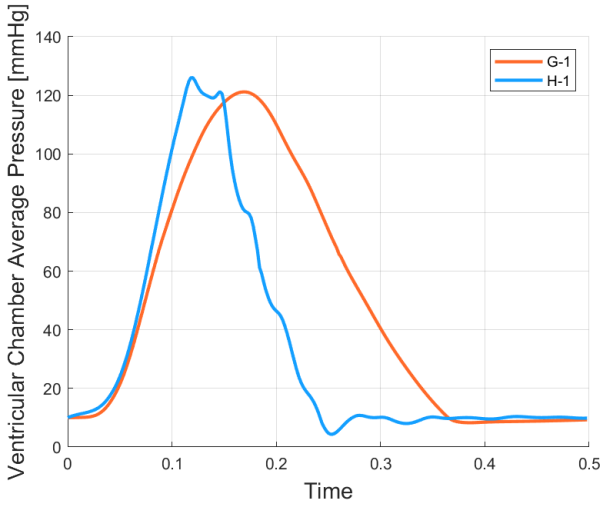


(b) Ventricular chamber average pressure of *G-1* and *H-1*.

Figure 4.8: Comparison of the time evolution of the ventricular chamber volume and pressure in *G-1* and *H-1*.

We notice that the two behaviors are qualitatively similar, however the following differences have to be highlighted:

- all the 4 cardiac phases are anticipated in *H-1* with respect to *G-1*; this can be seen also from the opening/closing times of the valves in table 4.4 and table 4.2;
- *H-1* has some oscillations in the time evolution of both ventricular chamber volume and pressure; this can be related to the simplified boundary condition prescribed for the pericardium. Indeed, they lack viscosity as described in section 4.4.2;
- the ventricular chamber volumes are different at the beginning of the simulation; this can be related again to the different boundary conditions for the pericardium, but also to the different linear (Hooke) and non-linear (Guccione) laws for the structure. However they arrive at the same minimum ventricular chamber value at the end of the ejection phase.

Comparing the Guccione calibrated value in table 4.1 to the Hooke calibrated value in table 4.3, we can finally notice that the resistances $R$ are very similar and the parameter $\gamma_{ST}$ miming the pericardium is exactly equal to the value $K_\perp$ used in the *Guccione setting*.

### 4.4.4. Computation of the theoretical range for the Robin interface parameter $\alpha_f$

After having calibrated all the parameters for the Hooke case, we obtained all the useful informations to compute the theoretical optimal range $[\alpha_{fTopt,min}, \alpha_{fTopt,max}]$ for the *Spherical Simplified Model*. Indeed, from the Young modulus $E$ and the Poisson modulus $\nu$ (see table 4.4) we have computed:

$$\lambda_1 = \frac{E}{2(1+\nu)} = 1.72 \cdot 10^4 Pa. \tag{4.10}$$

Therefore, we have computed the parameter $\lambda$, summarizing the elastic properties of the structure, via the Timoshenko correction factor:

$$\lambda = G\lambda_1 = \frac{\pi}{12}\lambda_1 = 4.51 \cdot 10^3 Pa. \tag{4.11}$$

Finally we had all the desired parameters needed to carry on the theoretical analysis on the *Spherical Simplified Model* to compute the range $[\alpha_{fTopt,min}, \alpha_{fTopt,max}]$, they are presented in table 4.5.

| | **Value** |
|---|---|
| $\Delta t$ $[s]$ | $2 \cdot 10^{-4}$ |
| **Small semiaxis** $b$ $[cm]$ | 2.5 |
| **Big semiaxis** $a$ $[cm]$ | 6 |
| **Structure thickness** $[cm]$ | 0.8 |
| $\gamma_{ST}[\frac{Pa}{m}]$ | $10^4$ |
| $\lambda$ $[Pa]$ | $4.51 \cdot 10^3$ |
| **Fluid density** $\rho_f$ $[\frac{Kg}{m^3}]$ | $1.06 \cdot 10^3$ |
| **Structure density** $\rho_s$ $[\frac{Kg}{m^3}]$ | $1 \cdot 10^3$ |

Table 4.5: Parameters needed to compute the theoretical optimal range for $\alpha_f$ in the *Simplified Spherical Model*.

For what concerns the geometrical differences between our computational domain (i.e. the

truncated ellipsoid, see section 4.1.1) and the one considered in the *Spherical Simplified Model* (4.4) (i.e. a sphere); we will do an approximation considering the radius $r$ of the sphere (as in [52]) equal to an average of the two semiaxes of our prolate: $r = \dfrac{a+b}{2}$.

The theoretical analysis of the *Spherical Simplified Problem* and the computation of the theoretical optimal range, given the parameters that we have calibrated in table 4.5, was performed by one of our collaborators, professor Giacomo Gigante. Therefore, the the interval for the theoretical optimal Robin interface parameter for the *Spherical Simplified Model* using the quantities $\lambda$ and $\gamma_{ST}$ obtained through the linearization of the *Guccione setting* with the *Hooke setting* is:

$$[\alpha_{fTopt,min}, \alpha_{fTopt,max}] = [1906.4, 2415.1][\frac{kg}{m^2 \cdot s}]. \tag{4.12}$$

For the numerical results of chapter 5, as representative of the theoretical optimal range (4.12), we will consider $\alpha_f = 2225\frac{kg}{m^2 \cdot s}$, and we will refer to it as $\alpha_{fTopt} = 2225\frac{kg}{m^2 \cdot s}$ or theoretical optimal value. Now we want to use this range (that is optimal for the *Spherical Simplified Model*) as an initial guess to explore the efficiency of *Scheme 2, 3* and *4* in both the *Hooke setting* and the *Guccione setting*. However, the most important objective of our work is to obtain good results of stability, accuracy and computational costs using our new *Loosely-coupled EFSI Scheme* to simulate the cardiac Electro Fluid Structure Interaction Problem (2.15) in the *Guccione setting*.

## 4.5. Summary and roadmap

Finally we can summar what we have done in this chapter and define the road map for the next chapter:

- We have performed:
  - manual calibration of the *Guccione setting* using *Scheme 1*;
  - linearization of the *Guccione setting* through a manual calibration of the *Hooke setting* to obtain the necessary parameters ($\lambda$ and $\gamma_{ST}$) to carry on the theoretical analysis on the *Spherical Simplified Model*;
  - computation of a theoretical optimal range $[\alpha_{fTopt,min}, \alpha_{fTopt,max}]$ for $\alpha_f$ through the theoretical analysis of the *Spherical Simplified Model* using the parameters $\lambda$ and $\gamma_{ST}$ obtained above. It is important to remark that the theoretical analysis is expected to provide a range of values that are not the effective optimal ones for the EFSI Problem due to the strong simplification of model and geometry of the *Spherical Simplified Model*. However it is important to have an initial guess sufficiently close to the effective range. In this sense the theoretical analysis is useful.
- In chapter 5 we will:
  - analyze *H-2* using different values for $\alpha_f$ and compare the results with *H-1* in terms of accuracy, stability and computational cost; then perform a manual calibration of the practical optimal $\alpha_{fPopt,H2}$ for *H-2*;
  - analyze *H-3* using different values for $\alpha_f$ and compare the results with *H-1* in terms of accuracy, stability and computational cost; then perform a manual calibration of the practical optimal $\alpha_{fPopt,H3}$ for *H-3*.
  - analyze *H-4* using different values for $\alpha_f$; then compare the results with *H-1*, *H-2* and *H-3* in terms of accuracy, stability and computational costs;
  - analyze the case *H-3* halving the time step to assess the impact of the time discretization;
  - analyze *G-2* using different values for $\alpha_f$ and compare the results with *H-1* in terms of accuracy, stability and computational cost; then perform a manual calibration of the practical optimal $\alpha_{fPopt,G2}$ for *G-2*;
  - analyze *G-3* using different values for $\alpha_f$ and compare the results with *H-1* in

terms of accuracy, stability and computational cost; then perform a manual calibration of the practical optimal $\alpha_{fPopt,G3}$ for *G-3*;

– analyze *G-4* using different values for $\alpha_f$; then compare the results with *G-1*, *G-2* and *G-3* in terms of accuracy, stability and computational costs;

# 5 | Numerical Results

In what follows, the unit $[\frac{kg}{m^2 \cdot s}]$ for the parameter $\alpha_f$ will be understood. This abuse of notation is done for the sake of simplicity in notation, tables and figures.

Moreover, we will often make use and refer to the notation, indicators and requirements defined in Section 4.2

## 5.1. EFSI Schemes with Partitioned FSI Robin-Neumann treatment in the *Hooke setting*

### 5.1.1. *Staggered E-Partitioned FSI Scheme 2*

In this section we study the efficiency of *Scheme 2* (see algorithm 3.2) to solve the cardiac EFSI problem with the *Hooke setting* (see Section 4.4.3). Besides the theoretical value $\alpha_{fTopt}$ representing the range (4.12) computed through the theoretical analysis of the *Spherical Simplified Model* (4.4), other values in the neighbouring have been considered to better explore the efficiency of the scheme in terms of computational cost and average number of iterations per time step of the Robin-Neumann FSI loop. To compare the different choices of $\alpha_f$ $0.1s$ have been simulated using $\Delta t = 2 \cdot 10^{-4} s$.

The use of *S2* in the *Hooke setting* gives, as one could expect due to the implicit treatment of FSI, the same results obtained in *H-1*. Indeed, the solution obtained with *H-2* for every value of the Robin parameter $10 \leq \alpha_f \leq 10^6$ is at convergence exactly identical to the one obtained with *H-1*, featuring the same values of ventricular chamber average pressure, ventricular chamber volume and myocardium volume at each time step. However the different values of $\alpha_f$ give different behaviors of *Scheme 2* in terms of computational cost and average number of iterations of the Robin-Neumann FSI loop, this comparison can be visualized in figure 5.1 and table 5.1.

For values $\alpha_f > 10^6$ *H-2* does not reach convergence because when the Robin interface value becomes large, say $\alpha_f \to +\infty$, our Robin-Neumann scheme for FSI behaves like a Dirichlet-Neumann scheme, due to the fact that in the linear combination of the Robin

Interface condition (3.8) we have a very large value of $\alpha_f$ that makes such condition almost identical to a Dirichlet one. This leads to significant numerical problems inherited from the continuous problem; indeed, given our choice of boundary conditions, in particular during isovolumic phases, the Dirichlet-Neumann splitting hinders the well posedness of the fluid problem, leading to an unsolvable numerical problem. Indeed, the fluid substep should be performed only with Dirichlet conditions on all the boundary, and the compatibility conditions are not satisfied, in general.

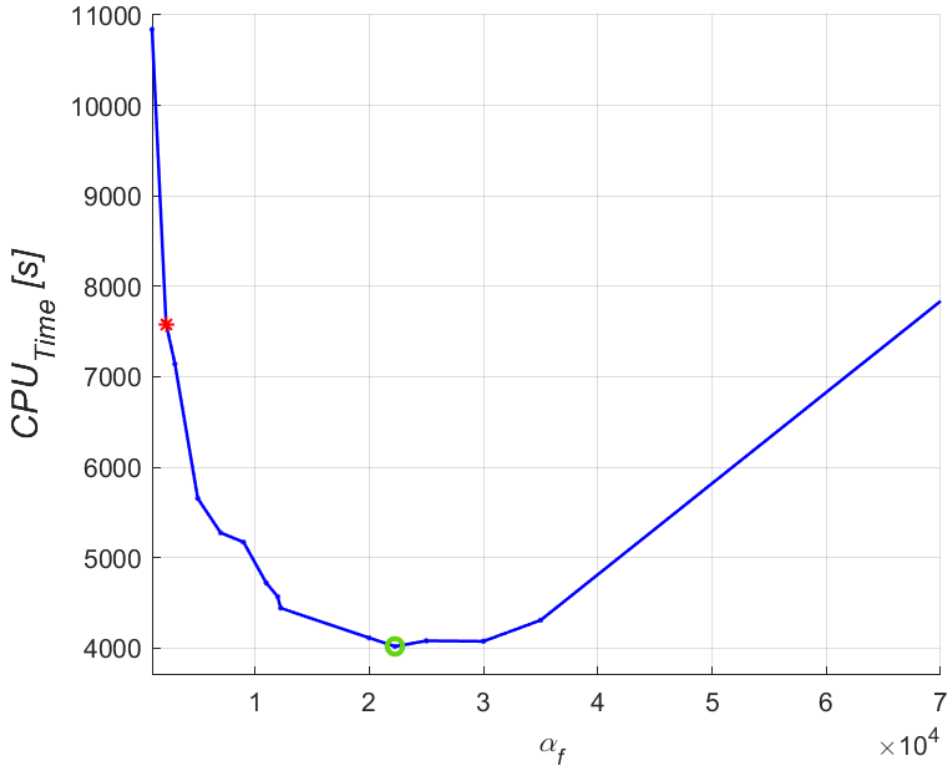


Figure 5.1: Comparison of the $CPU_{Time}$ performances to simulate $0.1s$ of the cardiac EFSI problem in the *Hooke setting* using *S2* with different values of $\alpha_f$. The theoretical value obtained with the theoretical analysis is highlighted in red: $\alpha_{fTopt} = 2225$. On the other hand the practical optimal value is highlighted in green, i.e. $\alpha_{fPopt,H2} = 22250$.

| $\alpha_f[\frac{kg}{m^2 \cdot s^2}]$ | 1000 | 2225 | 5000 | 11000 | 12500 | 22250 | 35000 | $10^5$ |
|---|---|---|---|---|---|---|---|---|
| **Avg #** | 27.25 | 18.5 | 13.3 | 10.85 | 10.3 | 9.15 | 9.75 | 15.2 |

Table 5.1: Comparison of the average number of iterations at each time step in the FSI Robin-Neumann loop of *H-2* with different values of $\alpha_f$. The representative of the range obtained with the theoretical analysis is highlighted in red: $\alpha_{fTopt} = 2225$. On the other hand the practical optimal value is highlighted in green, i.e. $\alpha_{fPopt,H2} = 22250$.

One can immediately observe from figure 5.1 that the theoretical value $\alpha_{fTopt} = 2225$ (4.12) (highlighted with red asterisk) is not the practical optimal one. This could be expected due to the strong simplifications of model and geometry in the theoretical analysis. However, it is important to have an initial guess sufficiently close to the effective range. In this sense the theoretical analysis is useful. On the other hand the practical optimal $\alpha_f$ for *H-2* is the value $\alpha_{fPopt,H2} = 22250$, highlighted with a green circle in the figure. This value is optimal from the point of view of computational cost, having the same solution for all the $\alpha_f$.

Notice from figure 5.1 that the simulation of $0.1s$ of *H-2* with $\alpha_{fPopt,H2}$ lasts $\sim 4000s$ against the $3380s$ to simulate $0.5s$ of *H-1* (see table 4.4), this shows that *Scheme 1* is way faster than *Scheme 2* even if they give exactly the same results. Moreover, the comparison between the average number of iterations per time step in the Robin-Neumann FSI loop (see table 5.1) shows that with the practical optimal value $\alpha_{fPopt,H2} = 22250$ the average number of iterations is halved (9.15) with respect to the theoretical optimal one $\alpha_{fTopt} = 2225$ (18.5). This discrepancy is again due to the many differences between our EFSI Problem and the *Spherical Simplified Problem* where the theoretical analysis was carried on.

### 5.1.2. *Loosely Coupled EFSI Scheme 3*

In this section we have used the new *Loosely Coupled EFSI Scheme* (or *Scheme 3*, see algorithm 3.3) to run simulations of the cardiac EFSI Problem in the *Hooke setting*. Different values of $\alpha_f$ have been tried, including the practical optimal one calibrated for *H-2* (i.e. $\alpha_{fPopt,H2} = 22250$) and the theoretical optimal one $\alpha_{fTopt} = 2225$, representing the range (4.12) computed in Section 4.4.4. The simulation of the *Hooke setting* using *S3* reaches convergence only for values of the Robin interface parameter such that $10 < \alpha_f \leq 12250$. However, not all the Robin interface parameters perform well. Indeed, with values $\alpha_f \leq 1000$ the simulation does not describe the physiological variations among the

4 cardiac phases, e.g. with $\alpha_f = 100$ there is not an opening of the aortic valve.

The results of the simulations *H-3* with different values of $\alpha_f$ have been compared to the one of *H-1* in terms of accuracy, stability and computational cost. We summarize such comparison in terms of the time evolution of ventricular chamber volume and pressure in figure 5.2 and in terms of the obtained physiological indicators in table 5.2.

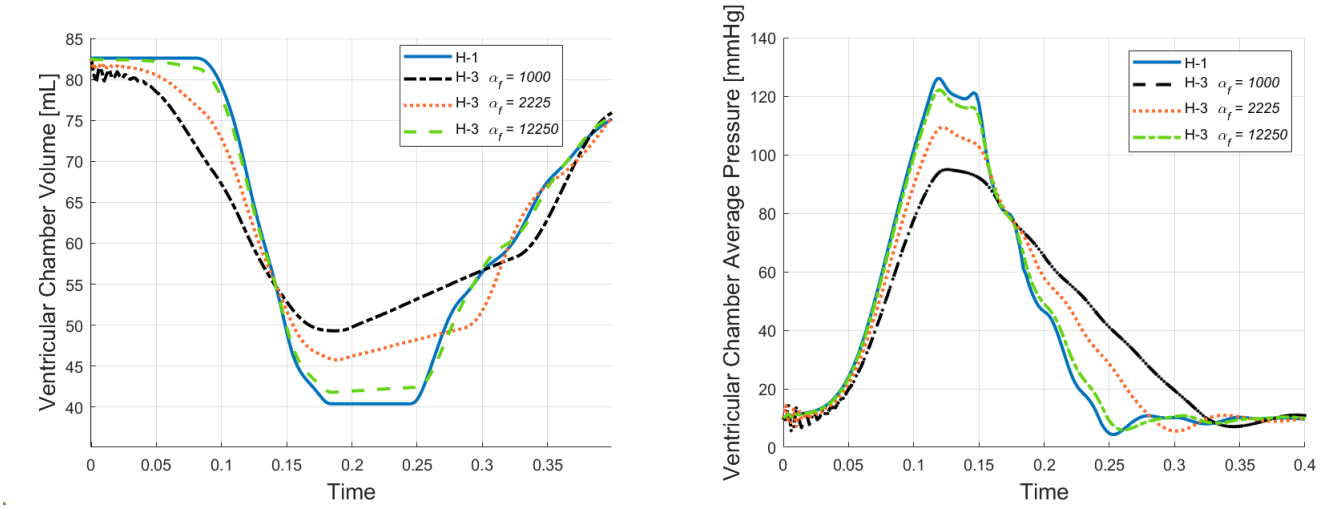


(a) Ventricular chamber volume.

(b) Ventricular chamber average pressure.

Figure 5.2: Time evolution of the ventricular chamber volume and pressure using *S1* and *S3* with different values of $\alpha_f$ to simulate the *Hooke setting* for $0.5s$

| | *H-1* | *H-3* $\alpha_f = 1000$ | *H-3* $\alpha_f = \alpha_{fTopt} = 2225$ | *H-3* $\alpha_f = 12250$ |
|---|---|---|---|---|
| $p_{max}$ $[mmHg]$ | 126.02 | 94.4 | 109.35 | 122.21 |
| $E_f$ | 51.1% | 40.3% | 44.6% | 49.38% |
| $Time_{act}$ $[ms]$ | 97 | 97 | 97 | 97 |
| $max\|\|\boldsymbol{u}\|\|$ $[m/s]$ | 1.9 | 0.91 | 1.4 | 1.8 |
| $ILI_C$ | 0.01% | 16.34% | 7.97% | 1.44% |
| $ILI_R$ | 0.01% | 14.56% | 7.15% | 1.44% |
| $T_{O,A}$ $[s]$ | 0.082 | 0.094 | 0.088 | 0.082 |
| $T_{C,A}$ $[s]$ | 0.184 | 0.2 | 0.194 | 0.186 |
| $T_{O,M}$ $[s]$ | 0.244 | 0.326 | 0.284 | 0.25 |
| $CPU_{Time}$ $[s]$ | 3380 | 3845 | 3506 | 3383 |

Table 5.2: Comparison of physiological indicators (i)-(vii) and $CPU_{Time}$ obtained in *H-1* with the ones obtained in *H-3* with different values of $\alpha_f$.

We can observe the following things:

- from figure 5.2a we can observe that in general using *Scheme 3* we lose some volume during the first isovolumic phase and we gain volume during the second one, in what follows we will refer to this issue as isovolumic loss. This behavior is described by the physiological indicators (v)-(vi) and it is linked to the fact that we are using an explicit scheme for the FSI problem, so some spurious numerical fluxes are present. Indeed, there is not an exact match of the imposed FSI coupling conditions due to the explicit treatment, therefore the velocity of the fluid differs from the time derivative of the structure displacement on the interface $\Sigma$ leading to such spurious numerical fluxes through the Fluid Structure Interface. We can observe also looking at the Isovolumic Loss Indicators in table 5.2 that the smaller the Robin parameter $\alpha_f$, the higher the isovolumic loss during isovolumic phases. The just cited negative correlation explains also the positive correlation between the maximum pressure $p_{max}$ and $\alpha_f$; indeed, the smaller is $\alpha_f$, the less the simulation captures the isovolumic phases. Therefore, being the first isovolumic phase responsible of the increase of pressure, when we do not reproduce it well, we obtain a lower maximum pressure.

- For what concerns the range computed in Section 4.4.4 for the theoretical optimal values of the *Spherical Simplified Model*, i.e. $[\alpha_{fTopt,min}, \alpha_{fTopt,max}] = [1906.4, 2415.1]$, it is contained in the range of converging and stable simulations depicted above ($1000 < \alpha_f \leq 12250$). Indeed, besides some initial oscillations possibly due to the simplified boundary conditions prescribed on the pericardium (see Section 4.4.2), the physiological variations among the 4 cardiac phases are quite well described by the theoretical optimal value representing range (4.12) (i.e. $\alpha_{fTopt} = 2225$) as one can observe from figure 5.2a. However, we can see from table 5.2 that using $\alpha_{fTopt} = 2225$ we commit an error of $\sim 7/8\%$ in capturing the isovolumic phases, together with an error of $\sim 10\%$ in fulfilling the other physiological requirements I-IV.

- Looking at both figure 5.2 and table 5.2 we can observe that the use of *S3* with $\alpha_f = 12250$ gives the best physiological indicators; indeed, it almost perfectly captures the isovolumic phases with an error of only 1.44% and all the other physiological indicators (i)-(iv) are in line with the requirements I-IV with an error of $\sim 2\%$. Therefore, we can say that the practical optimal value of the Robin interface parameter for *H-3* is $\alpha_{fPopt,H3} = 12250$.

- For what concerns the $CPU_{Time}$ we have almost the same behavior for all the values $\alpha_f$ reported in table 5.2. The similar computational costs of *H-1* and *H-3* in all

cases is related to the fact that the only difference between the two schemes used is that: with *Scheme 1* we solve a large FSI linear system at each time step, while with *Scheme 3* we solve two smaller Fluid and Structure linear systems at each time step. Therefore, being the assembling of the fluid system one of the most significant contribution to the computational cost, here in both cases we assemble such system only once per time step.

- Unfortunately the practical optimal Robin interface parameter calibrated for *H-2* (i.e. $\alpha_{fPopt,H2} = 22250$) does not give a converging simulation using *S3*, but until it crashes it gives the best results in capturing the first isovolumic phase.

### 5.1.3. *Scheme 4*

An idea to improve the goodness of the results obtained with *Scheme 3* is to perform 2 iterations instead of 1 in the FSI Robin-Neumann Problem; this was done using *Scheme 4*, that is equal to *S2* but with $K_{max} = 2$ in the FSI Robin-Neumann loop. We have used such scheme with the theoretical optimal $\alpha_{fTopt} = 2225$ and the practical optimal $\alpha_{fPopt,H3} = 12250$ calibrated for *H-3*. Unfortunately *H-4* with $\alpha_f = 12250$ does not reach convergence, so we have decided to use a value slightly detached from the maximum allowed, i.e. $\alpha_f = 11000$. Therefore, in table 5.3, we present a comparison in terms of the physiological indicators (i)-(vii) and computational costs obtained in *H-1*, *H-3* and *H-4* for $\alpha_f = \alpha_{fTopt} = 2225$; the same comparison can be found in table 5.4 for $\alpha_f = 11000$. Moreover, in figure 5.3 and figure 5.4 one can find also a comparison in terms of the time evolution of the ventricular chamber volume and pressure.

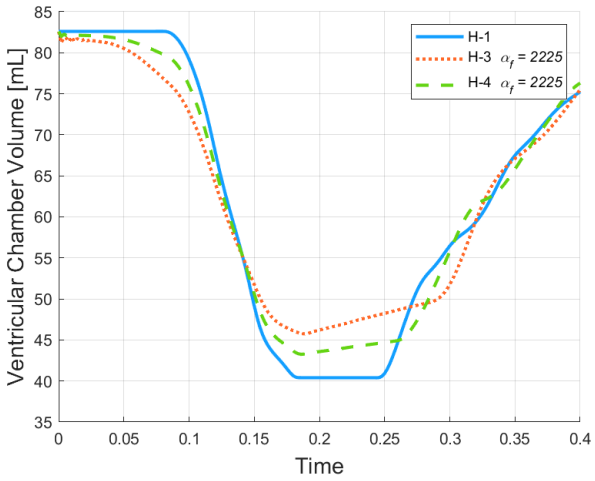


(a) Ventricular chamber volume.

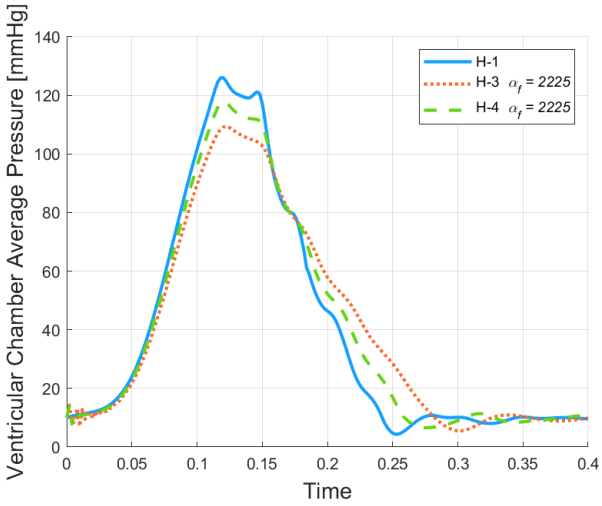


(b) Ventricular chamber average pressure.

Figure 5.3: Time evolution of the ventricular chamber volume and pressure in *H-1*, *H-3* and *H-4* with $\alpha_f = \alpha_{fTopt} = 2225$.

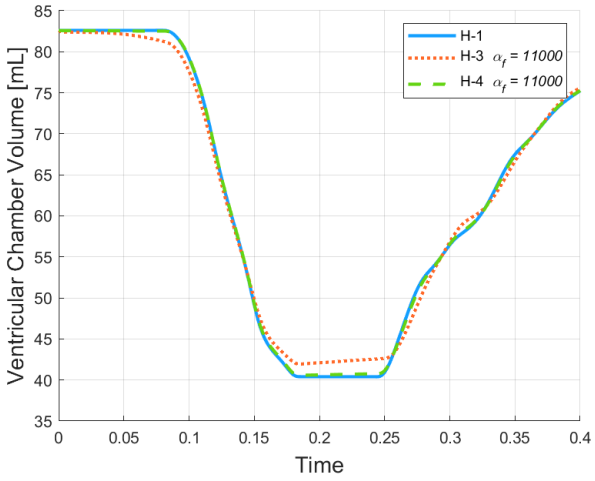


(a) Ventricular chamber volume.

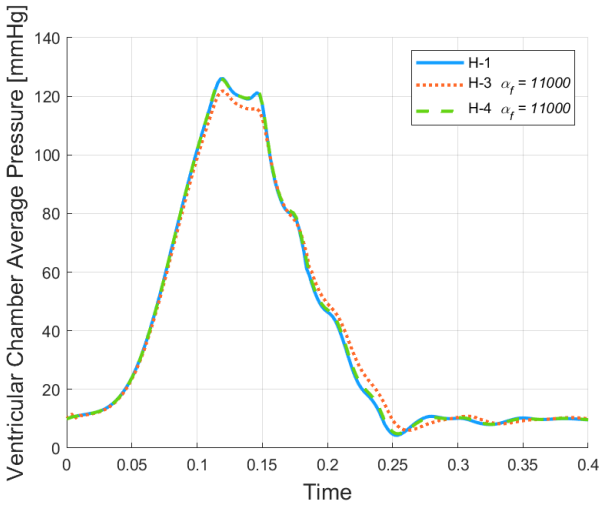


(b) Ventricular chamber average pressure.

Figure 5.4: time evolution of the ventricular chamber volume and pressure in *H-1*, *H-3* and *H-4* with $\alpha_f = 11000$.

| | *H-1* | *H-3* $\alpha_f = \alpha_{fTopt} = 2225$ | *H-4* $\alpha_f = \alpha_{fTopt} = 2225$ |
|---|---|---|---|
| $p_{max}$ $[mmHg]$ | 126.02 | 109.35 | 117.78 |
| $E_f$ | 51.1% | 44.6% | 47.64% |
| $Time_{act}$ $[ms]$ | 97 | 97 | 97 |
| $max\|\|\boldsymbol{u}\|\|$ $[m/s]$ | 1.9 | 1.4 | 1.6 |
| $ILI_C$ | 0.01% | 7.97% | 3.75% |
| $ILI_R$ | 0.01% | 7.15% | 3.39% |
| $T_{O,A}$ $[s]$ | 0.082 | 0.088 | 0.084 |
| $T_{C,A}$ $[s]$ | 0.184 | 0.194 | 0.19 |
| $T_{O,M}$ $[s]$ | 0.244 | 0.284 | 0.26 |
| $CPU_{Time}$ $[s]$ | 3380 | 3506 | 5648 |

Table 5.3: Comparison of physiological indicators (i)-(vii) and computational costs obtained in *H-1*, *H-3* and *H-4* with the theoretical optimal value $\alpha_{fTopt} = 2225$.

| | *H-1* | *H-3* $\alpha_f = 11000$ | *H-4* $\alpha_f = 11000$ |
|---|---|---|---|
| $p_{max}$ $[mmHg]$ | 126.02 | 121.85 | 125.84 |
| $E_f$ | 51.1% | 49.24% | 50.88% |
| $Time_{act}$ $[ms]$ | 97 | 97 | 97 |
| $max\|\|\boldsymbol{u}\|\|$ $[m/s]$ | 1.9 | 1.8 | 1.9 |
| $ILI_C$ | 0.01% | 1.68% | 0.08% |
| $ILI_R$ | 0.01% | 1.64% | 0.47% |
| $T_{O,A}$ $[s]$ | 0.082 | 0.084 | 0.082 |
| $T_{C,A}$ $[s]$ | 0.184 | 0.186 | 0.186 |
| $T_{O,M}$ $[s]$ | 0.244 | 0.252 | 0.244 |
| $CPU_{Time}$ $[s]$ | 3380 | 3502 | 5653 |

Table 5.4: Comparison of physiological indicators (i)-(vii) and computational costs obtained in *H-1*, *H-3* and *H-4* with $\alpha_f = 11000$.

From figure 5.3a and figure 5.4a it is clear that performing 2 iterations per time step instead of 1 in the FSI loop leads to a significant improvement in capturing the isovolumic phases, that now are better captured in *H-4* with respect to *H-3* with the theoretical optimal $\alpha_{fTopt} = 2225$, and almost perfectly captured in *H-4* with $\alpha_f = 11000$. More-

over, by performing 2 iterations, *Scheme 4* is closer to an implicit scheme, so that the discrepancies with the results of *H-1* are reduced.

Also looking at the physiological indicators reported in table 5.3 and table 5.4 we notice how passing to 2 iterations in the FSI loop leads to significant improvements in all the physiological indicators, in particular notice that the Isovolumic Loss Indicators are more than halved passing from *H-3* to *H-4* with both the considered $\alpha_f$. Moreover using *S4* with $\alpha_f = 11000$ leads to results almost equal to the one obtained in *H-1*. However, the computational cost in *H-4* almost doubles with respect to *H-3*, as we could expect doubling the number of iterations, but it remains however comparable to the one obtained in *H-1*. Anyway *S4* has again the advantage to be modular.

### 5.1.4. Halving the time step

Another possible solution to account for the isovolumic losses obtained with *Scheme 3* is to halve the time step. Indeed, at the continuous mathematical level the Robin-Neumann imposition of the coupling conditions for the Fluid-Structure Interaction does not have the problem of the spurious numerical fluxes, that instead affects the numerical scheme when the coupling conditions are treated explicitly like in the *Loosely Coupled EFSI Scheme*. Therefore for $\Delta t \to 0$ we expect to move towards a better situation where spurious numerical fluxes are reduced during the isovolumic phases.

We have computed again a range for the theoretical optimal values using the theoretical analysis on the *Spherical Simplified problem* due to the fact that such analysis depends also on $\Delta t$, see Section 4.4.4. Since the theoretical computed range was almost the same of the previous case (4.12), we have chosen the same representative for such theoretical optimal range: $\alpha_{fTopt} = 2225$. Again we needed to simulate a new *H-1* but with $\Delta t = 10^{-4}s$, we will refer to the simulation with such $\Delta t$ in the *Hooke setting* using the different schemes as *H-*$j_b$, where $j$ indicates the use of *Scheme j*. We have simulated again $0.5s$.

We present the comparison beteween *H-*$1_b$ and *H-*$3_b$ with different values for $\alpha_f$ in figure 5.5, where the time evolution of ventricular chamber volume and average pressure is reported, and in table 5.5 in terms of the physiological indicators (i)-(vii) and computational costs.

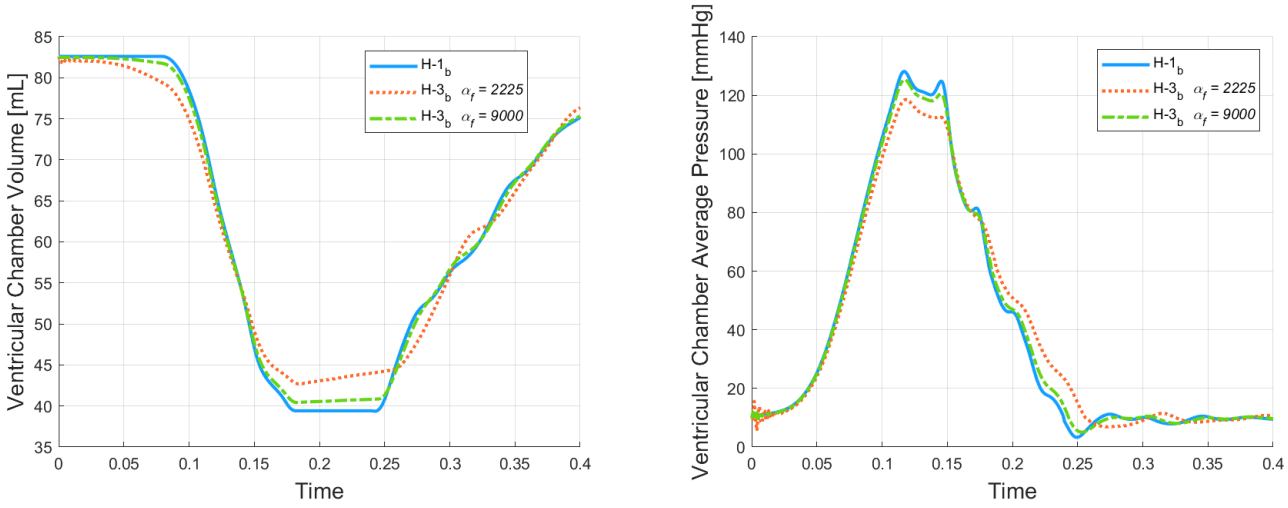


(a) Ventricular chamber volume.

(b) Ventricular chamber average pressure.

Figure 5.5: time evolution of the ventricular chamber volume and pressure in *H-1* and *H-3* with different values of $\alpha_f$.

| | $H\text{-}1_b$ | $H\text{-}3_b$ $\alpha_f = \alpha_{fTopt} = 2225$ | $H\text{-}3_b$ $\alpha_f = 9000$ |
|---|---|---|---|
| $p_{max}$ $[mmHg]$ | 128.17 | 118.5 | 125.35 |
| $E_f$ | 52.34% | 48.33% | 51.05% |
| $Time_{act}$ $[ms]$ | 96 | 96 | 96 |
| $max\|\|\boldsymbol{u}\|\|$ $[m/s]$ | 2 | 1.7 | 1.9 |
| $ILI_C$ | 0.01% | 3.93% | 0.98% |
| $ILI_R$ | 0.01% | 3.74% | 0.98% |
| $T_{O,A}$ $[s]$ | 0.08 | 0.082 | 0.08 |
| $T_{C,A}$ $[s]$ | 0.182 | 0.187 | 0.184 |
| $T_{O,M}$ $[s]$ | 0.24 | 0.257 | 0.245 |
| $CPU_{Time}$ $[s]$ | 6680 | 6427 | 6575 |

Table 5.5: Comparison of physiological indicators (i)-(vii) and $CPU_{Time}$ obtained in $H\text{-}1_b$ against the one obtained with $H\text{-}3_b$ with different values of $\alpha_f$, simulating $0.5s$ with $\Delta t = 10^{-4}s$.

From figure 5.5a we can observe again the negative correlation between the Robin parameter $\alpha_f$ and the loss/gain of volume during the isovolumic phases, even if now it seems that the isovolumic phases are better captured. This is confirmed by the physiological indicators of table 5.5, where we can observe from the Isovolumic Loss Indicators that

halving the time step also the errors capturing the isovolumic phases are halved using the theoretical optimal value; indeed, here with the theoretical optimal value $\alpha_{fTopt} = 2225$ we have an error of $\sim 4\%$, while in the case with $\Delta t = 2 \cdot 10^{-4} s$ we obtained an error of $\sim 7/8\%$, as one can see from table 5.2. Moreover, also all the other physiological indicators better fulfill the requirements I-IV, with an error of $\sim 4/5\%$ with the theoretical optimal $\alpha_{fTopt} = 2225$.

Finally, in this case the practical optimal value for $H\text{-}3_b$ is $\alpha_{fPopt,H3_b} = 9000$, but for all values $\alpha_f > 9000$ the simulation does not converge.

## 5.2. EFSI Schemes with Partitioned FSI Robin-Neumann treatment in the *Guccione setting*

Now, after having extensively analyzed the *Hooke setting* and the performances of different schemes solving the cardiac EFSI Problem in such setting, we finally return to the *Guccione setting* calibrated in Section 4.3. We will again carry out the same analysis performed in the previous section, employing and comparing the different schemes.

### 5.2.1. *Staggered E-Partitioned FSI Scheme 2*

We first explore the use of *Scheme 2*. We have used the theoretical value $\alpha_{fTopt} = 2225$, representative of the theoretical optimal range (4.12) computed for the *Simplified Spherical Model*. We have explored also other values $\alpha_f$ performing a manual calibration of the practical optimal one for *G-2* simulating $0.1s$ with $\Delta t = 2 \cdot 10^{-4} s$. From *G-2* we obtained a complete coincidence with the results obtained with *G-1* (see Section 4.3) $\forall \alpha_f$ such that $10 < \alpha_f \leq 40000$. Here we notice that the maximum allowed value of $\alpha_f$ (i.e. $\alpha_f = 40000$) is smaller than the one obtained with *H-2*, see Section 5.1.1.

The results of *G-2* using different values of $\alpha_f$ in terms of $CPU_{Time}$ and average number of iterations per time step of the FSI Robin-Neumann loop are summarized in figure 5.6 and table 5.6.

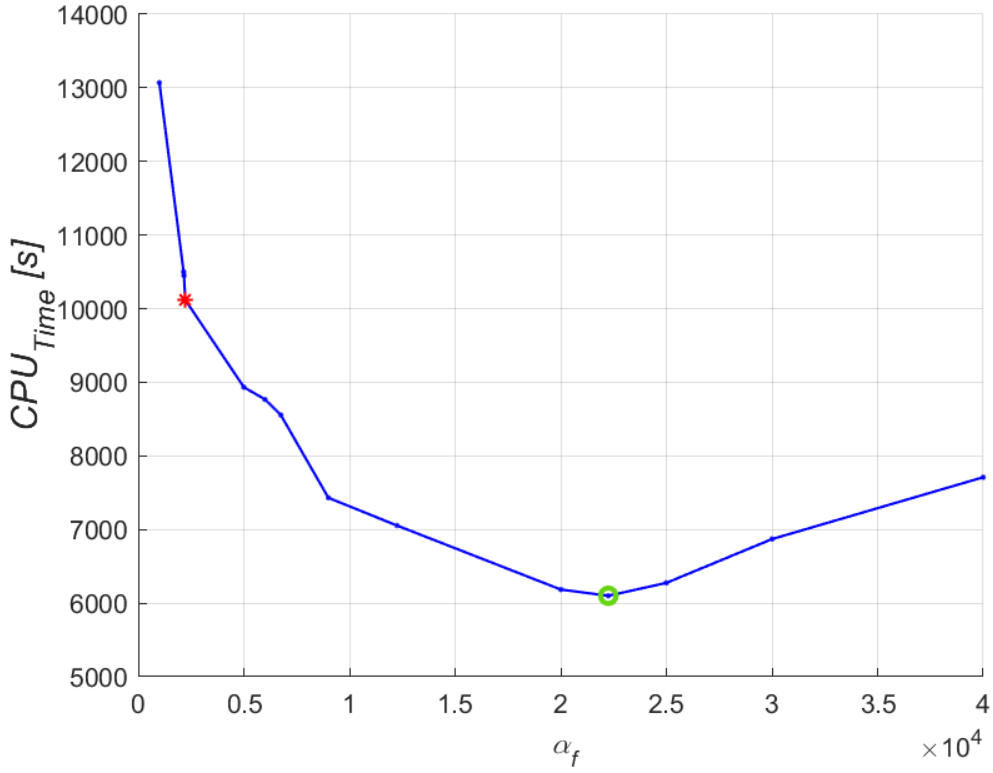


Figure 5.6: Comparison of the $CPU_{Time}$ performances to simulate $0.1s$ of the cardiac EFSI problem in the *Guccione setting* using *S2* with different values of $\alpha_f$. The value representing the range obtained with the theoretical analysis is highlighted in red: $\alpha_{fTopt} = 2225$. On the other hand the practical optimal value is highlighted in green, i.e. $\alpha_{fPopt,G2} = 22250$.

| $\alpha_f[\frac{kg}{m^2 \cdot s^2}]$ | 1000 | 2225 | 5000 | 6750 | 12250 | 22250 | 30000 | 40000 |
|---|---|---|---|---|---|---|---|---|
| **Avg #** | 23.3 | 17.7 | 15.3 | 14.2 | 11.45 | 9.55 | 10.8 | 12.2 |

Table 5.6: Comparison of the average number of iterations at each time step in the FSI Robin-Neumann loop of *G-2* with different values of $\alpha_f$. The value representing the range obtained with the theoretical analysis is highlighted in red: $\alpha_{fTopt} = 2225$. On the other hand the practical optimal value is highlighted in green, i.e. $\alpha_{fPopt,G2} = 22250$.

From table 5.6 and figure 5.6 it is quite astonishing to notice the extreme similarity with the analysis carried on *H-2* in terms of the optimality of the parameters, see Section 5.1.1. Indeed, the practical optimal value for *G-2* is again $\alpha_{fPopt,G2} = 22250$, the same of *H-2*. This may mean that we have calibrated quite well the parameters for the *Hooke*

*setting*, reproducing a simplified case but with the same properties in terms of response to the different parameters. We can observe from table 5.6 that the average number of iterations per time step in the FSI Robin-Neumann loop is halved passing from the theoretical optimal one (in red) to the practical optimal one (in green). We remark again that this could be expected due to the strong simplification of model and geometry in the theoretical analysis. However, it is important to have an initial guess sufficiently close to the effective range. In this sense the theoretical analysis is useful.

### 5.2.2. *Loosely Coupled EFSI Scheme 3*

Now we can move forward and pass to the application of our proposed new *Scheme 3* to the *Guccione setting*. Like we have done for the *Hooke setting* in Section 5.1.2, also here we have used *Scheme 3* with different values of $\alpha_f$ to simulate $0.5s$ with $\Delta t = 2 \cdot 10^{-4}s$.

In this case the simulations *G-3* reach convergence for $\alpha_f$ such that $100 < \alpha_f \leq 6750$, however only values $\alpha_f > 1000$ give reasonable qualitative results. The results of the simulations *G-3* with different values of $\alpha_f$ have been compared to the one obtained with *G-1* in terms of accuracy, stability and computational cost. We summarize such comparison in terms of the time evolution of ventricular chamber volume and average pressure in figure 5.7 and in terms of physiological indicators and $CPU_{Time}$ in table 5.7. We also present some 3D numerical results in figure 5.10 and figure 5.8.

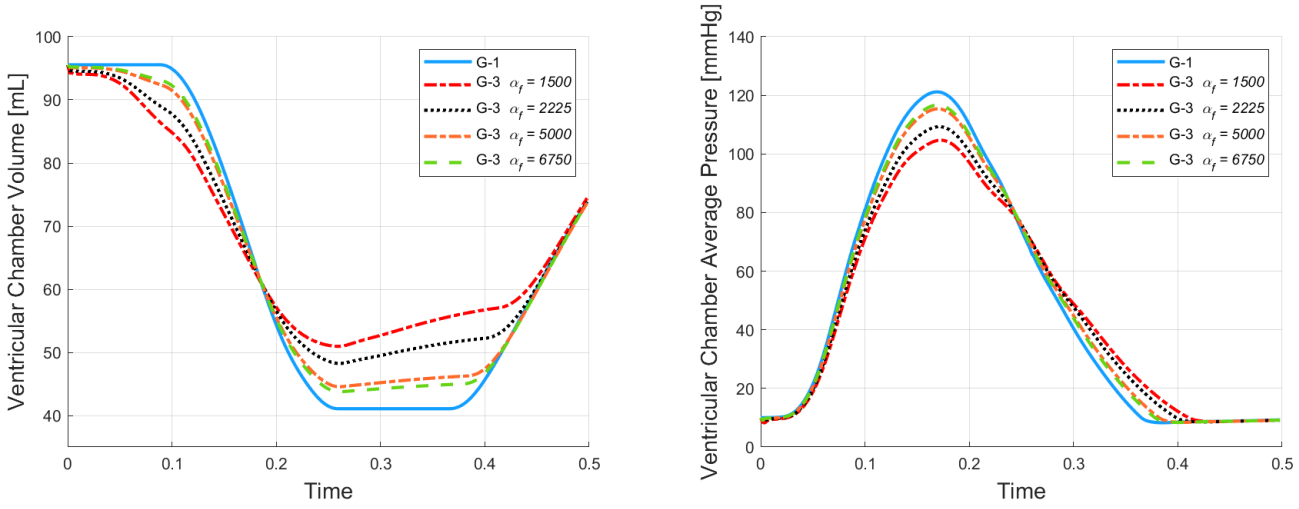


(a) Ventricular chamber volume.

(b) Ventricular chamber average pressure.

Figure 5.7: Time evolution of the ventricular chamber volume and pressure in *G-1* and *G-3* with different values of $\alpha_f$.

| | *G-1* | *G-3* $\alpha_f = 1500$ | *G-3* $\alpha_f = \alpha_{fTopt} = 2225$ | *G-3* $\alpha_f = 5000$ | *G-3* $\alpha_f = 6750$ |
|---|---|---|---|---|---|
| $p_{max}$ $[mmHg]$ | 121.17 | 104.7 | 109.32 | 115.39 | 116.68 |
| $E_f$ | 56.95% | 46.7% | 49.51% | 53.38% | 54.22% |
| $Time_{act}$ $[ms]$ | 91 | 91 | 91 | 91 | 91 |
| $max\|\|\boldsymbol{u}\|\|$ $[m/s]$ | 1.3 | 1.2 | 1 | 1.2 | 1.2 |
| $ILI_C$ | 0.01% | 10.65% | 7.44% | 3.37% | 2.55% |
| $ILI_R$ | 0.01% | 10.18% | 7.38% | 3.59% | 2.69% |
| $T_{O,A}$ $[s]$ | 0.09 | 0.098 | 0.096 | 0.092 | 0.092 |
| $T_{C,A}$ $[s]$ | 0.26 | 0.268 | 0.266 | 0.264 | 0.264 |
| $T_{O,M}$ $[s]$ | 0.366 | 0.412 | 0.4 | 0.384 | 0.38 |
| $CPU_{Time}$ $[s]$ | 7070 | 5548 | 4618 | 4724 | 5450 |

Table 5.7: Comparison of physiological indicators (i)-(vii) and computational costs obtained in *G-1* against the one obtained in *G-3* with different values of $\alpha_f$.

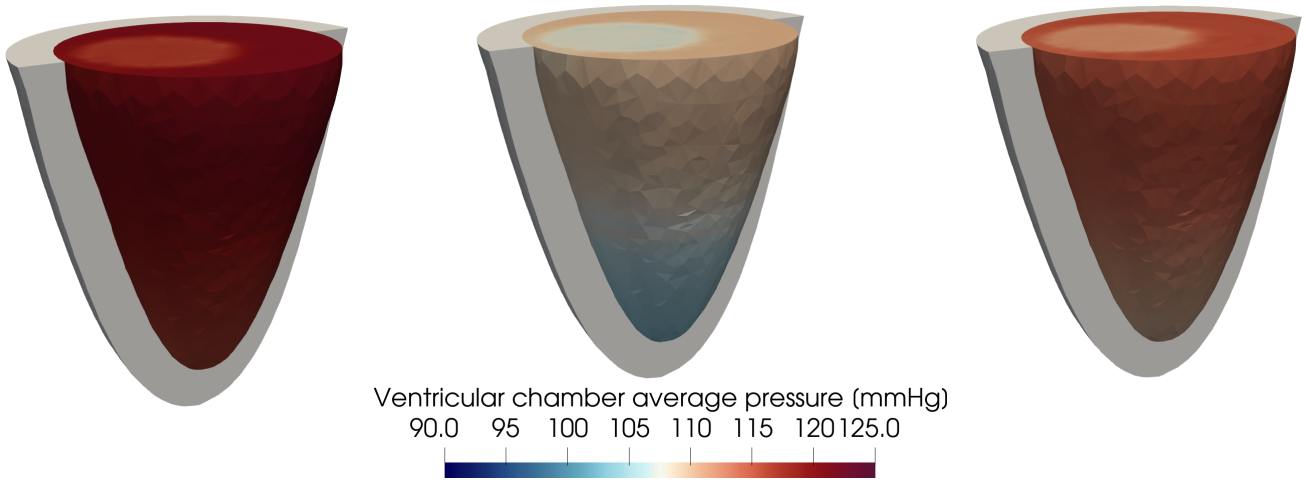


(a) *G-1*. (b) *G-3* $\alpha_f = 2225$. (c) *G-3* $\alpha_f = 5000$.

Figure 5.8: Comparison of the numerical solutions for the ventricular average chamber pressure obtained with *G-1* and *G-3* with different values of $\alpha_f$. The time instant at which the maximum pressure $p_{max}$ is reached is shown, i.e. $t = 0.17s$.

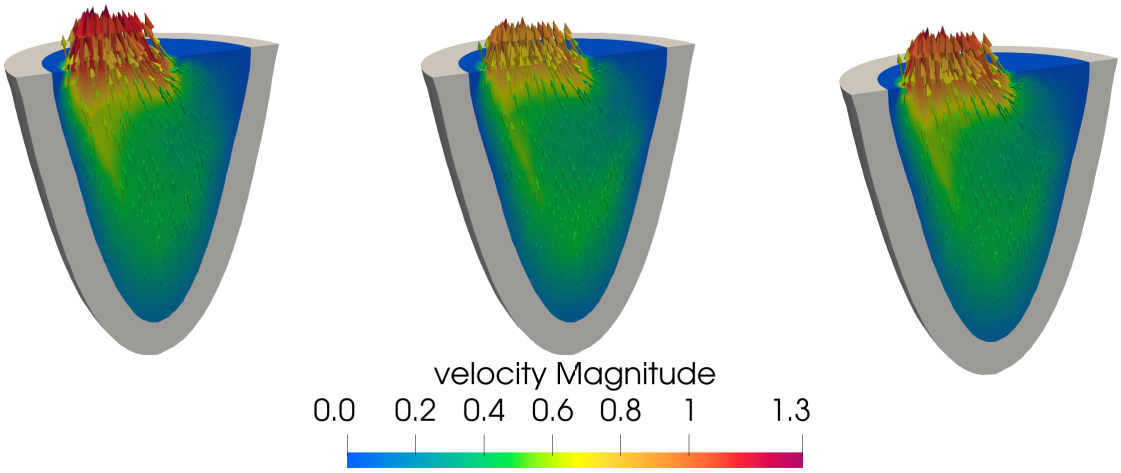


(a) *G-1*. (b) *G-3* $\alpha_f = 2225$ (c) *G-3* $\alpha_f = 5000$.

Figure 5.9: Comparison of the numerical solutions for the blood velocity magnitude obtained with *G-1* and *G-3* with different values of $\alpha_f$. A time instant during the ejection phase is shown: $t = 0.17s$.

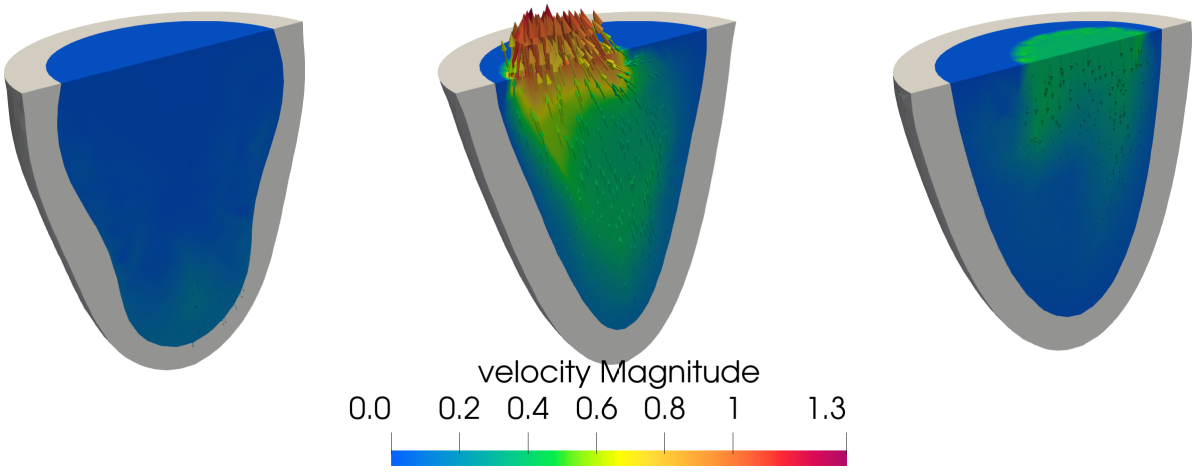


(a) $t = 0.074s$: isovolumic contraction. (b) $t = 0.18s$: ejection phase. (c) $t = 0.49s$: ventricular filling.

Figure 5.10: Numerical results obtained with *G-3* $\alpha_f = 5000$

From these numerical results we can observe the following things:

- in general we have again, as explained in the analysis of scheme *S3* in the *Hooke setting* (see Section 5.1.2), a negative correlation between $\alpha_f$ and the isovolumic

losses, that leads to a positive correlation between $\alpha_f$ and the ventricular chamber maximum average pressure $p_{max}$; this behavior can be deduced from figure 5.7a, figure 5.8 and table 5.7. Moreover, from figure 5.10 we can observe that also the velocity magnitude is positively correlated to the coefficient $\alpha_f$.

- For what concerns the range computed in Section 4.4.4 for the theoretical optimal values in the *Simplified Sphericl Model*, i.e. $[\alpha_{fTopt,min}, \alpha_{fTopt,max}] = [1906.4, 2415.1]$, it is contained in the range of converging, stable and qualitatively acceptable simulations individuated above ($1000 < \alpha_f \leq 6750$). Indeed, using the representative of the theoretical range (i.e. $\alpha_{fTopt} = 2225$), the physiological variations among the 4 cardiac phases are quite well captured as one can observe from figure 5.7a, together with the achievement of stabilty. However, we can see from table 5.7 that using $\alpha_{fTopt} = 2225$ we commit an error of $\sim 7/8\%$ in capturing the isovolumic phases, together with an error of $\sim 10\%$ in fulfilling the other physiological requirements I-IV. These results in terms of response to the parameter calibration are almost identical to the one obtained with the *Hooke setting* in Section 5.1.2, strengthening the hypothesis of having well calibrated such linearized setting. However with the *Guccione setting* the largest Robin interface parameter (i.e. $\alpha_f = 6750$) that can be used to obtain a converging simulation with *Scheme 3* is smaller than the one (i.e. $\alpha_f = 12250$) obtained for the *Hooke setting*. Maybe here we can not use higher values because other problems related to the non linearity and anisotropicity of the structure come into play; indeed, from table 5.7 we can see that passing from $\alpha_f = 5000$ to $\alpha_f = 6750$ the computational cost grows, therefore we can identify the range $5000 < \alpha_f \leq 6750$ as a transition zone towards non converging simulations.

- Besides being in a transition zone towards non converging simulations, the value $\alpha_f = 6750$ gives the best physiological indicators, fulfilling the physiological requirements with an error less than 3%. However, to achieve perfect stability and lower computational cost we suggest to use a value a little bit detached from the maximum one; therefore, we can say that the practical optimal value for *G-3* is $\alpha_{fPopt,G3} = 5000$, that gives anyway good physiological indicators, fulfilling the requirements I-V with an error less than 4%.

- For what concerns in general the $CPU_{Time}$, here we notice from table 5.7 a great improvement of *Scheme 3* with respect to *Scheme 1*; indeed, we obtained a $CPU_{Time}$ $\sim 35\%$ less than *G-1* in the case *G-3* with $\alpha_f = 5000$ or $\alpha_f = 2225$. This improvement is due to the fact that here the structure is non linear, therefore using *Scheme 1* we use a Newton solver for the whole FSI system, assembling the fluid and structure problem more than once ($\sim 2/3$ times, namely the number of iterations performed

by the Newton solver) per time step; on the other hand, with *Scheme 3* we solve one linear fluid problem and a non linear structure problem (again with Newton) only once per time step, therefore we assembly the fluid problem only once per time step. Being the assembly of the fluid problem one of the most significant contribution to the computational cost, *Scheme 3* becomes computationally more efficient assembling such system only once per time step. Moreover, this new proposed scheme has also the advantage of being modular, hence different already existing solvers can be employed.

- It is interesting to notice that also in the *Guccione setting*, the practical optimal value for *S2* found in the previous subsection, i.e. $\alpha_{fPopt,G2} = 22250$, does not give a converging simulation using *Scheme 3*.

After all this discussion we can finally say that the range to obtain the most stable and computationally efficient results using our new proposed *Loosley-Coupled EFSI Scheme* to simulate the *Guccione setting* is:

$$1500 < \alpha_f \leq 5000, \tag{5.1}$$

Therefore, the theoretical range computed in Section 4.4.4, namely $1906.4 \leq \alpha_f \leq 2415.1$ is perfectly included in the experimentally calibrated one (5.1).

### 5.2.3. *Scheme 4*

Given the important $CPU_{Time}$ improvement highlighted in the just discussed section, we have again performed the further inspection on the possibility to perform 2 iterations instead of 1 in the Robin-Neumann FSI loop, using *Scheme 4*. We have used both the theoretical value $\alpha_{fTopt} = 2225$ and the practical optimal value calibrated for *S3* in the *Guccione setting*, i.e. $\alpha_{fPopt,G3} = 5000$, to carry out such analysis. In figure 5.11 and figure 5.12 is reported a comparison between *G-1*, *G-2* and *G-4* using the above cited $\alpha_f$; these comparisons are in terms of the time evolution of the ventricular chamber volume and average pressure. Finally in table 5.8 and table 5.9 the physiological indicators (i)-(vii) obtained with such simulations are reported.

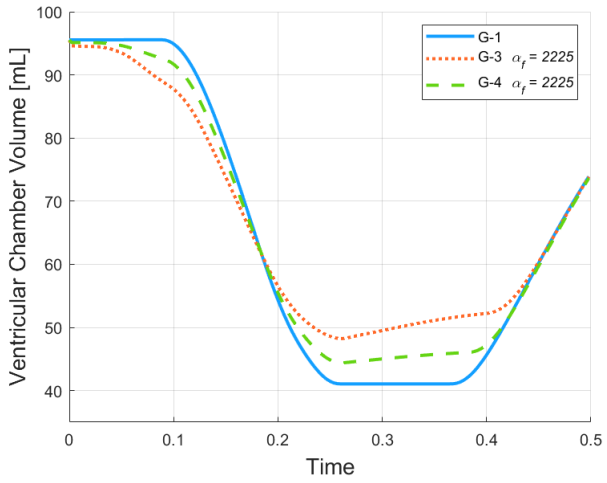


(a) Ventricular chamber volume.

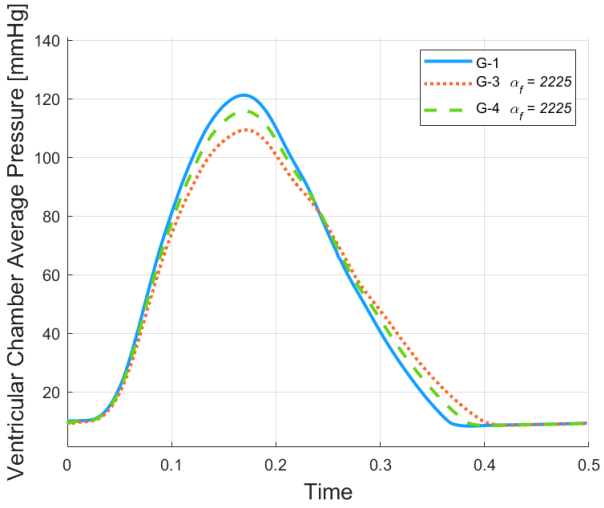


(b) Ventricular chamber average pressure.

Figure 5.11: time evolution of the ventricular chamber volume and pressure in *G-1*, *G-3* and *G-4* with $\alpha_f = \alpha_{fTopt} = 2225$.

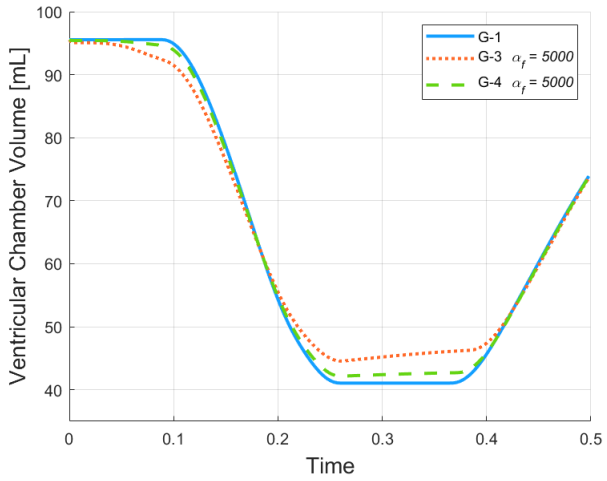


(a) Ventricular chamber volume.

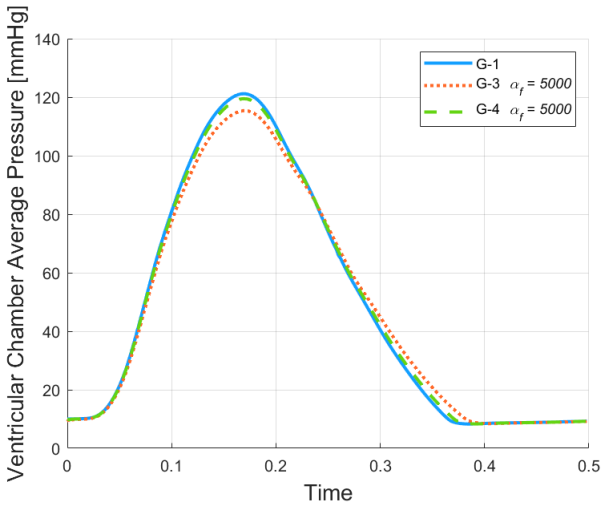


(b) Ventricular chamber average pressure.

Figure 5.12: time evolution of the ventricular chamber volume and pressure in *G-1*, *G-3* and *G-4* with $\alpha_f = 5000$.

| | *G-1* | *G-3* $\alpha_f = \alpha_{fTopt} = 2225$ | *G-4* $\alpha_f = \alpha_{fTopt} = 2225$ |
|---|---|---|---|
| $p_{max}$ $[mmHg]$ | 121.17 | 109.32 | 115.77 |
| $E_f$ | 56.95% | 49.51 | 53.54% |
| $Time_{act}$ $[ms]$ | 91 | 91 | 91 |
| $max\|\|\boldsymbol{u}\|\|$ $[m/s]$ | 1.3 | 1 | 1.2 |
| $ILI_C$ | 0.01% | 7.44% | 3.17% |
| $ILI_R$ | 0.01% | 7.38% | 3.52% |
| $T_{O,A}$ $[s]$ | 0.09 | 0.096 | 0.092 |
| $T_{C,A}$ $[s]$ | 0.26 | 0.266 | 0.264 |
| $T_{O,M}$ $[s]$ | 0.366 | 0.4 | 0.384 |
| $CPU_{Time}$ $[s]$ | 7070 | 4618 | 8452 |

Table 5.8: Comparison of physiological indicators (i)-(vii) and computational costs obtained using *Scheme 1*, *Scheme 3* and *Scheme 4* to simulate the *Guccione setting* for $0.5s$ with the theoretical optimal value $\alpha_f = \alpha_{fTopt} = 2225$.

| | *G-1* | *G-3* $\alpha_f = 5000$ | *G-4* $\alpha_f = 5000$ |
|---|---|---|---|
| $p_{max}$ $[mmHg]$ | 121.17 | 115.39 | 119.47 |
| $E_f$ | 56.95% | 53.38% | 55.88% |
| $Time_{act}$ $[ms]$ | 91 | 91 | 91 |
| $max\|\|\boldsymbol{u}\|\|$ $[m/s]$ | 1.3 | 1.2 | 1.3 |
| $ILI_C$ | 0.01% | 3.37% | 0.92% |
| $ILI_R$ | 0.01% | 3.59% | 1.24% |
| $T_{O,A}$ $[s]$ | 0.09 | 0.092 | 0.09 |
| $T_{C,A}$ $[s]$ | 0.26 | 0.264 | 0.262 |
| $T_{O,M}$ $[s]$ | 0.366 | 0.384 | 0.372 |
| $CPU_{Time}$ $[s]$ | 7070 | 4724 | 8325 |

Table 5.9: Comparison of physiological indicators (i)-(vii) and computational costs obtained using *Scheme 1*, *Scheme 3* and *Scheme 4* to simulate the *Guccione setting* for $0.5s$ with $\alpha_f = 5000$.

From figure 5.11a and figure 5.12a we notice that here the isovolumic phases are better captured by *Scheme 4* with respect to *Scheme 3*, even with the theoretical optimal value.

Therefore from table 5.8 and table 5.9 we notice that the isovolumic losses indicators are more than halved using *S4* with respect to the one obtained with *S3*. With *S4* we obtain computational costs that are higher than the ones obtained using *S1*, but however comparable. Indeed, they are $\sim 15\%$ higher, but using a modular scheme, hence different solvers can be employed.

# 6 | Conclusions and future developments

## 6.1. Conclusions

We have obtained encouraging results with our proposed new *Loosely-coupled EFSI Scheme 3* (see Section 3.3) applied to the cardiac EFSI Problem described in Chapter 2. The range of theoretical values of $\alpha_f$ for the Robin interface parameter, chosen performing a theoretical analysis on the *Simplified Spherical Model* (see Section 4.4), gave stability and accuracy with an error of $\sim 10\%$ in reproducing the physiological behavior described by requirements I-V. However, to obtain a higher level of accuracy, a manual calibration of the Robin parameter $\alpha_f$ is needed; with the practical optimal $\alpha_{Popt,G3}$ we obtained an error of $\sim 3/4\%$ in reproducing the physiological behavior. It is important to remark that the theoretical analysis was expected to provide a range of values that are not the effective optimal ones for the EFSI Problem due to the strong simplification of model and geometry of the *Spherical Simplified Model*. However, it is important to have an initial guess sufficiently close to the effective range. In this sense the theoretical analysis was useful. Therefore, we have established a practical range for the choice of the Robin parameters (5.1) to obtain stable, accurate and computational efficient simulations; we have ascertained that the theoretical range (4.12) was completely contained inside it. Comparing this new *Loosely-coupled EFSI Scheme 3* with the *Staggered E-Monolithic FSI Scheme 1*, we have noticed that:

- *Scheme 1* perfectly captures the isovolumic phases, while with *Scheme 3* we commit an error in reproducing such phases due to the spurious numerical fluxes given by the explicit treatment of the FSI coupling conditions. However, with the optimal practical value $\alpha_{Popt,G3} = 5000$ this error is less than 4%, whilst using values in the theoretical range (4.12) we commit an error of $\sim 8\%$.
- *Scheme 3* is $\sim$ 35% faster than *Scheme 1* and has also the advantage of being modular, i.e. we can use different already existing solvers.

Moreover, we have also investigated *Scheme 2* with different choices for $\alpha_f$. We have ascertained that it gives the same identical results of *Scheme 1* for a wide range of parameters. However, *Scheme 2* is computationally inefficient; indeed, also using the calibrated optimal value $\alpha_f = 22250$ it is 4 times slower than *Scheme 1*.

Finally, we have explored two possibilities to reduce the inaccuracy of *Scheme 3* in reproducing the isovolumic phases:

- the possibility of halving the time step, obtaining better results using *Scheme 3* in terms of reproducing a physiological behavior, but inevitably doubling the computational cost;
- the possibility of performing 2 iterations instead of 1 in the Robin-Neumann FSI loop (i.e. *Scheme 4*), leading to an improvement in reproducing the physiological behavior. Also in this second possibility we obtained an enhance of the computational cost, that remains however comparable to the one using *Scheme 1*; moreover, *Scheme 4* has the advantage to be modular.

A final comparison between *Scheme 1,2,3* and *4* in terms of computational cost and accuracy in reproducing the isovolumic phases (an average of the two Isovolumic Loss Indicators defined in Section 4.2, i.e. $ILI_{AVG} = \frac{ILI_C + ILI_R}{2}$) simulating the *Guccione setting* for $0.5s$ using $\Delta t = 2 \cdot 10^{-4} s$ can be found in table 6.1. We have chosen to show the accuracy in reproducing the isovolumic phases because it is the most reliable indicator to discriminate between different results; indeed, it influences all the other physiological indicators, hence behaviors.

| | *G-1* | *G-2*(22250) | *G-3*(2225) | *G-3*(5000) | *G-4*(2225) | *G-4*(5000) |
|---|---|---|---|---|---|---|
| $CPU_{Time}$ $[s]$ | 7070 | 30000 | 4618 | 4724 | 8452 | 8325 |
| $ILI_{AVG}$ $[s]$ | 0.01% | 0.01% | 7.41% | 3.48% | 3.35% | 1.08% |

Table 6.1: Comparison of the computational costs and average Isovolumic Loss Indicator $ILI_{AVG}$ obtained in *G-1* and in *G-2*, *G-3* and *G-4* with the optimal calibrated parameters and with the theoretical one. We have simulated $0.5s$ with $\Delta t = 2 \cdot 10^{-4} s$.

## 6.2. Future developments

The work that we have presented has one important limitation; indeed, we have introduced important simplifications in the description of the geometry of the human ventricle, using a truncated ellipsoid with two overlapping orifices for the valves instead of a realistic

geometry. However, we have obtained encouraging results using the new *Loosely-Coupled EFSI Scheme*, hence a possible development of this work could be the application of the same analysis to a more complex model of the left ventricle to see if similar results can be obtained also in such context. On the other hand, from the theoretical point of view, a formal linearization of the Guccione model to find the parameters $\lambda$ and $\gamma_{ST}$ needed to perform the theoretical calibration of $\alpha_f$ can be done. Indeed, in this work such calibration (see Section 4.4.3) was performed manually, but it can be done also linearizing formally the non-linear Guccione law for the structure. If such linearization is intended to be done, one would have to pay attention to the fact that the Guccione law is also anisotropic. Nonetheless, the similarity of the results obtained with the *Guccione* and *Hooke settings* in the present work indicates that our approximation was sufficiently effective.

# Bibliography

[1] Zygote 3D human anatomy models. URL `https://www.zygote.com`.

[2] P. C. Africa. Scalable adaptive simulation of organic thin-film transistors. 2019.

[3] V. Alastrue, A. Garcia, E. Peña, J. F. Rodriguez, M. A. Martinez, and M. Doblaré. Numerical framework for patient-specific computational modelling of vascular tissue. *International Journal for Numerical Methods in Biomedical Engineering*, pages 35–51, 2010.

[4] D. Ambrosi and Pezzuto. Active stress vs. active strain in mechanobiology: constitutive issues. *Journal of Elasticity*, pages 199–212, 2012.

[5] D. Ambrosi, G. Arioli, F. Nobile, and A. Quarteroni. Electromechanical coupling in cardiac dynamics: the active strain approach. *SIAM Journal on Applied Mathematics*, page 605–621, 2011.

[6] J. Arciero, L. Carichino, S. Cassani, and G. Guidoboni. *Mathematical Modeling of Blood Flow in the Eye*, pages 101–157. Springer International Publishing, Cham, 2019.

[7] M. Astorino, F. Chouly, and M. Fernández. Robin based semi-implicit coupling in fluid-structure interaction: stability analysis and numerics. *SIAM J. Sci. Comput.*, page 4041–4065, 2008.

[8] H. Athari, A. Bolukbasi, and D. Ciloglu. The application of FSI techniques in modeling of realistic pulmonary systems. *International Journal of Mechanical and Mechatronics Engineering*, 2015.

[9] L. Azzolin, L. Dedè, A. Gerbi, and A. Quarteroni. Effect of fibre orientation and bulk modulus on the electromechanical modelling of human ventricles. *Mathematics In Engineering*, pages 614–638, 2020.

[10] S. Badia, F. Nobile, and C. Vergara. Fluid-structure partitioned procedures based on Robin transmission conditions. *Journal of Computational Physics*, page 7027–7051, 2008.

[11] S. Badia, F. Nobile, and C. Vergara. Robin-Robin preconditioned Krylov methods for fluid-structure interaction problems. *Comput. Methods Appl. Mech. Eng.*, page 2768–2784, 2009.

[12] J. W. Banks, W. D. Henshaw, and D. W. Schwendeman. An analysis of a new stable partitioned algorithm for FSI problems. part i: Incompressible flow and elastic solids. *J. Comput. Physics*, page 108–137, 2014.

[13] A. Barker and X. Cai. Scalable parallel methods for monolithic coupling in fluid-structure interaction with application to blood flow modeling. *Journal of Computational Physics*, pages 642–659, 2010.

[14] N. Barnafi, S. Di Gregorio, L. Dede', P. Zunino, C. Vergara, and A. Quarteroni. A multiscale poromechanics model integrating myocardial perfusion and the epicardial coronary vessel. *SIAM Journal of Applied Mathematics*, to appear.

[15] K. J. Bathe, H. Zhang, and M. H. Wang. Finite element analysis of incompressible and compressible fluid flows with free surfaces and structural interactions. *Computers and Structures*, 56(2):193–213, 1995.

[16] J. D. Bayer, R. C. Blake, G. Plank, and N. A. Trayanova. A novel rule-based algorithm for assigning myocardial fiber orientation to computational heart models. *Annals of Biomedical Engineering*, pages 2243–2254, 2012.

[17] Y. Bazilevs, V. M. Calo, J. A. Cottrell, T. J. Hughes, A. Reali, and G. Scovazzi. Variational multiscale residual-based turbulence modeling for large eddy simulation of incompressible flows. *Computers and Fluids*, 2007.

[18] L. Bennati, C. Vergara, M. Domanin, C. Malloggi, D. Bissacco, S. Trimarchi, V. Silani, G. Parati, and R. Casana. A computational fluid structure interaction study for carotids with different atherosclerotic plaques. *Journal of Biomechanical Engineering*, 2021.

[19] C. Bertoglio and A. Caiazzo. A tangential regularization method for backflow stabilization in hemodynamics. *Journal of Computational Physics*, pages 162–171, 2014.

[20] F. J. Blom. A monolithical fluid–structure interaction algorithm applied to the piston problem. *Comput. Meth. Appl. Mech. Eng.*, pages 369–391, 1998.

[21] M. Bucelli, L. Dedè, A. Quarteroni, and C. Vergara. Partitioned and monolithic algorithms for the numerical solution of cardiac fluid-structure interaction. *MOX report n. 78/2021*, 2021.

[22] E. Burman and M. Fernández. Stabilized explicit coupling for fluid–structure interaction using Nitsche's method. *C.R. Math. Acad. Sci. Paris*, pages 467–472, 2007.

[23] E. Burman and M. Fernández. Stabilization of explicit coupling in fluid–structure interaction involving fluid incompressibility. *Comput. Methods Appl. Mech. Eng.*, pages 766–784, 2009.

[24] E. Burman and M. Fernández. Coupling schemes for incompressible fluid–structure interaction: implicit, semi-implicit and explicit. *SMA J.*, pages 59–108, 2011.

[25] C. Burstedde, L. C. Wilcox, and O. Ghattas. p4est: scalable algorithms for parallel adaptive mesh refinement on forests of octrees. pages 1103–1133, 2011.

[26] J. Carro, J. F. Rodriguez, V. Monasterio, and E. Pueyo. Limitations in electrophysiological model development and validation caused by differences between simulations and experimental protocols. pages 53–64, 2017.

[27] P. Causin, J. F. Gerbeau, and F. Nobile. Added-mass effect in the design of partitioned algorithms for fluid-structure problems. *Comput. Methods Appl. Mech. Eng.*, pages 4506–4527, 2005.

[28] S. Chandra, V. Gnanaruban, F. Riveros, J. F. Rodriguez, and E. A. Finol. A methodology for the derivation of unloaded abdominal aortic aneurysm geometry with experimental validation. *J Biomech Eng.*, 2016.

[29] P. Colli-Franzone, , L. Pavarino, and S. Scacchi. *Mathematical Cardiac Electrophysiology*. Springer, 2014.

[30] L. Dedè, F. Menghini, and A. Quarteroni. Computational fluid dynamics of blood flow in an idealized left human heart. *International Journal for Numerical Methods in Biomedical Engineering*, 2019.

[31] S. Deparis, D. Forti, G. Grandperrin, and A. Quarteroni. FaCSI: A block parallel preconditioner for fluid-structure interaction in hemodynamics. *Journal of Computational Physics*, pages 700–718, 2016.

[32] S. Di Gregorio, M. Fedele, G. Pontone, A. F. Corno, P. Zunino, C. Vergara, and A. Quarteroni. A multiscale computational model of myocardial perfusion in the human heart. *Journal of Computational Physics*, 2021.

[33] M. Domanin, L. Bennati, C. Vergara, D. Bissacco, C. Malloggi, V. Silani, G. Parati,

and R. Trimarchi, S. Casana. Fluid structure interaction analysis to stratify the behavior of different atheromatous carotid plaques. *MOX Report n. 22/2021*, 2021.

[34] R. Doste, D. Soto-Iglesias, G. Bernardino, A. Alcaine, R. Sebastian, S. Giffard-Roisin, M. Sermesant, A. Berruezo, D. Sanchez-Quintana, and O. Camara. A rule-based method to model myocardial fiber orientation in cardiac biventricular geometries with outflow tracts. *International Journal for Numerical Methods in Biomedical Engineering*, 2019.

[35] C. Farhat, P. Geuzaine, and K. G. van der Zee. Provably second-order time-accurate loosely-coupled solution algorithms for transient nonlinear computational aeroelasticity. *Comput. Methods Appl. Mech. Eng.*, pages 1973–2001, 2006.

[36] M. Fedele, E. Faggiano, L. Dedè, and A. Quarteroni. A patient-specific aortic valve model based on moving resistive immersed implicit surfaces. *Biomechanics and Modeling in Mechanobiology*, 2017.

[37] M. Fernandez, J. Mullaert, and M. Vidrascu. Explicit Robin–Neumann schemes for the coupling of incompressible fluids with thin-walled structures. *Comput. Methods Appl. Mech. Engrgy*, page 566–593, 2013.

[38] M. A. Fernandez, J. F. Gerbeau, and C. Grandmont. A projection semi-implicit scheme for the coupling of an elastic structure with an incompressible fluid. *J. Num. Methods Engrg.*, page 794–821, 2007.

[39] L. Formaggia, E. Miglio, A. Mola, and N. Parolini. Fluid-structure interaction problems in free surface flows: application to boat dynamics. *Int. J. Numer. Meth. Fluids*, pages 965–978, 2008.

[40] C. Forster, W. Wall, and E. Ramm. Artificial added mass instabilities in sequential staggered coupling of nonlinear structures and incompressible viscous flow. *Comput. Methods Appl. Mech. Eng.*, pages 1278–1293, 2007.

[41] D. Forti and L. Dedè. Semi-implicit BDF time discretization of the navier-stokes equations with VMS-LES modeling in a high performance computing framework. *Computers and Fluids*, pages 168–182, 2015.

[42] I. Fumagalli, M. Fedele, C. Vergara, L. Dede', S. Ippolito, F. Nicolò, C. Antona, R. Scrofani, and A. Quarteroni. An image-based computational hemodynamics study of the systolic anterior motion of the mitral valve. *Computers in Biology and Medicine*, 2020.

[43] M. Gee, U. Kuttler, and W. Wall. Truly monolithic algebraic multigrid for fluid-structure interaction. *Int. J. Num. Methods Engrgy*, page 987–1016, 2011.

[44] L. Gerardo-Giorda, F. Nobile, and C. Vergara. Analysis and optimization of Robin-Robin partitioned procedures in fluid-structure interaction problems. *SIAM J. Num. Anal.*, pages 2091–2116, 2010.

[45] A. Gerbi. Numerical approximation of cardiac electro-fuid-mechanical models: coupling strategies for large-scale simulation. *EPFL PhD thesis*, 2018.

[46] A. Gerbi, L. Dede', and A. Quarteroni. A monolithic algorithm for the simulation of cardiac electromechanics in the human left ventricle. *Mathematics in Engineering*, pages 1–37, 2018.

[47] A. Gerhard, Holzapfel, and W. O. Ray. Constitutive modelling of passive myocardium: A structurally based framework for material characterization. *Philosophical Transactions of the Royal Society A: Mathematical, Physical and Engineering Sciences*, pages 3445–3475, 2009.

[48] N. D. Ghista, H. Sandler, and H. W. Vayo. Elastic modulus of the human intact left-ventricle determination and physiological interpretation. *Medical and Biological Engineering*, page 151–161, 1975.

[49] G. Gigante and C. Vergara. Analysis and optimization of the generalized schwarz method for elliptic problems with application to fluid-structure interaction. *Numer. Math.*, page 369–404, 2015.

[50] G. Gigante and C. Vergara. On the choice of interface parameters in Robin–Robin loosely coupled schemes for fluid–structure interaction. *Fluids*, page 109–119, 2021.

[51] G. Gigante and C. Vergara. On the stability of a loosely-coupled scheme based on a Robin interface condition for fluid-structure interaction. *Computers and Mathematics with Applications*, page 109–119, 2021.

[52] G. Gigante, C. Vergara, and G. Sambataro. Optimized Schwarz method for spherical interfaces with application to fluid structure interaction. *SIAM Journal On Scientific compututing*, pages 751–770, 2020.

[53] J. M. Guccione and A. D. McCulloch. Finite element modeling of ventricular mechanics. *Teory of Heart, Springer*, 1991.

[54] G. Guidoboni, R. Glowinski, N. Cavallini, and S. Canic. Stable loosely-coupled type

algorithm for fluid–structure interaction in blood flow. *Journal of Computational Physics*, 228(18):6916–6937, 2009.

[55] E. Heidenreich, J. M. Ferrero, M. Doblaré, and J. F. Rodríguez. Adaptive macro finite elements for the numerical solution of monodomain equations in cardiac electrophysiology. pages 2335–2348, 2010.

[56] E. A. Heidenreich, J. F. Rodriguez, F. J. Gaspar, and M. Doblare. Fourth-order compact schemes with adaptive time step for monodomain reaction-diffusion equations. pages 39–55, 2007.

[57] M. Heil. An efficient solver for the fully coupled solution of large-displacement fluid-structure interaction problems. *Comput. Methods Appl. Mech. Engrgy*, pages 1–23, 2004.

[58] G. Hermann, Matthies, and J. Steindorf. Partitioned strong coupling algorithms for fluid–structure interaction. *Computers and Structures*, 81(8):805–812, 2003.

[59] M. Hirschvogel, M. Bassilious, L. Jagschies, S. M. Wildhirt, and M. W. Gee. A monolithic 3d-0d coupled closed-loop model of the heart and the vascular system: experiment-based parameter estimation for patient-specific cardiac mechanics. *International journal for numerical methods in biomedical engineering*, 2017.

[60] C. Hoogendoorn, R. Sebastian, J. F. Rodriguez, K. Lekadir, and A. F. Frangi. An atlas and data-driven approach to initializing reaction-diffusion systems in computer cardiac electrophysiology. 2017.

[61] A. M. Katz. Physiology of the heart. *M - Medicine Series. Wolters Kluwer Health/Lippincott Williams and Wilkins Health*, 2010.

[62] M. Landajuela, C. Vergara, A. Gerbi, L. Dede', L. Formaggia, and A. Quarteroni. A numerical approximation of the electromechanical coupling in the left ventricle with inclusion of the purkinje network. *Int. Journal on Numerical Methods in Biomedical Engineering*, 2018.

[63] M. Lange, S. Palamara, T. Lassila, C. Vergara, A. Quarteroni, and A. F. Frangi. Improved hybrid/gpu algorithm for solving cardiac electrophysiology problems on purkinje networks. *Int. J. Numer. Meth. Biomed. Eng.*, 2017.

[64] M. Lombardi, M. Cremonesi, A. Giampieri, N. Parolini, and A. Quarteroni. A strongly coupled fluid-structure interaction model for wind-sail simulation. *High Performance Yacht Design conference, The Royal Institution of Naval Architects, London, UK*, 2012.

[65] F. Marcinno', A. Zingaro, I. Fumagalli, L. Dede', and C. Vergara. A computational study of blood flow dynamics in the pulmonary arteries. *MOX Report n. 73/2021*, 2021.

[66] A. Mena, J. M. Ferrero, and J. F. Rodriguez. Gpu accelerated solver for nonlinear reaction-diffusion systems. application to the electrophysiology problem. *Computer Physics Communications*, pages 280–289, 2015.

[67] M. E. Moghadam, Y. Bazilevs, T. Y. Hsia, I. E. Vignon-Clementel, and A. L. Marsden. A comparison of outlet boundary treatments for prevention of backflow divergence with relevance to blood flow simulations. *Computational Mechanics*, pages 277–291, 2011.

[68] F. Nobile and C. Vergara. An effective fluid-structure interaction formulation for vascular dynamics by generalized Robin conditions. *SIAM J. Sc. Comp.*, pages 731–763, 2008.

[69] F. Nobile and C. Vergara. Partitioned algorithms for fluid-structure interaction problems in haemodynamics. *J. Math*, pages 443–467, 2012.

[70] F. Nobile, M. Pozzoli, , and C. Vergara. Time accurate partitioned algorithms for the solution of fluid-structure interaction problems in haemodynamics. *Comput. and Fluids*, page 470–482, 2013.

[71] F. Nobile, C. Vergara, and M. Pozzoli. Inexact accurate partitioned algorithms for fluid-structure interaction problems with finite elasticity in haemodynamics. *Journal of Computational Physics*, page 598–617, 2014.

[72] D. Nordsletten, D. McCormick, P. J. Kilner, P. Hunter, D. Kay, and N. P. Smith. Fluid-solid coupling for the investigation of diastolic and systolic human left ventricular function. *International Journal for Numerical Methods in Biomedical Engineering*, pages 1017–1039, 2011.

[73] D. A. Nordsletten, S. A. Niederer, M. P. Nash, P. J. Hunter, and N. P. Smith. Coupling multiphysics models to cardiac mechanics. *Biomechanics and Modeling in Mechanobiology*, 2011.

[74] R. W. Ogden. Non-linear elastic deformations. *Courier Corporation*, 1997.

[75] K. C. Park, C. A. Felippa, and J. A. De Runtz. Stabilisation of staggered solution procedures for fluid-structure interaction analysis. *Comput. Methods Appl. Mech. Eng.*, 1977.

[76] S. Patil, R. Lietz, S. Woodiga, and H. e. a. Ahn. Fluid structure interaction simulations applied to automotive aerodynamics. *International Journal for Numerical Methods in Biomedical Engineering*, 2019.

[77] M. R. Pfaller, J. M. Hörmann, M. Weigl, A. Nagler, R. Chabiniok, C. Bertoglio, and W. A. Wall. The importance of the pericardium for cardiac biomechanics: from physiology to computational modeling. *Biomech Model Mechanobiol.*, 2019.

[78] R. Piersanti, P. C. Africa, M. Fedele, C. Vergara, L. Dede', A. F. Corno, and A. Quarteroni. Modeling cardiac muscle fibers in ventricular and atrial electrophysiology simulations. *Computer Methods in Applied Mechanics and Engineering*, 2021.

[79] S. Piperno and C. Farhat. Partitioned procedures for the transient solution of coupled aeroelastic problems-part 2: energy transfer analysis and three-dimensional applications. *Comput. Methods Appl. Mech. Eng.*, pages 3147–3170, 2001.

[80] S. Pozzi and C. Vergara. Mathematical and numerical models of atherosclerotic plaque progression in carotid arteries. *In "Numerical Mathematics and Advanced Applications ENUMATH 2019" - Lecture Notes in Computational Science and Engineering*, 2021.

[81] A. Quarteroni. *Numerical Models for Differential Problems*. Springer, 2017.

[82] A. Quarteroni and M. Fedele. Polygonal surface processing and mesh generation tools for numerical simulations of the complete cardiac function. *International Journal for Numerical Methods in Biomedical Engineering*, 2021.

[83] A. Quarteroni, A. Manzoni, and C. Vergara. The cardiovascular system: mathematical modelling, numerical algorithms and clinical applications. *Acta Numer. 26*, pages 365–590, 2017.

[84] A. Quarteroni, C. Vergara, and M. Landajuela. Mathematical and numerical description of the heart function. *International Journal Numerical Methods in Biomedical Engineering*, pages 171–177, 2018.

[85] A. Quarteroni, L. Dede', A. Manzoni, and C. Vergara. Mathematical modelling of the human cardiovascular system: Data, numerical approximation, clinical applications. *Cambridge University Press*, 2019.

[86] F. Regazzoni, L. Dede', and A. Quarteroni. Active contraction of cardiac cells: a reduced model for sarcomere dynamics with cooperative interactions. *Biomechanics and Modeling in Mechanobiology*, pages 1663–1686, 2018.

[87] F. Regazzoni, L. Dede', and A. Quarteroni. Machine learning for fast and reliable solution of time-dependent differential equations. 2019.

[88] F. Regazzoni, L. Dede', and A. Quarteroni. Machine learning of multiscale active force generation models for the efficient simulation of cardiac electromechanics. *Computer Methods in Applied Mechanics and Engineering*, 2020.

[89] F. Regazzoni, L. Dede', and A. Quarteroni. Biophysically detailed mathematical models of multiscale cardiac active mechanics. *PLOS Computational Biology*, 2020.

[90] F. Regazzoni, M. Salvador, P. C. Africa, M. Fedele, L. Dedè, and A. Quarteroni. A cardiac electromechanics model coupled with a lumped parameters model for closed-loop blood circulation. *Journal of Computational Physics*, 2022.

[91] C. Riccobene, E. Schenone, and N. Parolini. Reduced models for liquid food packaging systems. *Advances on Links Between Mathematics and Industry*, pages 45–58, 2019.

[92] S. Rossi, T. Lassila, R. Ruiz-Baier, A. Sequeira, and A. Quarteroni. Thermodynamically consistent orthotropic activation model capturing ventricular systolic wall thickening in cardiac electromechanics. *European Journal of Mechanics A/Solids*, pages 129–142, 2014.

[93] A. Santiago, J. Aguado-Sierra, M. Zavala-Aké, R. Doste-Beltran, S. Gòmez, R. Arìs, and J. C. Cajas. Fully coupled fluid-electro-mechanical model of the human heart for supercomsputer. *International Journal for Numerical Methods in Biomedical Engineering*, 2018.

[94] K. Stein, T. Tezduyar, and R. Benney. Mesh moving techniques for fluid-structure interactions. *Journal of Applied Mechanics*, pages 58–63, 2003.

[95] S. Stella, F. Regazzoni, C. Vergara, L. Dede', and A. Quarteroni. A fast cardiac electromechanics model coupling the eikonal and the nonlinear mechanics equations. 2021.

[96] M. Strocchi, M. A. Gsell, C. M. Augustin, O. Razeghi, C. H. Roney, J. A. Prassl, E. J. Vigmond, J. M. Behar, J. S. Gould, C. A. Rinaldi, M. J. Bishop, G. Plank, and S. A. Niederer. Simulating ventricular systolic motion in a four-chamber heart model with spatially varying Robin boundary conditions to model the effect of the pericardium. *Journal of Biomechanics*, 2020.

[97] A. Tagliabue, L. Dedè, and Quarteroni. Complex blood flow patterns in an idealized left ventricle: A numerical study. *Chaos*, 2017.

[98] T. Tusscher and V. Panfilov. Alternans and spiral breakup in a human ventricular tissue model. *American Journal of Physiology - Heart and Circulatory Physiology*, pages 1088–1100, 2006.

[99] T. K. Tusscher, D. Noble, P. J. Noble, and A. V. Panfilov. A model for human ventricular tissue. 2004.

[100] T. Usyk, I. LeGrice, and A. D. McCulloch. Computational model of three-dimensional cardiac electromechanics. *Computing and Visualization in Science*, page 249–257, 2002.

[101] C. Vergara, S. Palamara, D. Catanzariti, F. Nobile, E. Faggiano, C. Pangrazzi, M. Centonze, M. Maines, A. Quarteroni, and G. Vergara. Patient-specific generation of the purkinje network driven by clinical measurements of a normal propagation. 2014.

[102] I. E. Vignon-Clementel, C. A. Figueroa, K. E. Jansen, and C. A. Taylor. Outflow boundary conditions for 3d simulations of non-periodic blood flow and pressure fields in deformable arteries. *Computer methods in biomechanics and biomedical engineering*, page 625–640, 2010.

[103] H. Watanabe, S. Sugiura, H. Kafuku, and T. Hisada. Multiphysics simulation of left ventricular filling dynamics using fluid-structure interaction finite element method. *Biophysical Journal*, pages 2074–2085, 2004.

[104] D. Wiggert and A. Tijsseling. Fluid transients and fluid-structure interaction in flexible liquid-filled piping. *ASME. Appl. Mech. Rev.*, pages 455–481, 2001.

[105] Y. Zhang. Geometric modeling and mesh generation from scanned images. *Boca Raton: CRC Press*, 2018.